DTU Library

Microwave Instrument for Human Vital Signs Detection and Monitoring

Jensen, Brian Sveistrup

Publication date:
2013

Document Version
Publisher's PDF, also known as Version of record

Technical University of Denmark

Brian Sveistrup Jensen

Microwave Instrument for Human Vital Signs Detection and Monitoring

PhD thesis, July 2012

DTU Electrical Engineering
Department of Electrical Engineering

The work presented in this thesis was carried out at the Department of Electrical Engineering in partial fulfillment of the requirements for the PhD degree at the Technical University of Denmark.

Supervisor:

Tom Keinicke Johansen, Associate Professor, PhD,
Department of Electrical Engineering,
Technical University of Denmark

www.elektro.dtu.dk

Preface

This PhD study was carried out from June 1^{st}, 2009 to July 31^{st}, 2012 at the Department of Electrical Engineering, Technical University of Denmark, Kgs. Lyngby, Denmark. The effective study period has been 38 months, including 2 months extension. Financial support for the PhD Study was provided by the Technical University of Denmark. Associate Professor Tom Keinicke Johansen acted as project supervisor.

Production costs for IC development and fabrication has been partly financed by the Danish fund, *H. C. Ørsteds Fonden* and the German company and research institute *Innovations for High Performance Microelectronics GmbH*; abbreviated IHP GmbH.

For a period of 9 months, the PhD study was carried out in collaboration with DTU Post.Doc. Thomas Jensen who was working on the project *Kompakt trådløst overvågningssystem til måling af vitale livsfunktioner*[1] financed by the Danish fund, *Grosserer Alfred Nielsen og Hustrus fond (Radio-Parts Fonden).*

In the early days of this work, the highly changing nature of VSD data and the challenges encountered with harmonics and IM products led to the initial conclusion that a broadband system was needed. As several other projects within the Electromagnetic Systems (EMS) group at DTU, also needed broadband sources, a coorporation with the German IC manufacturing company and research institute, Innovations for High Performance Microelectronics GmbH (abbreviated IHP GmbH) was started. A total of 6 months was spent on the development of a fully integrated SiGe:C digital accumulator IC for use in a high speed direct digital synthesizer (DDS) at 20-24 GHz clock frequency. The goal was to combine this accumulator with an already developed 6-bit DAC from IHP, [1], thereby enabling generation of frequencies from 0-10 GHz, see the attached paper [JP1]. Although a wideband solution was eventually abandoned for the benefit of a more simple CW radar solution, the work gave an opportunity to become familiar with the 0.25 μm SiGe:C BiCMOS technology from IHP GmbH. A technology that was later used for implementing a radar front-end IC designed specifically for use in vital signs monitoring instruments. This IC is presented in the end of this thesis. At the moment of writing, the work on combining the 24 GHz accumulator IC with a 6-bit DAC from IHP GmbH is still ongoing at the Goethe University of Frankfurt, Germany, under supervision of Prof. Viktor Krozer.

[1] English translation: Compact wireless monitoring system for measurement of vital signs.

Acknowledgements

Without the help received from several people and the financial support received from H. C. Ørsted Fond for IC production, the completion of this PhD thesis would have never been possible.

First of all, I would like to thank Prof. Viktor Krozer for encouraging me to start the PhD study in the first place. Secondly, I would like to thank my supervisor Associate Prof. Tom Keinicke Johansen and my colleagues, PhD student Sævar Þór Jónasson and former Post.Doc Thomas Jensen for many interesting and fruitful discussions throughout the entire project period. Without the advice and inspiration from these three people, this thesis would not have been a reality.

Regarding the development of VISDAM, I would like to thank all the guys from the mechanical workshop at the Department of Electrical Engineering for their guidance and patience throughout the development and fabrication of the mechanical parts. Also, I would like to thank Technician Bo Brændstrup for sharing his knowledge on many practical issues related to the electrical assembly. Researcher Tonny Rubæk and Associate Professor Johan Jacob Mohr have been a great help in the development of LabView interfaces and the implementation of signal processing functions in Matlab, while Assistant Professor Vitaliy Zhurbenko has been a great help during measurements of the VSD IC.

I have to thank all of my friends and my whole family; especially my parents Lone and Arne, my brother Jesper and my great friend through many years, Anders. It is highly likely that they do not always fully understand my motives. However, they have always supported and encouraged me to carry on my activities and I have always felt, that they believed in me.

Last, but certainly not least, I would like to thank my lovely girlfriend Karen for urging me to do my best, even though it sometimes meant, that our time together would be limited. I look so much forward to October, where the two of us becomes three of us!

Technical University of Denmark
Kgs. Lyngby, Denmark
July, 2012

Brian Sveistrup Jensen

Abstract

This work investigates how to design microwave systems for vital signs detection (VSD) and monitoring (i.e. of respiration and heartbeat signals). Typical system types include ultra-wideband (UWB) and continuous wave (CW) radars. Due to its ease of implementation and potential for a low-power low-cost system, emphasis is on the CW type of VSD radars. The signal theory governing both homodyne and heterodyne CW VSD architectures is thoroughly examined. Throughout the discussion it is shown, how heterodyne systems using a low intermediate frequency (IF) can overcome some of the commonly encountered problems with homodyne systems, i.e. channel mismatches and DC offsets resulting from hardware imperfections.

To verify the theory, a new VSD radar system called the DTU-VISDAM (VItal Signs Detection And Monitoring) has been designed and build. The system together with the implemented signal processing methods is presented and real measurements verifies its operation. At the moment of writing, VISDAM consists of two heterodyne radar units operating at X-band with an IF frequency at 1 kHz. A small scale test is performed with VISDAM showing its capabilities to track the heart rate of a person in various different scenarios, i.e. lying on a bed and sitting straight up. Multi-unit measurements are carried out to remove random body movements not associated with the vital signs from the subjects being monitored.

In the pursuit of an even more compact solution, the work on a fully integrated SiGe:C VSD radar front-end was initiated. With financial support from the Danish fund *H. C. Ørsteds Fonden*, the IC was fabricated in the SG25H3 SiGe:C BiCMOS technology from Innovations for High Performance microelectronics (IHP) GmbH in Germany. The radar transceiver has been measured and although some adjustments could be of benefit, it is assessed that the radar chip can contribute to a full VSD system. Time did not allow for this latter system implementation of the IC.

Resumé

Dette arbejde undersøger hvorledes mikrobølgesystemer til brug for detektion og overvågning af menneskers vitale livstegn (åndedræt og hjerterytme) bør designes. På engelsk benyttes udtrykket "Vital Signs Detection" som forkortes til VSD. Typiske VSD systemer inkludere ultra-bredbåndede (UWB) og kontinuert transmiterende (CW) radarer. På grund af den relativt lette implementering og potentialet for et lav-effekts, billigt system er vægten i dette arbejde lagt på CW typen af VSD radarer. Signalteorien der gælder for både homodyne og heterodyne CW VSD arkitekturer bliver grundigt beskrevet. Gennem diskussionen bliver det vist hvordan heterodyne systemer der benytter en lav mellemfrekvens (IF), kan overvinde nogle af de almindeligt forekomne problemer der ses i homodyne systemer; heriblandt ubalance i modtagerkanalerne og DC offsets der resulterer fra ufuldkommenheder i hardwaren.

For at verificere teorien, er det nye VSD radar system, kaldet DTU-VISDAM (VItal Signs Detection And Monitoring), blevet designet og bygget. Systemet bliver presenteret sammen med den implementerede signal processering der benyttes til de rå VISDAM data og reelle målinger viser VISDAMs funktionalitet. Det nuværende system består af to heterodyne radar enheder der opererer ved X-bånd og med en IF frekvens på 1 kHz. En mindre gennemtestning af VISDAM viser dets evne til at tracke hjerterytmen på et menneske i forskellige situationer, herunder mens personen ligger i en seng eller mens denne sidder ret op. Målinger med begge enheder på samme tid bliver brugt til at fjerne tilfældige bevægelser af kroppen der ikke har med de vitale signaler at gøre.

I jagten på et endnu mindre system, blev der påbegyndt et design af en komplet integreret SiGe:C VSD radar front-end. Med finansiel støtte fra *H. C. Ørsteds Fonden*, blev IC'en fremstillet i SG25H3 SiGe:C BiCMOS teknologien fra det tyske firma Innovations for High Performance microelectronics (IHP) GmbH. Radar tranceiveren er blevet testet og selvom fintuning ville være gavnligt, vurderes det at radar chippen ville kunne bruges i et fuldt VSD system. Dog har der ikke været tid til en sådan implementering.

Acronyms and Abbreviations

ADC	Analog to Digital Converter
ADS	Advanced Design System (Simulation tool from Agilent Technologies)
BB	Baseband
BPF	Band Pass Filter
CMOS	Complementary Metal Oxide Semiconductor (Transistor technology)
CW	Continous Wave
DAC	Digital to Analog Converter
DC	Direct Current (zero frequency)
DSB	Double Sideband
DTU	Danish: Danmarks Tekniske Universitet (The Technical University of Denmark)
EEPROM	Electrically Erasable Programmable Read-Only Memory
EMS	Electromagnetic Systems Group (within Department of Electrical Engineering at DTU)
FDA	U.S. Food and Drug Administration
FFT	Fast Fourier Transform
HBT	Heterojunction Bipolar Transistor
HPB	High Pass Filter
IF	Intermidiate Frequency
IRM	Image Reject Mixer
K_a-band	Frequency band from 26.5 to 40.0 GHz
K-band	Frequency band from 18.0 to 26.5 GHz
LED	Light Emitting Diode
LNA	Low Noise Amplifier
LO	Local Oscillator
LPF	Low Pass Filter
MCU	Microcontroller Unit
MIMO	Multiple-Input-Multiple-Output
MPA	Medium Power Amplifier
NI	National Instruments (Corp.)
PCB	Printed Circuit Board
PCIe	Peripheral Component Interconnect Express (PC communication bus)
PLL	Phase Locked Loop
RF	Radio Frequency
SiGe:C	Silicon Germanium Technology (Carbon Doped Base)
SIL	Single antenna Injection Locked (radar)
SPI	System Packet Interface (serial interface)
SMA	SubMiniature version A connector
SRF	Self Resonance Frequency

Acronyms and Abbreviations - Continued

SSB	Single Sideband
UWB	Ultra Wide-Band
VCO	Voltage-Controlled Oscillator
VI	Virtual Instrument (NI LabView Interface)
VISDAM	Vital Signs Detection and Monitoring (the radar developed through the PhD project)
VNA	Vector Network Analyser
VSD	Vital Signs Detection
X-band	Frequency band from 8.0 to 12.0 GHz
XTAL	Crystal Oscillator

Publications

Below is listed the papers that have resulted from the PhD study period. These are attached at the back of this thesis. The only exception is [CP3], which is not attached due to an ongoing patent application process.

[JP1] B.S. Jensen, M.M. Khafaji, T.K.Johansen, V. Krozer and J.C. Scheytt, "Twelve-bit 20-GHz reduced size pipeline accumulator in 0.25 μm SiGe:C technology for direct digital synthesiser applications," *IET Circuits, Devices & Systems*, vol. 6, pp. 19-27, January 2012.

[CP1] Brian Sveistrup Jensen, Sævar Þór Jónasson, Thomas Jensen and Tom Keinicke Johansen, "Vital Signs Detection Radar using Low Intermediate-Frequency Architecture and Single-Sideband Transmission," *Accepted for publication at the European Microwave Conference*, Amsterdam RAI, The Netherlands, 2012.

[CP2] Brian Sveistrup Jensen, Thomas Jensen, Vitaliy Zhurbenko and Tom Keinicke Johansen, "Noise Considerations for Vital Signs CW Radar Sensors," *Convened Paper, European Conference on Antennas and Propagation*, pp. 2805-2809, Rome, Italy, 2011.

[CP3] Sævar Þór Jónasson, Brian Sveistrup Jensen and Tom Keinicke Johansen, "Study of Split-Ring Resonators for use on a Pharmaceutical Drug Capsule for Microwave Activated Drug Release," *Accepted for publication at the European Microwave Conference*, Amsterdam RAI, The Netherlands, 2012.

Contents

Chapter 1

Introduction

Measuring human vital signs (heartbeat and respiration) unobtrusively has been of great interest since the first wireless sensors were demonstrated in the early 1970's, [2]. The most commonly used non-contact sensor types are in the form of continuous-wave (CW) radars, [3–6], and ultra-wide band (UWB) radars, [7, 8]. However, other technologies, such as the so-called single-antenna injection locked (SIL) radars, [9], have been demonstrated as usable for vital signs detection (VSD). Although such systems have been conceived and utilized in many applications for several decades, the lack of sufficiently compact radar circuits and inadequate sensitivity has meant that research within this area was limited before the beginning of the new millenium. At that point in time, especially the group(s) of Prof. Victor Lubecke (University of Hawaii) and Prof. Jenshan Lin (University of Florida) began their comprehensive research *campaign*, which is still ongoing. It would not be meaningful to present the list of references to their work here. Instead, many references will be given throughout the thesis.

Currently VSD radar technology has reached a certain maturity where commercialization attempts have been started. An example of this is the Hawaiian company Kai Medical Inc. which have recently had their first product, *Kai Spot*, approved by the U.S. Food and Drug Administration (FDA). This device measures respiratory activity wirelessly. Although commercialization has been started, there is still room for further maturing of VSD technology; especially when it comes to accurately determining the heart rate as well.

VSD technology is not only of interest in medical applications, but can also be used for monitoring of infants and the elderly, both at hospitals and in their own homes. Furthermore, they are well suited for certain search and rescue operations as well as for military applications where living subjects are to be detected inside buildings etc. The biggest advantages of such instruments are that, they eliminate the need for wired sensors that often induce discomfort for patients and reduce the work load experienced by nursing staff, as hygiene demands will become less stringent and because no probe pads need to be placed, thus lowering the requirement for special education and training. For these types of sensors to be a viable alternative, they of course have to exhibit a performance that can compete with the traditional worn sensors.

The basic operation of any VSD radar is to isolate and detect the heartbeat and respiration motions coming from the person under test. When developing theory, it is common only to talk about the chest wall movement due to these motions. However, the entire body will often vary as function of the vital signs. This is especially true for the heartbeat motion. In fact, the sensitivity to the heartbeat signal increases when the respiration motion becomes less. This will be clear from the theory presented in Chapter 2 and was also discovered in [10, 11] where additionally the highest sensitivity to the heartbeat signal was found when measuring from behind the person.

The UWB version of a VSD radar is based on the comparison of echoes from a pulsed transmitter using very short duration pulses (i.e. wide bandwidth) such that range resolution is enhanced, at the cost of total transmitted power and thus maximum range. UWB radars compare successive echoes between which, the only difference is at the time point related to the moving target. By having sufficient range resolution, the small movements resulting from heartbeat and respiration activities can be detected. UWB radars have the drawback of being rather complex, as wideband circuits and a pulsed transmitter is needed. This often also increases the cost of such systems.

CW type VSD radars, transmit and receive continuously. For a target of zero net velocity, the phase of the received signal will be modulated according to the heartbeat and respiration activities. Comparing the phases between the transmitted and received signals, the desired vital signs signals can be extracted. The main drawbacks of the CW type VSD instrument, is a potentially high power consumption due to the continuous transmission, and the fact that a simple single-frequency CW radar cannot measure distance. Although distance is often not needed, the CW radar can measure this by modulating the frequency or the phase of the transmitted signal. However, this will increase the complexity of the system considerably. The advantages of CW VSD radars are that they can be made narrowband (often single-frequency) and that they are relatively easy to implement, while circuit components are easily available and often rather inexpensive. For these latter reasons, the CW VSD type was selected for this PhD study and as such, this type of radar will be in focus from this point on.

As low power consumption is attractive and because dynamic range is often not a problem, CW VSD radar instruments are often designed to transmit at low power levels (below 0 dBm). To some extent, this characteristic also reduces peoples concerns regarding long-term health issues, as low transmitted power and high frequencies (often above 2.4 GHz) prevents the microwaves from penetrading through skin, muscles and bones of the person in front of the radar. One exception is penetrading VSD instruments designed for disaster site or military applications where people are located beneath debris or avalanches or behind walls in buildings, respectively, [12–14].

Despite several successful demonstrations of compact, low-cost VSD radars in recent years, reported systems tend to show limited sensitivity towards the vital signs to be detected and monitored. In particular, the detection of heartbeat proves quite challenging in a real-life environment. Most CW type VSD radars presented so far, implement a homodyne I/Q architecture. This introduces problems with DC offsets and channel-to-channel imbalance; two factors that reduce sensitivity considerably, and thus requires some additional (and often rather advanced) calibration and signal processing steps. At the outset of the PhD project it was therefore decided to investigate possible enhancements to CW VSD radars, by improved transceiver architectures and hardware configurations. Based on theoretical investigations on various tranceiver architectures, the low-IF heterodyne architechture with single-sideband transmission proved particularly well suited for VSD radars. Therefore, an X-band VSD radar system, called DTU-VISDAM (VItal Signs Detection and Monitoring), was developed and tested with promising results. To further reduce size and cost in future VSD systems a 24 GHz SiGe:C BiCMOS radar chip was developed. Although measurements show minor deviations compared to simulations, it has been assessed that the IC is capable of implementation in a complete VSD system. However, time did not allow for such an implementation.

The use of heterodyne systems have traditionally been limited in VSD applications, due to phase noise problems at the small offset frequencies (below 4 Hz) introduced by the heartbeat and respiration activity. However, as shown in this thesis, careful design, especially with respect to coherency in the generator/aquisition circuitry, makes it possible to accurately detect the heart rate of a person. So far a very limited number of articles have been published on VSD radars using heterodyne transceivers. Some of the most relevant include [15–17].

Throughout theory and real life measurements, this thesis will concentrate on a single-subject environment. However, the reader can consult for instance [18] for inspiration on how to detect multiple subjects with CW VSD radars. The focus is on low-power systems at both $X-$ and $K-$band. Penetrading VSD radars are not considered.

Thesis Overview

The main part of this thesis consist of seven chapters including this introduction. Chapter 2 presents an architectual overview of the CW type (homodyne and heterodyne) radar transceivers used in VSD applications and further explains the benefits of using a heterodyne system. This overview will be supported by the signal theory describing each system.

Chapter 3 presents the double-unit DTU-VISDAM radar setup, which has been developed by the author as part of the PhD study, to verify that a heterodyne system is applicable in a VSD application. Chapters 4 and 5 presents the implemented VISDAM signal processing steps and a small-scale verification test, conducted on several test subjects.

Chapter 6 presents the VSD SiGe:C integrated circuit (IC) that has been designed by the author to replace large parts of the VISDAM units; mainly to reduce system size and eventually power consumption. Finally, Chapter 7 gives a conclusion and discusses some future aspects related to the further development of VISDAM.

A DVD containing additional appendixes has been appended to the thesis. This DVD includes the Matlab Function Set for the VISDAM radar signal processing as well as additional Matlab scripts used for generation of the figures presented throughout Chapter 2. Furthermore, a digital copy of the thesis is also included. The folder structure (content) of the DVD is listed in Appendix 9.

Chapter 2

CW VSD Radars: Signal Theory & Architectual Overview

As was mentioned in the introduction, this work concentrates on continuous wave (CW) VSD radar architectures. This chapter introduces the basic types of CW VSD radars and presents the signal theory governing their operation.

2.1 Signals of Interest: Human Vital Signs

The vital signs that are to be detected and monitored by the VSD instrument are the respiration and heartbeat activities. With respiration rates in the range of approximately 6 to 60 breaths per minute (bpm) and heart rates in the range of 40 to 200 beats per minute (also denoted bpm) these signals are in general considered to be very low-frequency signals (full range is 0.1 - 3.3 Hz). As will be explained further below, this becomes a major challenge when DC offsets are to be removed in the receiver path. Standard DC blocks in the form of capacitors will not suffice, as they will simply remove or severely attenuate the vital signs signals as well.

As was described above, VSD instruments are designed to measure only the variation on the surface of the chest wall. This implies that the amplitudes of the signals depend heavily on the physiological structure of the subject being monitored. For instance a large difference between men and women is to be expected and the same goes for persons of different weight. However, for the analysis carried out in this chapter, it is assumed that the chest wall movement due to respiration activity is in the range of 1 - 10 mm while that due to heartbeat activity is in the

	bpm	Frequency [Hz]	Chest wall displacement amplitude [mm]
Respiration	6-60	0.10 - 1.00	1 - 10
heartbeat	40-200	0.67 - 3.33	0.01 - 0.20

Table 2.1: Vital signs signals that are considered in the signal theory presented in this chapter.

range of 0.01 - 0.20 mm. Table 2.1 summarizes the characteristics of the vital signs signals considered in this chapter.

2.2 The Direct Conversion Architecture (Homodyning)

The signal theory behind VSD instruments is best explained by first considering the simple case of an instrument based on the direct conversion (homodyne) radar architecture, see Fig. 2.1. Two distinct cases are shown; the single channel and the quadrature (I/Q) receiver versions. They differ only by the down-conversion mixer and baseband circuitry and it will soon become clear why the I/Q version is much prefered over the single channel version.

The transmitted signal is generated by the system local oscillator (LO) and can be represented as follows

$$T(t) = LO_{RF}(t) = \cos\left(\omega_{RF}t + \theta_{RF} + \phi_{nRF}(t)\right) \tag{2.1}$$

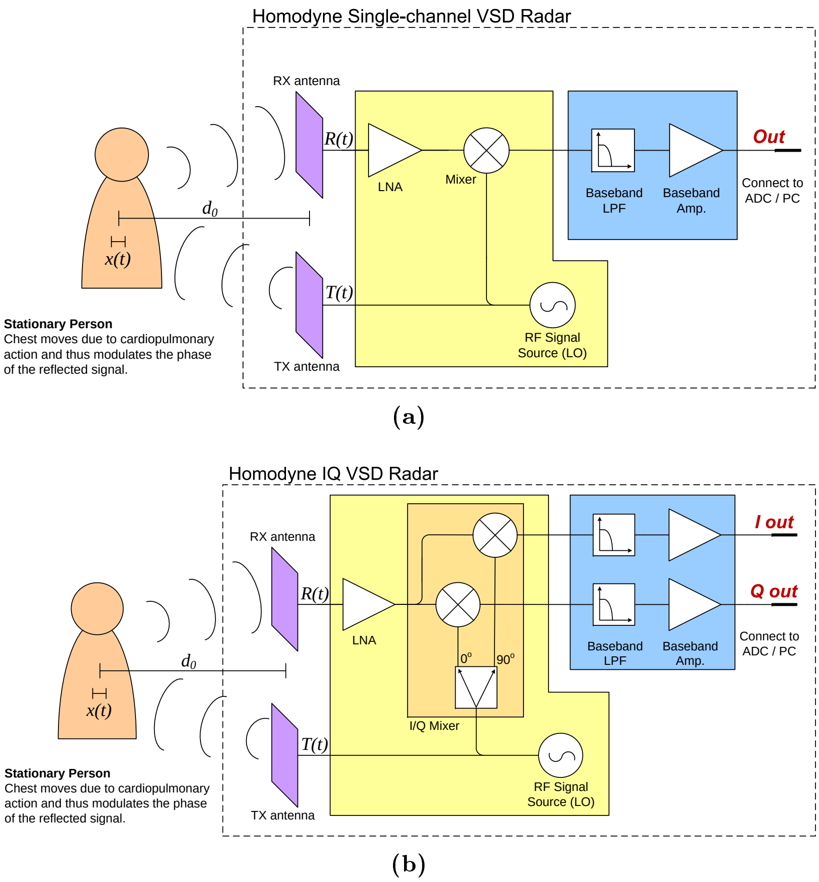

Figure 2.1: Simple block diagrams of two implementations of a VSD instrument based on the direct conversion (homodyne) radar architecture. (a) the single channel version and (b) the quadrature (I/Q) version. The nominal distance to the subject, d_0, and the time-varying chest wall displacement, $x(t)$ is indicated.

where $\omega_{RF} = 2\pi f_{RF}$ is the RF carrier frequency, θ_{RF} is an arbitrary phase offset and where ϕ_{nRF} represents the phase noise generated by the LO. The time-varying distance, $d(t)$, that the transmitted signal has to undergo before reaching the radar receiver is given by

$$d(t) = 2 \cdot \big(d_0 + x(t)\big) \tag{2.2}$$

where d_0 is the nominal distance to the target and where

$$x(t) = x_h(t) + x_r(t) \tag{2.3}$$

represents the chest wall movement due to heart- and respiration activity, respectively. Neglecting any path loss, the received signal is now given by

$$R(t) = \cos\left[\omega_{RF} t + 2\pi \frac{d(t)}{\lambda_{RF}} + \phi_{nRF}\left(\Delta t\right) + \theta_{RF} + \theta_0\right] \tag{2.4}$$

where $\lambda_{RF} = c/f_{RF}$ is the wavelength of the transmitted signal with c being the speed of light in free space, and where θ_0 represent any constant phase change caused by the electronic components and by the reflection off of the chest wall. Furthermore, the phase noise component, $\phi_{nRF}(t)$, is now shifted in time according to

$$\Delta t = t - \frac{d(t)}{c} \approx t - \frac{2d_0}{c} \tag{2.5}$$

where it is assumed that $x(t) << d_0$ so that the approximation $d(t) \approx 2d_0$ can be used.

Using the transmitter LO from (2.1) as LO source for the down-conversion mixer, we obtain the following baseband signal

$$B(t) \;=\; R(t) \cdot LO_{RF}(t) \;\overset{\text{LPF}}{\approx}\; \frac{1}{2}\cos\left(2\pi \frac{d(t)}{\lambda_{RF}} + \Delta\phi_{nRF}(t) + \theta_0\right) \tag{2.6}$$

where the last approximation sign indicates low pass filtering (LPF) to retrive only the baseband frequencies and where

$$\Delta\phi_{nRF}(t) = \phi_{nRF}\left(\Delta t\right) - \phi_{nRF}(t) \tag{2.7}$$

is the residual phase noise. When modulated onto the carrier, the low frequency of the vital signs would normally place the signals deep within any phase noise curtain of a given LO source. However, when using the same source for both transmission and reception the phase noise terms are correlated as shown in (2.7), thus effectively attenuating the residual phase noise. In the extreme case when $d_0 = 0$ and thus zero time delay, the phase noise will be completely attenuated, letting the receiver act as a perfectly matched filter. As d_0 increases, this filtering effect will degrade as the two terms of (2.7) will become more and more decorrelated. Due to the range (or flight time) dependency, this effect is often referred to as the *Range Correlation Effect* and was first described and mathematically formulated in [19]. Here the attenuation of the phase noise (filtering effect) was given as[1]

$$\Gamma(d_0, f_m) = \frac{1}{4}\sin\left(\frac{2\pi d_0 f_m}{c}\right)^{-2} \approx \frac{1}{4}\left(\frac{2\pi d_0 f_m}{c}\right)^{-2} \tag{2.8}$$

[1]Notice, that in [CP2] this formula was erroneously inverted to resemble instead a gain factor. The formula presented here for the phase noise attenuation is the correct one.

where f_m is the offset frequency from the carrier. The approximation is valid for small offset frequencies where the argument to the sine function becomes small.

VSD instruments operate primarily at close ranges and small offset frequencies. Based on (2.8), this means that residual phase noise from the LO is no longer the dominant noise term. Instead, flicker noise from mixers and amplifiers become dominant and the designer should consider using topologies suited for low flicker noise operation, i.e. use for example passive mixers with no or little DC bias. Recently, a setup was shown in [17] comparing the close-in noise floor in both a homodyne and a heterodyne (see Section 2.3) VSD setup. It was shown clearly that the lowering of flicker noise in the receive chain improved the overall noise performance considerably.

White noise (the noise floor) is normally a minor concern as signal levels are often high. The use of low noise amplifiers in the receive path are therefore not critical, although often included as a good design practice. A further discussion on noise issues in VSD instruments can be found in the appended conference paper [CP2].

2.2.1 Null-points and Optimum-points

In the microwave VSD litterature two terms that are often used are the so-called *null-points* and *optimum-points*. These are points in space (distance to target and back) where the VSD radar output is nearly zero or nearly linearly propertional to the chest wall movement, respectively. To investigate the null-point problem, (2.2) is inserted into (2.6) while the constant amplitude- and residual phase noise terms are neglected. The baseband signal can then be written as

$$B(t) = \cos\left(4\pi\frac{x(t)}{\lambda_{RF}} + \Delta\theta\right) \tag{2.9}$$

where

$$\Delta\theta = 4\pi\frac{d_0}{\lambda_{RF}} + \theta_0 \tag{2.10}$$

is the total phase shift due to electronic components, reflections and distance to the target. When considering chest wall movements due to heartbeat activity, a small phase modulation ($x(t) << \lambda_{RF}$) can often be assumed. In this case, the baseband signal can be approximated using the small-angle approximation as,

$$B(t)\Big|_{\Delta\theta=n\frac{\pi}{2}} \approx \frac{4\pi x(t)}{\lambda_{RF}} \quad , \; n = \text{odd integer} \;\rightarrow\; \textit{optimum-point} \tag{2.11a}$$

$$B(t)\Big|_{\Delta\theta=n\frac{\pi}{2}} \approx 1 - \frac{1}{2}\left(\frac{4\pi x(t)}{\lambda_{RF}}\right)^2 \quad , \; n = \text{even integer} \;\rightarrow\; \textit{null-point} \tag{2.11b}$$

in which it is seen that for $\Delta\theta = n\pi/2$ with n being an odd integer, the baseband signal is directly proportional to the chest wall movement, $x(t)$. However, for n being equal to an even integer, the variation of the baseband signal drops to its minimum and becomes highly non-linear as a function of chest wall movement. Hence the name; null-points. The null-point

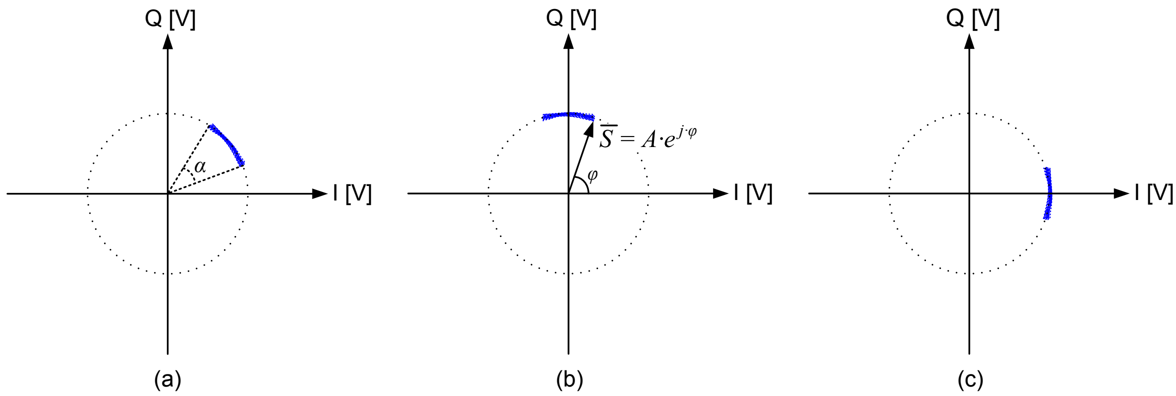

Figure 2.2: Illustration of a phasor representation of the baseband signal optained with a direct conversion VSD radar. The figure shows (a) a general case, (b) a case where the I-channel is in a optimum-point and Q-channel is in an null-point and (c) where I-channel is in null-point and Q-channel is in a optimum-point. $\overline{S}$ represents the phasor vector that trace out the measurement and the opening angle α indicates the modulation strength.

problem can be illustrated by considering a phasor representation of the baseband signal from (2.9), in the complex plane, see Fig. 2.2. As illustrated, when the modulation is small, only part of the full modulation circle would be represented in the baseband signal. For a single-channel receiver as the one illustrated in Fig. 2.1(a), either the in-phase (I) or quadrature (Q) channel would be available; not both. In the case of the I-channel being available, Fig. 2.2(b) represents a situation where the variation in output voltage is maximum and (2.11a) for the optimum-point location is valid. On the other hand Fig. 2.2(c) represents a situation where the variation in output voltage is at its minimum, and where (2.11b) for the null-point is valid.

As the phase distance between optimum-points and null-points is $\pi/2$, it is seen from (2.10) that this crossover occurs every $\lambda_{RF}/8$ of physical distance. Thus a small change in absolute distance to the target could potentially move the measurement from an optimum to a worst-case situation. To solve the null-point problem in the direct conversion architecture, a simple solution is to obtain both the I- and Q-channels, as was illustrated in Fig. 2.1(b) and successfully implemented in [5, 20]. This approach ensures that if one channel resides in a null-point, the other will be in an optimum-point. In mathematical terms, the LO signal from (2.1) is splitted to produce two quadrature signals given by

$$LO_{RF,I}(t) = \cos\Big(\omega_{RF} t + \theta_{RF}\Big) \tag{2.12a}$$

$$LO_{RF,Q}(t) = \cos\Big(\omega_{RF} t + \theta_{RF} - \frac{\pi}{2}\Big) \tag{2.12b}$$

which, when multiplied with the received signal from (2.4) and subsequently low pass filtered produces the following I/Q baseband outputs

$$B_I(t) = \cos\left(4\pi \frac{x(t)}{\lambda_{RF}} + \Delta\theta\right) \tag{2.13a}$$

$$B_Q(t) = \cos\left(4\pi \frac{x(t)}{\lambda_{RF}} + \Delta\theta - \frac{\pi}{2}\right) \tag{2.13b}$$

where again, the phase noise and the constant amplitude term of 1/2 resulting from sine multiplication has been neglected. For a target with zero net velocity, which is most often the case in VSD applications, the measurement points will not move around the full circle. The position of the measurements in the complex plane is solely determined by the constant phase term, $\Delta\theta$, from (2.10).

An alternative approach for dealing with null-detection points was recently presented in [21], where phase and frequency diversity was utilised by implementing multiple channels (at least two) each having their own receive antenna. Although this is an equally clever way of removing the null-detection problem, it inevitably also makes the antenna system and thus the entire radar more bulky.

The ratio between the opening angle, α, representing actual measurements and the full circle is equal to the ratio between the carrier wavelength and the chest wall displacement amplitude, i.e.

$$m_0 = \frac{\alpha}{360^\circ} = \frac{4\pi}{\lambda_{RF}} x(t)_{\mathrm{pp}}. \tag{2.14}$$

where $x(t)_{\mathrm{pp}}$ represents the peak-to-peak amplitude variation of $x(t)$. In an analogy to the world of RF communication circuits, the ratio of (2.14) will be refered to as the modulation index, m_0. In general, it can be stated that higher frequency VSD instruments will impose a higher modulation index, when the chest wall movement amplitude is unchanged. In other words; the intuitive characteristic that sensitivity increases when the carrier frequency increases, applies. The condition used for the approximations in (2.11a) and (2.11b) is the same as requiring a low modulation index.

An alternative approach for removing the null-point problem in a direct conversion receiver was introduced in [6, 22, 23] and is a special case of the single-channel version, in which a double-sideband (DSB) signal is transmitted. This technique does not eliminate null-points fully, but extends the range between null-points by exploiting the different wavelengths and thus phase shifts encountered by the two sideband signals. Furthermore, a frequency tuning option for placing the measurement in a near-optimum situation was included.

2.2.2 I/Q Baseband Signals: Amplitude Spectrum Characteristics

The baseband signals from (2.13a) and (2.13b) contain respiration- and heartbeat information through the term $x(t)$. To extract these signals and seperate them from each other, a number of signal processing steps are needed. At low modulation indexes, m_0, harmonics and intermodulation (IM) products in the raw baseband signals are low and thus the calculation of a simple amplitude spectrum might give adequate results. On the other hand; when the sensitivity increases due to an increased modulation index, higher harmonics and intermodulation products are observed. As will be shown in Section 2.2.3 a better way to process baseband signals is to extract the actual phase information and investigate the phase spectrum. Here, however, the characteristics of the amplitude spectrum is investigated.

The movement of the chest wall modulates the phase of the carrier in a linear manner according to (2.2). However, the phase to amplitude translation is non-linear through the sine function, and thus gives rise to mixing products between frequency components included in the time-varying phase term dominated by $x(t)$. Assuming sinusoidal chest wall movements, (2.3) can be rewritten as

$$x(t) = m_r \sin(\omega_r t) + m_h \sin(\omega_h t) \tag{2.15}$$

with m_r and m_h being the chest wall movement amplitudes of the respiration and heartbeat activities, respectively, while $\omega_r = 2\pi f_r$ and $\omega_h = 2\pi f_h$ represents the corresponding angular frequencies. In this case, it was shown in [10] that the baseband signal can be represented as a Fourier series as follows

$$B(t) = \sum_{k=-\infty}^{\infty} \sum_{l=-\infty}^{\infty} \left[J_l\left(\frac{4\pi m_r}{\lambda_{RF}}\right) J_k\left(\frac{4\pi m_h}{\lambda_{RF}}\right) \cdot \cos(k\omega_r t + l\omega_h t + \Delta\theta) \right] \tag{2.16a}$$

$$= \sum_{k=-\infty}^{\infty} \sum_{l=-\infty}^{\infty} \left[J_l\Big(\frac{m_{0r}}{2}\Big) J_k\Big(\frac{m_{0h}}{2}\Big) \cdot \cos\big(k\omega_r t + l\omega_h t + \Delta\theta\big) \right] \tag{2.16b}$$

where $J_n(x)$ is the Bessel function of first kind, order n with argument x and where m_{0r} and m_{0h} are the modulation indexes for respiration and heartbeat activities, respectively. It is seen that an infinite number of harmonics and intermodulation (IM) products with just as many different amplitudes exist. With reference to the phasor illustration of Fig. 2.2 it can be explained as follows. The heartbeat causes a very small chest wall movement in itself. Not enough to actually move the modulation point around the circle in the I/Q plane. However, the heartbeat modulation is done on top of the much larger respiration signal, which actually do move the modulation point as time goes by. The result is that amplitude variation caused by heartbeat alone depends heavily on the instantauneous value of the respiration signal. The result is a mixing action between the two signals which increase with an increasing modulation index.

As an example, the I/Q baseband signals from (2.13a) and (2.13b) have been simulated with Matlab for three different carrier frequencies, see Fig. 2.3. The Matlab script is included on the appended DVD, see DVD content in Appendix 9. Respiration- and heart rates as well as chest wall displacement amplitudes has been kept constant. The time-domain signals, amplitude spectrums (calculated using fast Fourier transform, FFT) and I/Q phasor plots are shown for each carrier frequency. Going from the 2.40 GHz case to the 10.0 GHz case it is easily seen from both the time- and frequency domain plots, that the sensitivity increases with increasing frequency. However it is also seen that the amplitude spectrum becomes cluttered with respiration harmonics and respiration/heartbeat IM-products. The 24.0 GHz case shows not only a further degradation in spectral purity, but also a small lowering of the signal strength related to the heartbeat signal. The reason for this is that the energy that would normally go into the fundamental respiration- and heartbeat signals is suddenly distributed into the harmonics and IM-products and at this point, the vital signs are completely buried within undesired spectral components. Automatic detection of the true respiration and heartbeat signals therefore becomes increasingly difficult as the carrier frequency increases. Even though human vital signs are not perfectly sinusoidal, it was shown in [10] that the Bessel function analysis approach correlated well with actual VSD measurements. An algorithm based on Bessel functions is, however, very vulnerable to noise components, as an accurate estimation of the fundamental respiration movement amplitude, m_r, is important to resolve the remaining spectral components. In [24] a better performance was obtained using the so-called RELAX algorithm for spectral estimation.

In the light of the properties described above, it was first sought in [25] to estimate the optimum carrier frequency for a VSD instrument, based on harmonic balance simulations carried out with Agilent ADS. The results compared well with the Bessel function analysis from (2.16a) and (2.16b). To obtain a good model for the direct conversion type of VSD radar in the beginning of this work, these simulations were redone using the human body model and ADS setup shown in Appendix 8. The simulation results are shown in Fig. 2.4 for different respiration amplitudes. Fig. 2.4(a) shows the strength of the actual heartbeat signal as a function of carrier frequency, while Fig. 2.4(b) shows the ratio between the heartbeat and the nearest (and most often the highest) interferer, the third harmonic of the respiration signal.

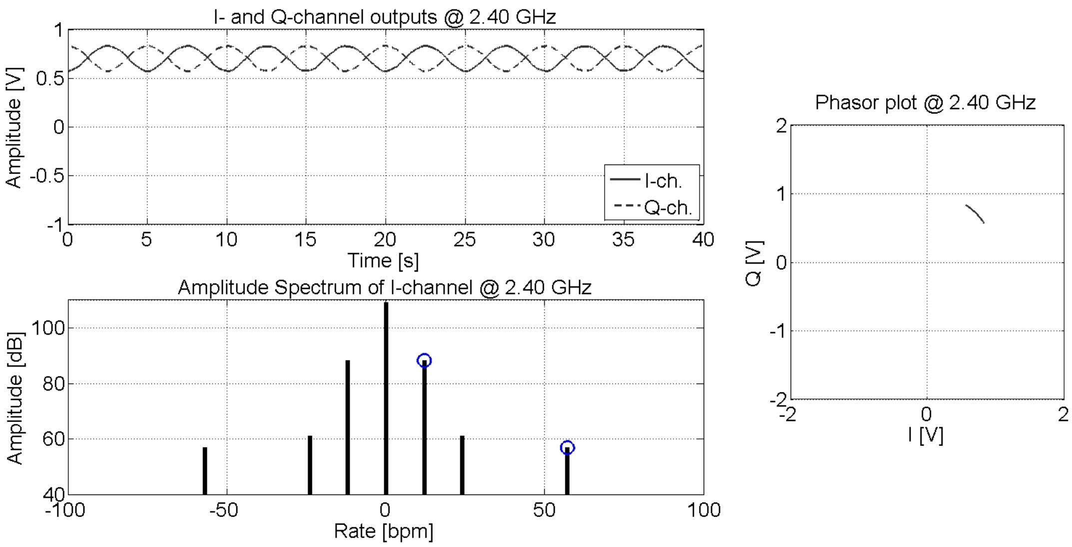

(a)

Figure 2.3: Matlab simulation of the I/Q baseband spectrum at different carrier frequencies: (a) 2.40 GHz, (b) 10.0 GHz and (c) 24.0 GHz. Chest wall displacement amplitudes are fixed at m_r=1.8 mm and m_h=0.05 mm while respiration- and heart rates are fixed at 12 bpm and 57 bpm, respectively (rings in amplitude spectrum). $\Delta\theta = \pi/4$ is used to split the output equally between I- and Q- channels. **Figure continuous on next page...**

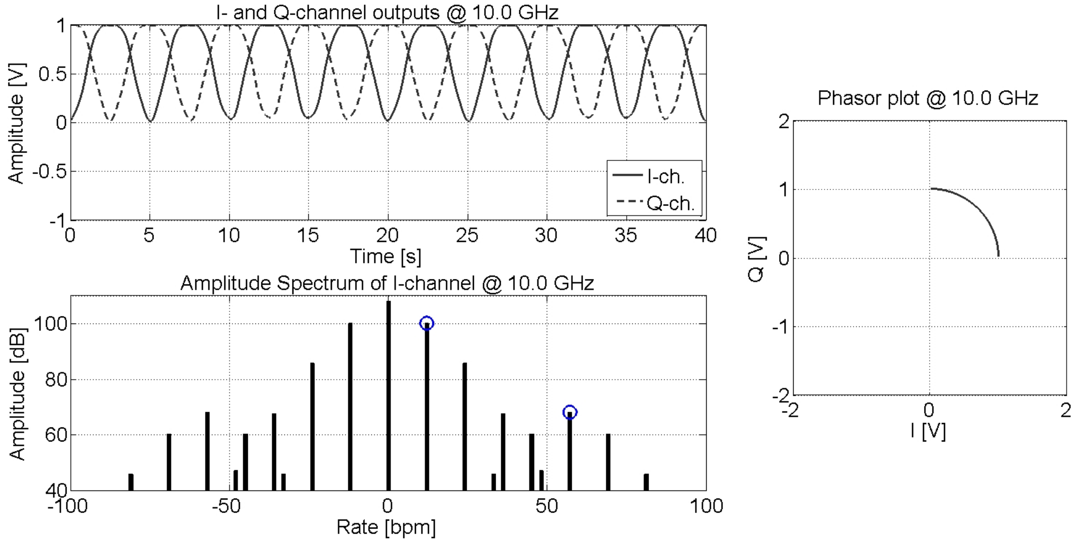

(b)

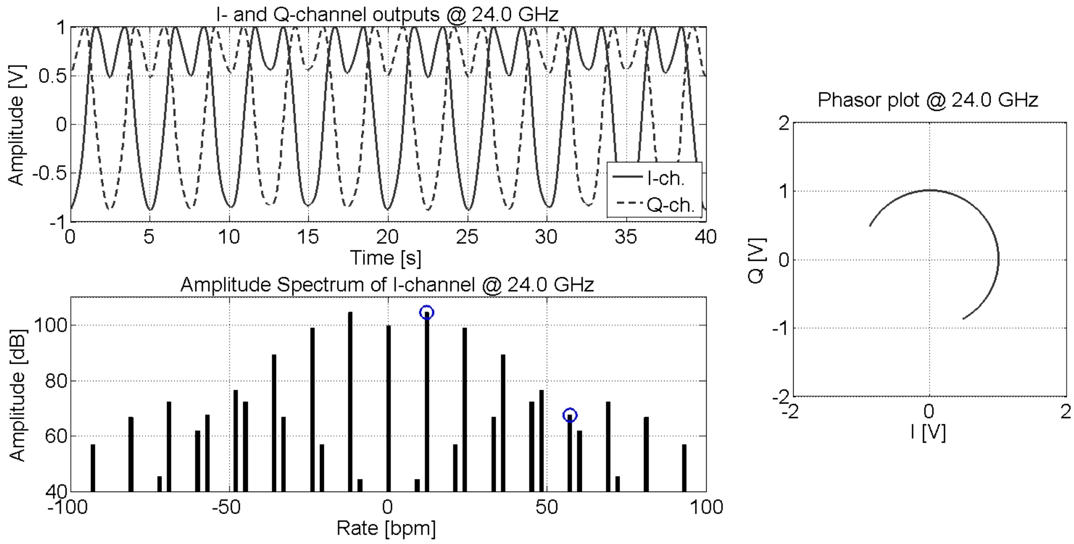

(c)

Figure 2.3: ... continued figure.

This latter case can be seen as a measure of how easy it is to detect the correct heartbeat component in the amplitude spectrum. The y = 1 line is a reference to when the interferer dominates over the actual heartbeat signal. For each of the simulation points, the constant phase change was set as to distribute the signals evenly between the I- and Q- channels; just as was done in the Matlab simulation from Fig. 2.3.

It is clearly seen that in the beginning the strength of the heartbeat signal increases with increasing carrier frequency. However, at some point dependent upon the respiration strength, a maximum sensitivity point is reached, after which it drops and actually continuous all the way to a zero-detection-point. At this point the energy of the fundamental heartbeat signal is completely distributed to the heartbeat harmonics and IM-products. For a respiration related chest wall displacement amplitude of only $m_r = 1.8$ mm the interferer begins to dominate already at 12 GHz. Respiration amplitudes can be much larger than 1.8 mm and thus this break-point frequency can become much lower. Furthermore, the situation changes when the respiration- and heart rates, f_r and f_h, changes. Especially, situations can occur where a spe-

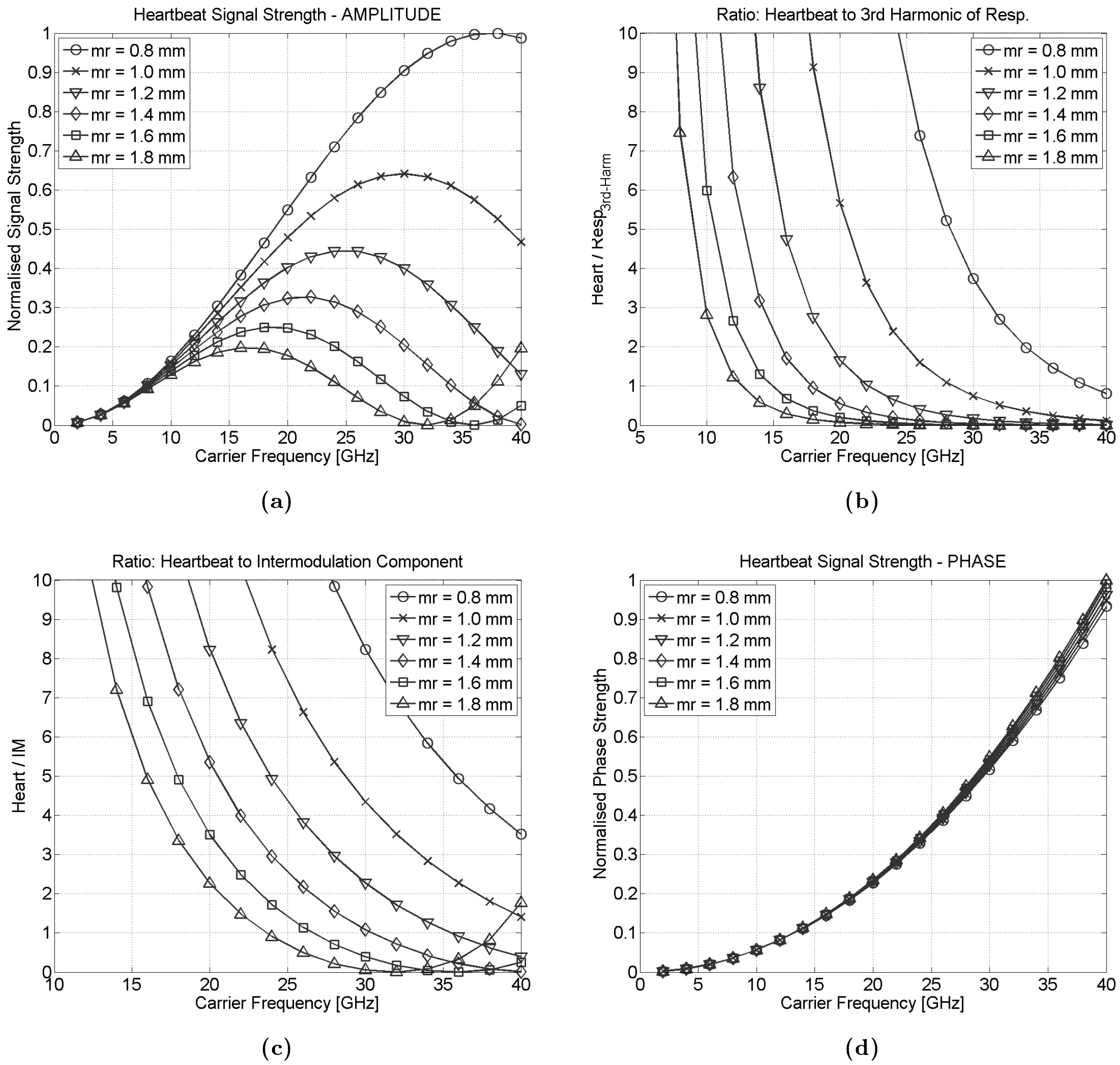

Figure 2.4: ADS simulation of direct conversion VSD instrument using amplitude spectrum for signal extraction. ADS Setup and human body model is shown in Appendix 8. (a) showing heartbeat signal strengh, (b) showing ratio between heartbeat and 3'rd harmonic of respiration signal, (c) showing ratio between heartbeat and the IM-product component and (d) showing phase signal strength. All plots are shown as function of carrier frequency. Heart rate was set to 72 bpm while respiration rate was set to 22 bpm.

cific harmonic of the respiration signal lies on top of the heartbeat signal and thus completely clutters the result.

Based on a person at rest (relatively low m_r) it was concluded in [25] that the carrier frequency could be increased up to the lower region of the K_a-band. Beyond that it simply becomes too difficult to sort out the different signal components based on spectral peaks alone. However, what will be shown next is that this is only true when the baseband *amplitude* spectrum alone is evaluated.

2.2.3 I/Q Baseband Signals: Phase Spectrum Characteristics

If the phase information is extracted from the baseband signal, the original signals which are linearly proportional to the chest wall displacement are obtained. Basically this means that the resulting phase signal includes only the two fundamental frequency components caused by the respiration- and heartbeat activity. Although additional challenges arise (described below), this technique was proven useful for implementation in VSD instruments in [26, 27]. The modulated phase, ϕ_m, can be extracted based on the I/Q baseband signals, (2.13a) and (2.13b), using simple arctanget demodulation as follows

$$\phi_m = \arctan\left[\frac{B_Q(t)}{B_I(t)}\right] = \arctan\left[\frac{\cos\left(4\pi\frac{x(t)}{\lambda_{RF}} + \Delta\theta - \frac{\pi}{2}\right)}{\cos\left(4\pi\frac{x(t)}{\lambda_{RF}} + \Delta\theta\right)}\right] = 4\pi\frac{x(t)}{\lambda_{RF}} + \Delta\theta\ . \qquad (2.17)$$

This signal is linearly proportional to the chest wall displacement, $x(t)$, and also includes the offset phase $\Delta\theta$. The latter does not contribute to the detection of the respiration- and heartbeat rates and can be seen as a DC phase component that is proportional to the distance to the subject according to (2.10).

Performing the arctangent demodulation on the simulated dataset from Fig. 2.3(c) for the 24 GHz carrier frequency, and then calculating the FFT of the phase signal to obtain what is here called the phase spectrum, the result shown in Fig. 2.5 is obtained. The spectrum is now clean from harmonics and IM-products just as anticipated and for an automatic detection algorithm an easier job is now ahead, using either simple spectral peak detection or a sliding window auto-correlation approach. Chapter 4 will deal in more details with the actual signal processing steps carried out.

2.2.4 Phase and DC Offset Errors in I/Q Arctangent Demodulation

The accuracy of the arctangent demodulation is limited primarily by two things; channel imbalance (phase and gain) and DC offsets. As a simple example of the latter error source, the 24 GHz simulation setup from Figures 2.3 and 2.5 is continued in Fig. 2.6; now with a DC offset added to each of the I/Q channels. It is easily seen that the phase signal is skewed and that this again results in a cluttered spectrum. The figure also illustrates the basic phase demodulation problem; that when the center of the modulation circle moves away from the (I,Q)=(0,0) point, the phase computed by (2.17) gets distorted. In the extreme case, when the modulation circle no longer encloses the (0,0)-point the phase can never be computed in

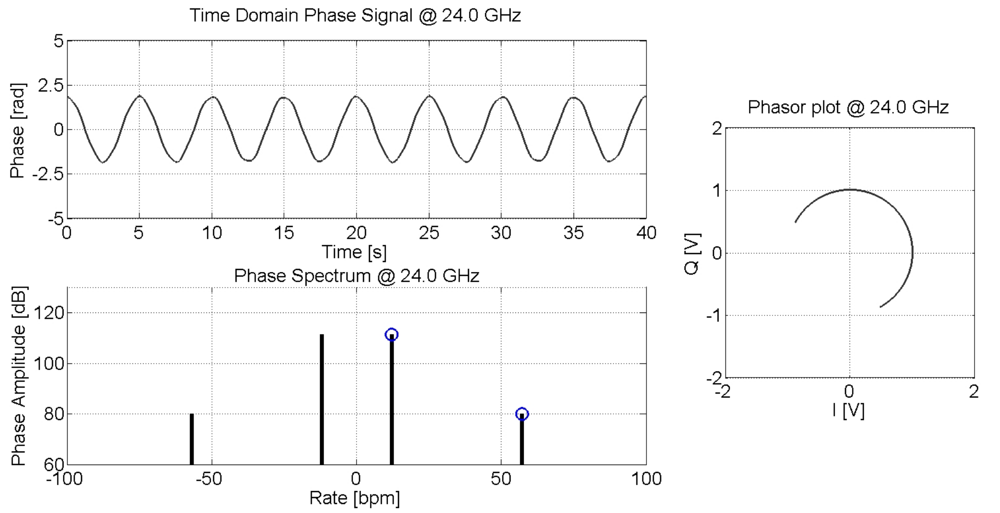

Figure 2.5: Phase demodulation (arctangent) simulation on the same 24 GHz data as was used in Fig. 2.3(c). (a) showing time-domain plot and (b) showing phase spectrum.

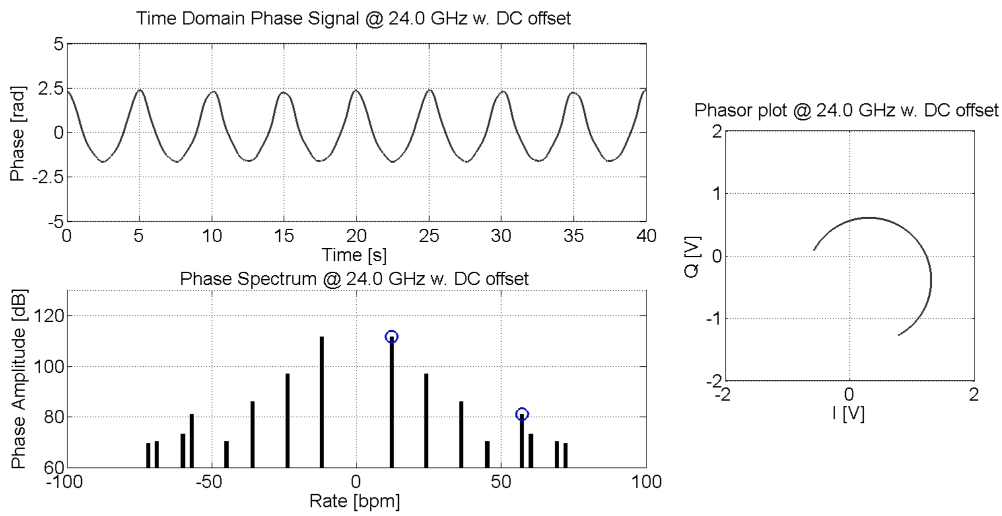

Figure 2.6: Matlab simulation of arctangent demodulation of the 24 GHz setup as was used in Figures 2.3 and 2.5; now with DC offset of $I_{DC} = 0.3$ V and $Q_{DC} = -0.4$ V.

the entire 360 degrees, although the signal from the subject vital signs might require this.

The typical sources of DC offset errors are depicted in Fig. 2.7, with clutter effects from stationary targets and antenna cross-coupling (or reflection in single-antenna systems) as the main sources. What are not shown are the internal error components such as LO-leakeage in the mixer resulting in self-mixing and internal channel cross-talk. These internal error sources can be included in the antenna cross-talk component depicted in the figure. Parsing these signals through the down-converter, gives rise to the following DC error components in the

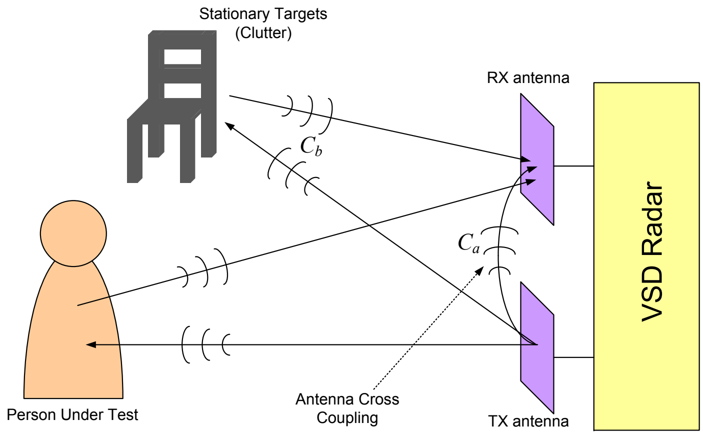

Figure 2.7: DC offsets can occur due to clutter effects from antenna cross-coupling and stationary targets in the beamwidth of the antennas; represented here by the coupling factors, C_a and C_b, respectively. C_a includes also internal transmit-to-receive isolation in the hardware.

baseband signals (amplitude constants from sine multiplication is again neglected)

$$\text{I-ch. DC errors from mixing (homodyning)} \begin{cases} E_{I,Ca}(t) & = C_a \cdot L_I(\theta_{Ca}) & \overset{\text{LPF}}{\approx} & C_a \cos\left(\theta_{Ca}\right) \\ E_{I,Cb}(t) & = C_b \cdot L_I(\theta_{Cb}) & \overset{\text{LPF}}{\approx} & C_b \cos\left(\theta_{Cb}\right) \\ E_{I,CLO}(t) & = C_{LO} \cdot L_I(\theta_{CLO}) & \overset{\text{LPF}}{\approx} & C_{LO} \cos\left(\theta_{CLO}\right) \end{cases} \tag{2.18a}$$

$$\text{Q-ch. DC errors from mixing (homodyning)} \begin{cases} E_{Q,Ca}(t) & = C_a \cdot L_Q(\theta_{Ca}) & \overset{\text{LPF}}{\approx} & -C_a \sin\left(\theta_{Ca}\right) \\ E_{Q,Cb}(t) & = C_b \cdot L_Q(\theta_{Cb}) & \overset{\text{LPF}}{\approx} & -C_b \sin\left(\theta_{Cb}\right) \\ E_{Q,CLO}(t) & = C_{LO} \cdot L_Q(\theta_{CLO}) & \overset{\text{LPF}}{\approx} & -C_{LO} \sin\left(\theta_{CLO}\right) \end{cases} \tag{2.18b}$$

where

$$L_I(\theta_x) = \cos\left(w_{RF}t + \theta_{RF} + \theta_x\right) \cdot LO_{RF,I}(t) \tag{2.19a}$$

$$L_Q(\theta_x) = \cos\left(w_{RF}t + \theta_{RF} + \theta_x\right) \cdot LO_{RF,Q}(t) \tag{2.19b}$$

and where C_a, C_b and C_{LO} are coupling factors for the antenna cross-coupling, stationary targets (clutters) and LO leakage, respectively. Also, θ_{Ca}, θ_{Cb} and θ_{CLO} are the associated phase shifts encountered through electronic components and flight time (distance) between the antennas and/or to the clutter and back. Both phase noise and any amplitude constants related to the mixing are neglected. Besides these mixing-related errors, there also exist a simple DC error associated with imperfections in each of the baseband channels. In the following, these errors will be called $E_{I,BB}$ and $E_{Q,BB}$, respectively.

Due to the near-DC frequencies of the vital signs, conventional DC-blocks cannot be employed in VSD direct-conversion instruments without also severely attenuating the desired signals. At first, it would appear easy to remove the DC offset in the digital processing by simply removing the mean value from the signals after sampling. However, the DC component of the baseband signal contain not only offset errors; In fact a desired DC component also exist, see Fig. 2.8(a). As the I/Q plot shows, the modulation circle is often not completely filled (m_0<1). This means, that even for a pure baseband signal, there exist a DC offset, related alone to the position of the subject in front of the radar, i.e. due to $\Delta\theta$ from (2.10). If DC offset errors are added, the situation of Fig. 2.8(b) is obtained. As shown in the small boxes, removal of the mere mean value results in an error, because not only is the unwanted error removed, but also the desired DC component. Some of the DC errors are often found through calibration routines, however, as was mentioned above, static clutter from the surroundings can affect DC error performance. This means that not all DC errors can be calibrated out dynamically (as the surroundings might change) before measuring. One signal processing technique for removal of DC errors in VSD data, was presented in [28]. Here the circumference of the modulation circle was estimated using the Levenberg-Marquardt algorithm, to find the center of the circle and thereby the DC offset errors. To this end; the estimation of the circumference becomes more precise when a greater part of the modulation circle is filled with measurement points (higher m_0), and for this reason it is of benefit to increase the carrier frequency. What is peculiar, is that a high m_0 was troublesome for the amplitude spectrum, whereas for the performance of arctangent demodulation it can in general be of benefit. Only in the extreme case where the chest wall displacement causes the signals to move multiple times around the modulation circle, a simple removal of the mean value might give adequate results as the samples would then not include a desired DC signal.

To evaluate the level of DC offsets that can be allowed for proper detection, the aforementioned Matlab simulation has been extended to include a DC offset analysis (for m-script code, see Appendix 9 and appended DVD). The procedure used in the simulation is shown in Fig. 2.9. Because DC offsets can easily become higher than the desired VSD signals, the offset is varied from 0% to 200% of the original signal, at different modulation angles to pick up the worst case scenario.

The angle of the DC offset vector, $\overline{V}_{\mathrm{DC}} = (V_{offset,I}, V_{offset,Q})$, applied to the samples,

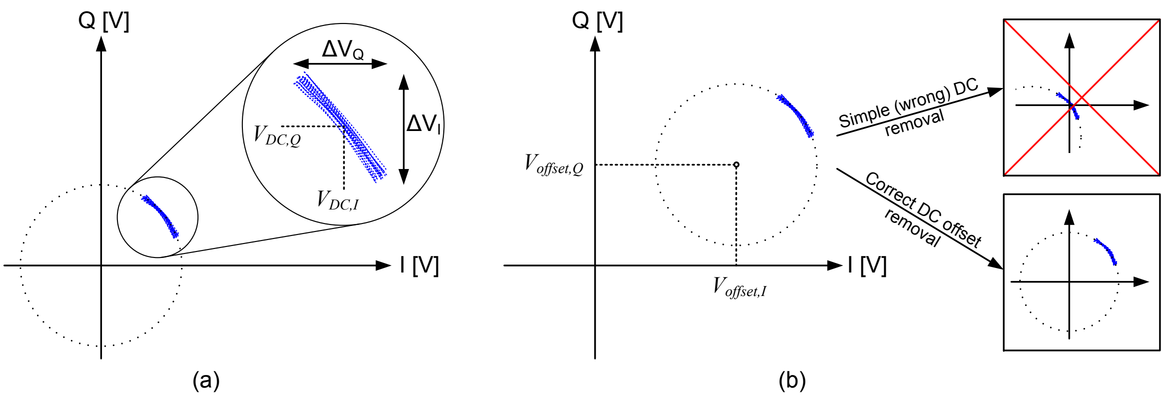

Figure 2.8: Illustration of the different types of DC offsets that exist in the baseband signals of an I/Q VSD radar. (a) shows a pure signal while (b) shows a signal with DC offset errors as well as incorrect and correct DC removal.

does not influence the result, as the modulation is done at different modulation angles. The simple case of having no offset in the Q-channel is therefore used. For each scenario the phase spectrum is calculated and the most likely interferers to the heartbeat signal are monitored; those being the IM-product as well as the third and fourth harmonic of the respiration signal. The ratio of the heartbeat signal to each of these potential interferers are shown in Fig. 2.10. To compare situations for different modulation indexes, the cases from above, i.e. 2.4 GHz, 10.0 GHz and 24.0 GHz carriers are shown.

The results indicate that when the modulation index increases, the DC offset that can be tolerated goes down. Especially, it is seen for the 10 GHz and the 24 GHz cases that at least one interferer becomes higher than the heartbeat signal (below 0 dB on y-axis) at an offset of approximately 70% and 40%, respectively. The 2.4 GHz case shows that the DC offset needs to be higher than 120% before an interferer begins to dominate the phase spectrum. Notice that for some plots, the $\Delta\theta = 0$ lines are not shown. This is because the heartbeat signal is more than 100 dB higher than any of the interferers.

A rather peculiar behaviour is seen at an offset of 100% for all frequencies. At this exact point, all the harmonics and IM-products disappear, resulting in a clean phase spectrum. This shows up as a peak for all ratios in the graphs of Fig. 2.10. The only exception to this is for a modulation index of $\Delta\theta = \pi$. The reason for this discrepancy is that this is the only modulation that moves across the $Q = 0$ line that seperates the upper and lower half planes and thus moves across the singularity of the arctangent function. The graphs from Fig. 2.10 can be used for estimating the residual DC offset that can be allowed after calibration and/or digital signal processing before the actual arctangent demodulation is carried out. As a general rule for systems operating up to 24 GHz, the DC offset should not be allowed to exceed approximately 50% of the actual vital signs signals, without actively compensating for the offset.

For the I/Q homodyne system, two baseband channels are needed. This potentially introduces both amplitude- and phase- imbalances, arising from different amplification and imperfect 90-degree split in the I/Q down-conversion mixer. Furthermore, phase errors can also arise from different phase shifts in the baseband circuitry of the two channels. However,

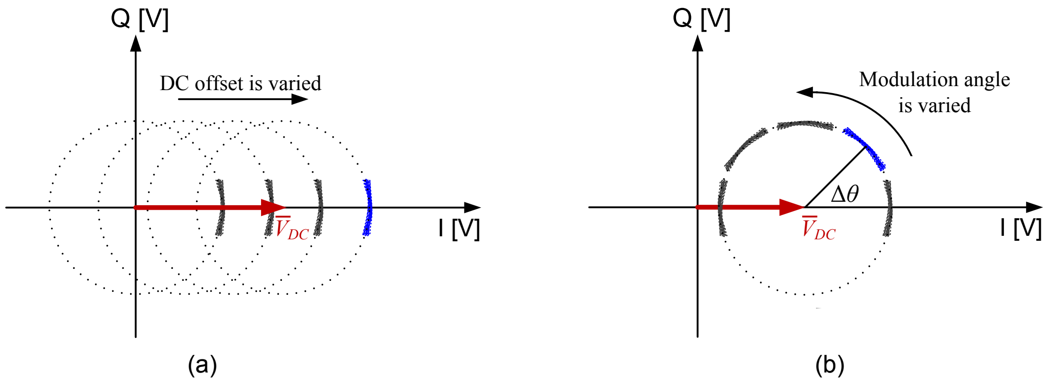

Figure 2.9: Procedure used for the DC offset analysis in arctangent demodulation of VSD data, with (a) showing the DC offset vector variation and (b) showing the variation of the modulation angle for each DC offset vector. Simulation performed using Matlab. For Matlab script, see Appendix 9 and appended DVD.

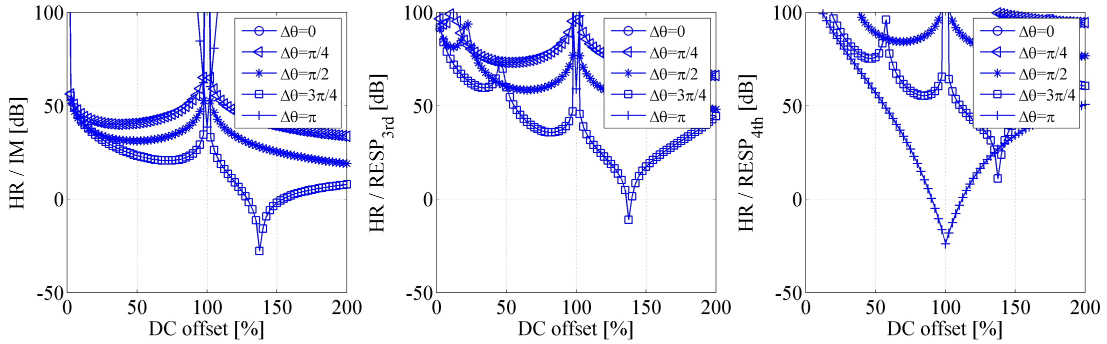

(a) Carrier Frequency: 2.4 GHz

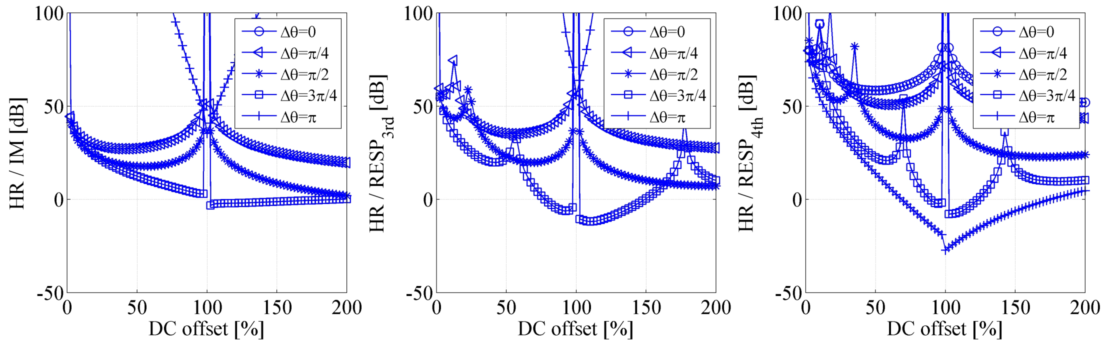

(b) Carrier Frequency: 10.0 GHz

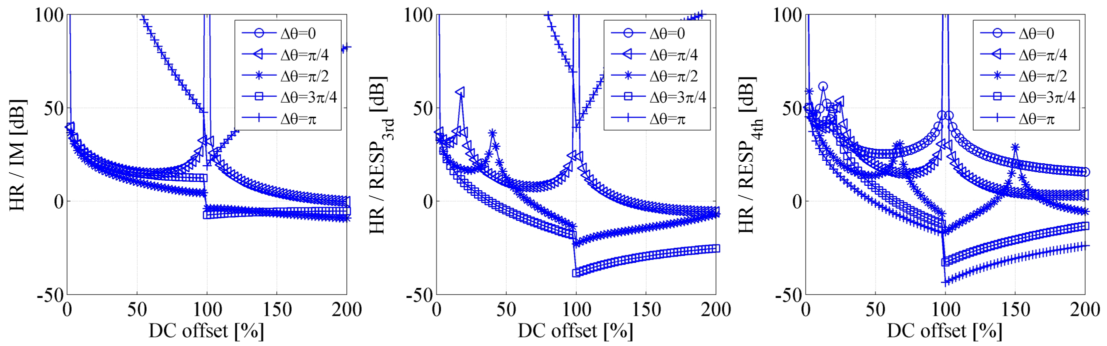

(c) Carrier Frequency: 24.0 GHz

Figure 2.10: DC offset analysis in arctangent demodulation of VSD data at (a) 2.4 GHz, (b) 10.0 GHz and (c) 24.0 GHz. The analysis is based on a heartrate of 57 bpm and a respiration rate of 12 bpm, with chest wall displacements of $m_h = 0.05$ mm and $m_r = 1.8$ mm for the heartbeat and respiration activities, respectively.

in homodyne VSD instruments this latter phase error can normally be neglected as phase imbalances are easily kept small at baseband frequencies, i.e. below 3.5 Hz.

Taking into consideration not only DC offsets, but also channel imbalances, the I/Q signals from (2.13a) and (2.13b) can be rewritten as

$$B_I(t) = \cos\left(4\pi\frac{x(t)}{\lambda_{RF}} + \Delta\theta\right) + E_{I,DC} \tag{2.20a}$$

$$B_Q(t) = A_e \cos\left(4\pi\frac{x(t)}{\lambda_{RF}} + \Delta\theta - \frac{\pi}{2} + \phi_e\right) + E_{Q,DC} \tag{2.20b}$$

where A_e and ϕ_e are the amplitude- and phase- imbalance errors, respectively, while $E_{I,DC}$ and $E_{Q,DC}$ represents the total DC offset errors given by

$$E_{I,DC} = E_{I,Ca} + E_{I,Cb} + E_{I,CLO} + E_{I,BB} \tag{2.21a}$$

$$E_{Q,DC} = E_{Q,Ca} + E_{Q,Cb} + E_{Q,CLO} + E_{Q,BB} \tag{2.21b}$$

The effects of these imbalances are the same as those found above, namely a reduced signal to clutter interferer ratio. The system architecture described next (and implemented as a prototype during the project period), does not implement a multi-channel system. Therefore, no further imbalance analysis is given here. Instead, the reader should consult [29] for a general description of the implications and methods for calibration in I/Q systems. In particular the reader should also see [30] which implements some of these methods for a VSD system.

2.3 Low-IF Coherent Heterodyne Architecture

Traditionally, most of the litterature on microwave VSD instruments have been focusing on homodyne architectures as the ones described above. However, recently there have been a technology move towards using heterodyne architectures instead. Although the hardware required for realising such systems is slightly more complex, this configuration has the potential to remove problems related to channel mismatches and some of the DC offset errors. It is also the choice of architecture for the prototype VSD radar developed through this project, see Chapter 3.

A heterodyne system converts the received RF signal to an intermediate frequency (IF) signal, which is then directly sampled before digital processing. The benefit is that the down-conversion process do not fold the RF signal around DC, and thus do not mix frequencies located above and below the RF carrier. The result is that only one receiver channel is needed, thus removing the problem of channel mismathes. Moreover, any DC errors related to imperfections in the receiver electronics, can be eliminated by using bandpass filters (BPF) or a simple DC block. However, as will be shown, stationary clutter still causes DC-like error-components in the final digital phase signal.

2.3.1 Generating the Intermediate-Frequency Signal

Three different simplified heterodyne architectures are shown in Fig. 2.11. The architectures of Figures 2.11(a) and (b) both use a sidestep configuration with a mixer and an IF generator.

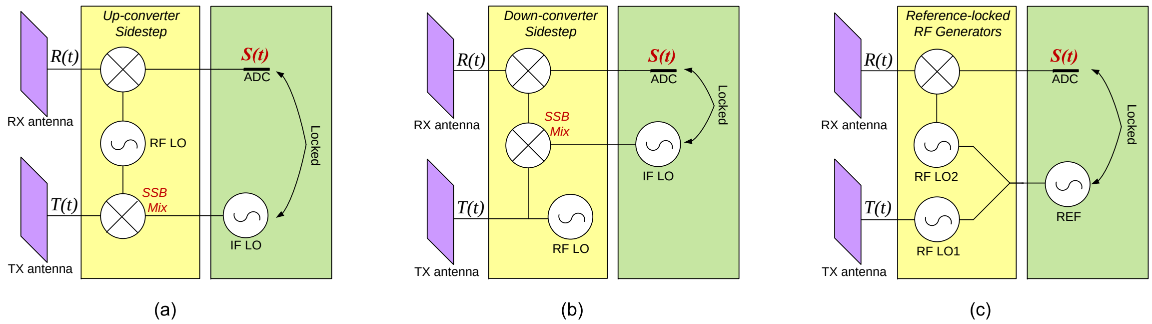

Figure 2.11: Three different ways to generate the IF offset in a heterodyne VSD radar. Methods are (a) "Up-converter Sidestep", (b) "Down-converter Sidestep" and (c) "Reference-locked RF Generators". As explained in the text, the first two methods require SSB sidestep mixing for proper null-point cancellation. Green area indicates locked (and possibly external) components when operating as a coherent MIMO system.

Going through the signal theory for these two configurations, reveals that they are essentially identical in operation. Therefore, only the theory for case (a) will be discussed below. Case (c) shows a different configuration where two RF generators are interlocked through a common reference oscillator while producing RF signals seperated by the IF frequency. Common to all of the configurations is the locking (coherency) between the sampling circuit and the IF generation circuit. As shown below, this is important in order to suppress the phase noise generated in the IF generator circuit.

One of the drawbacks of the sidestep architectures from Figures 2.11(a) and (b), is an increase of spectral components in the sidestep signal, owing to higher order mixing products. To this end, one of the most important design aspects is that a single-sideband (SSB) signal is needed for transmission (or down-conversion in case (b)). This requires that the sidestep mixer is configured as a slightly more complicated circuit, i.e. as an image-reject mixer (IRM). Chapter 3 shows an actual implementation of this type of mixer. [CP1] gives a detailed analysis of the difference between using an SSB sidestep rather than the simpler DSB sidestep. However, to emphasize the importance of this choice, the IF signals obtained by using either techniques are given here in a much simplified form as

$$S_{DSB}(t) = \cos\left(\frac{4\pi}{\lambda_{RF}}x(t) + \frac{4\pi}{\lambda_{RF}}d_0\right) \cdot \cos\left(\omega_{IF}t\right) \tag{2.22a}$$

$$S_{SSB}(t) = \cos\left(\omega_{IF}t + \frac{4\pi}{\lambda_{RF}}x(t) + \frac{4\pi}{\lambda_{RF}}d_0\right) \tag{2.22b}$$

where $\omega_{IF} = 2\pi f_{IF}$ is the IF angular frequency and λ_{RF} is the resultant wavelength associated with the up-converted RF signal. It can be seen from (2.22a), that the baseband signal obtained using a DSB sidestep is merely a sine wave at the IF frequency with the envelope modulated by the chest wall movement. The resultant behaviour is essentially the same as the one for the single-channel homodyne architecture, i.e. null-points and optimum-points will be present and their locations will be determined by the nominal distance to the subject under test, d_0. Contrary to this, in the case of an SSB sidestep, (2.22b) shows that the modulation is placed onto the phase of the IF signal, meaning that the envelope is no longer modulated by the variation in distance, i.e. null-detection points have been eliminated.

Turning towards the architecture of Fig. 2.11(c), the reference source typically operates in the MHz-range. As no sidestep mixing is taking place, neither the received signal nor the down-converter LO signal carries sidebands or image bands. The mixing between the LO signal and the received signal is therefore more ideal and thus does not require any special image-rejection methods. However, RF oscillator circuits that performs well are often more complicated, more bulky and more expensive than simple I/Q mixers, meaning that total system costs will most likely increase. Furthermore, for VSD systems operating as multiple-input-multiple-output (MIMO) systems, as when performing random body movement cancellation, see Section 2.4, it is often more complicated to distribute a common MHz-range reference clock, than a low-IF signal (often in the 1-100 kHz range) as the one needed for the sidestep cases. These two issues are among the reasons for choosing the architecture of Fig. 2.11(a) when implementing the VISDAM prototype radar presented in Chapter 3.

2.3.2 DC Offset Errors in Heterodyne Systems

The digital extraction of the phase information from the sampled return signal is performed using a digital I/Q demodulation (as will be presented in Chapter 4), which basically imitate the same down-conversion steps as was carried out in hardware in the direct-conversion I/Q architecture presented in Section 2.2. This means that, although DC offsets related to imperfections in the receiver electronics are removed with a BPF around the IF frequency, DC offsets related to stationary clutter still show up in the final digital I/Q signal, before arctangent demodulation. The clutter signal now simply have to undergo two down-conversion steps (one in hardware and one in software) before showing up as a static DC offset. This means that, calibration and advanced signal processing steps should still be carried out for proper phase demodulation. Taking into account phase constants, phase noise and any error signals, the down-converted IF signal from (2.22b) can be rewritten as

$$S_{SSB}(t) \overset{\text{BPF}}{\approx} \cos\left[\omega_{IF}t + \frac{4\pi}{\lambda_{RF}}x(t) + \theta_\Sigma \right. \tag{2.23}$$
$$\left. +\Delta\phi_{nRF}(t) + \phi_{nIF}\left(\Delta t\right)\right] + E_C(t)$$

where the time shift, Δt, is given by (2.5) and where

$$\theta_\Sigma \;=\; \Delta\theta + \theta_{IF} \;=\; 4\pi\frac{d_0}{\lambda_{RF}} + \theta_0 + \theta_{IF} \tag{2.24}$$

is a total phase term, consisting of an IF generator offset, θ_{IF}, an offset due to the nominal travel path, d_0, and a phase shift due to the electronics, θ_0; recall (2.10). Furthermore, the clutter signal that will cause a DC error after digital sampling and I/Q down-conversion is given by

$$E_C(t) = E_{Ca}(t) + E_{Cb}(t) + E_{CLO}(t) \tag{2.25}$$

where the individual error components are similar to the the direct conversion error components, although now located around the IF frequency as

$$\begin{array}{c}\textit{Digital}\text{ DC errors}\\ \text{from mixing}\\ \text{(heterodyning)}\end{array}\left\{\begin{array}{lcl} E_{Ca}(t) & \overset{\text{BPF}}{\approx} & C_a\cos\left(\omega_{IF}t+\theta_{Ca}\right)\\ E_{Cb}(t) & \overset{\text{BPF}}{\approx} & C_b\cos\left(\omega_{IF}t+\theta_{Cb}\right)\\ E_{CLO}(t) & \overset{\text{BPF}}{\approx} & C_{LO}\cos\left(\omega_{IF}t+\theta_{CLO}\right)\end{array}\right. \tag{2.26}$$

From (2.24)-(2.26) it is seen that receiver DC offset related errors are completely eliminated. If an analog BPF does not remove the entire DC offset, a digital filter can do this after sampling. Furthermore, although the phase noise from the RF oscillator is still attenuated through the range correlation effect, a new phase noise term shows up, i.e. the phase noise from the IF generator. At the point just before sampling, this phase noise term is not filtered. However, as indicated in Fig. 2.11, the IF generator is locked to the sampling circuitry to form a coherent radar. This means that, the range correlation effect filters the IF phase noise at the moment of sampling, leaving only a fraction of the phase noise in the digitized signal, i.e.

$$\begin{aligned} S_{SSB}(n) \overset{\text{BPF}}{\approx} \cos\Big[&\omega_{IF}nT_s+\frac{4\pi}{\lambda_{RF}}x(nT_s)+\theta_{\Sigma}+ \\ &\Delta\phi_{nRF}(nT_s)+\Delta\phi_{nIF}(nT_s)\Big]+E_C(nT_s)\end{aligned} \tag{2.27}$$

where n represent the discrete-time sample number, $T_s = 1/F_s$ is the sampling period (inverse of sampling frequency) and where

$$\Delta\phi_{nIF}(nT_s) = \phi_{nIF}\left(nT_s-\frac{d_0}{c}\right)-\phi_{nIF}(nT_s) \tag{2.28}$$

is the residual phase noise of the IF oscillator. Further discussion on the signal processing of such VSD signals, are presented in Chapter 4.

2.3.3 Envelope Modulation Caused by Clutter Signals

In the previous section, some effort was put into emphasizing that SSB signals are necessary in order to avoid null-points. Basically, it was sought to obtain a constant envelope in the sampled IF-signal of (2.28). However, when looking at real sampled signals from the VISDAM radar, throughout Chapters 4 and 5, it becomes clear that the envelope is not constant. An example of this, is shown in Fig. 2.12. One reason for the envelope modulation could be that the radar cross section is varied as the chest wall tightens and loosens up during breathing or even that the angle between the chest wall and the radar line-of-sight is varied. However, a far more predictable cause is the clutter signal, E_C, which is located at the same frequency, but with a phase which may or may not be aligned with the signals of interest. To illustrate this mechanism, consider a simple case in which phase noise is neglected such that the IF signal is given by

$$S(t) = A\sin\left(\omega_{IF}t+\frac{4\pi}{\lambda_{RF}}x(t)\right)+\left|E_C\right|\sin\left(\omega_{IF}t+\theta_C\right) \tag{2.29}$$

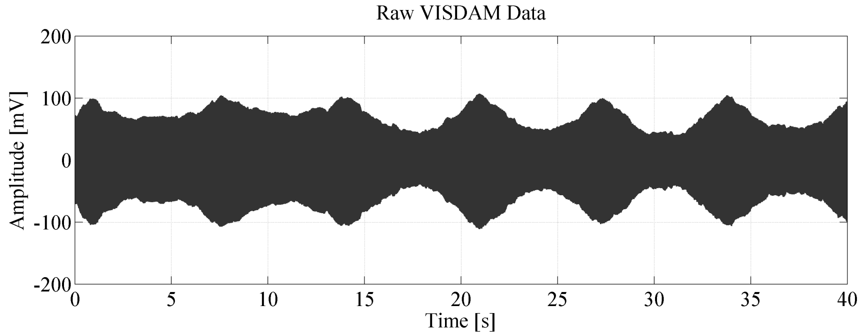

Figure 2.12: An example of a real sampled IF signal, showing a rather high envelope modulation.

where A is an arbitrary signal amplitude and θ_C is the phase difference between the desired signal and a single dominant clutter signal given in the second term. It is rather straightforward to see that if $\theta_C = 180^o$ (i.e. out of phase) the two signals will cancel according to their amplitudes. On the other hand, if they are in-phase they will sum up. The desired signal carries the chest wall modulation, so the phase difference will not be constant. Hence, the amplitude will be modulated. This mechanism is in fact already illustrated with the baseband I/Q signals shown in Fig. 2.9. See for instance the I/Q trace plotted for $\Delta\phi \approx 135^o$ in Fig. 2.9(b). It is clearly seen that the amplitude is not constant over the sample set.

As the clutter signals are stationary, they can be removed by proper calibration, i.e. by measuring the clutter signals before initialising the measurement of the subject. Looking at this problem from an RF-input, IF-input or Baseband-input point of view does not matter. Ultimately, the result is a mere DC offset in the digitally down-converted I/Q signal, as described above. Given that proper calibration is performed there is only one real impact on performance from this envelope modulation; namely that the ADC range is not fully exploited, resulting in a lower signal to amplitude quantization noise ratio.

2.4 Random Body Movement Cancellation Techniques

A big challenge encountered in non-contact vital signs detection is the noise caused by random body movements. These movements are often larger than the movements caused by the respiration and heartbeat signals and thus can severely degrade detection accuracy. Removal of the random body movement signal is therefore an important task, especially for systems intended for use, outside the controlled environment of the laboratory. Schemes for cancellation of these body movements make use of a multi-radar system, measuring from opposite directions of the body, [9, 31, 32]. These techniques assume that while the respiration signal and the heartbeat signal makes the body expand in all directions, the random movement causes a net displacement of the body, see Fig. 2.13. The signals, $x_1(t)$ and $x_2(t)$ can be written as

$$x_1(t) = x(t) + v(t) \tag{2.30a}$$

$$x_2(t) = \beta \cdot x(t) - v(t) \tag{2.30b}$$

where $x(t)$ is given by (2.3), $v(t)$ is the random body movement and where β accounts for the fact that the vital signs responses are not equal in magnitude on both sides of the body. The magnitude of the random body movement signal is assumed to be almost equal for both radars.

Replacing $x(t)$ with $x_1(t)$ and $x_2(t)$ in (2.22b) the IF signals obtained with each radar unit (assuming low-IF VSD radar, transmitting SSB), can be written as

$$S_{SSB1}(t) = \cos\left(\omega_{IF}t + \frac{4\pi}{\lambda_{RF}}\Big(x(t) + v(t)\Big) + \frac{4\pi}{\lambda_{RF}}d_{01}\right) \tag{2.31a}$$

$$S_{SSB2}(t) = \cos\left(\omega_{IF}t + \frac{4\pi}{\lambda_{RF}}\Big(x(t) - v(t)\Big) + \frac{4\pi}{\lambda_{RF}}d_{02}\right) \tag{2.31b}$$

Performing arctangent demodulation on both IF signals and adding the resulting phase signals, results in a combined phase, $\theta_\Delta(t)$, which can be written as

$$\begin{aligned}\theta_\Delta(t) &= \theta_1(t) - \theta_2(t)\\ &= \left[\frac{4\pi}{\lambda_{RF}}\Big(x(t) + v(t)\Big) + \frac{4\pi}{\lambda_{RF}}d_{01}\right] + \left[\frac{4\pi}{\lambda_{RF}}\Big(\beta \cdot x(t) - v(t)\Big) + \frac{4\pi}{\lambda_{RF}}d_{02}\right] \\ &= \frac{4\pi}{\lambda_{RF}}\left(\Big(1+\beta\Big)\cdot x(t) + d_{01} + d_{02}\right)\end{aligned} \tag{2.32}$$

in which the random body movement signal is no longer present. An alternative method is to multiply the two IF signals before arctangent demodulation, to obtain a combined baseband

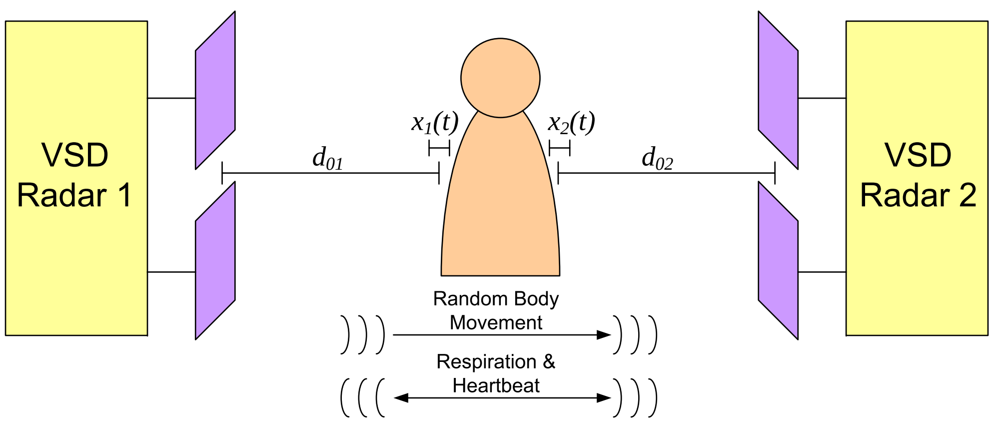

Figure 2.13: Random body movement scheme based on a 2-unit setup measuring from opposite sides of the person being monitored.

signal given by

$$\begin{aligned} S_{\Delta}(t) &= S_{SSB1}(t) \cdot S_{SSB2}(t) \\ &= \frac{1}{2}\cos\left(2\omega_{IF}t + \frac{4\pi}{\lambda_{RF}}\Big((1+\beta)\cdot x(t) + d_{01} + d_{02}\Big)\right) \\ &+ \frac{1}{2}\cos\left(\frac{4\pi}{\lambda_{RF}}\Big((1-\beta)\cdot x(t) + 2v(t) + d_{01} - d_{02}\Big)\right) \end{aligned} \tag{2.33}$$

from which two frequency components are obtained. One is located at DC and carries primarily the random body movement information and the other is located at double the IF frequency carrying only the vital signs information. Digital I/Q demodulation together with arctangent phase extraction can then be applied at $2\omega_{IF}$ to extract $x(t)$. Notice that the DC component carries the same information as would have been obtained if phase subtraction instead of addition was carried out in (2.32).

In the above analysis, it was assumed that both radars were operated at the same RF frequency. For practical reasons this is often not desired, as they will be pointed directly towards each other and thus would disturb the responses obtained. The frequencies should therefore be seperated by at least the IF bandwidth of the system, which for a typical VSD system is in the range of some 3-100 kHz. At such small frequency differences the wavelength, λ_{RF}, of each radar can be assumed to be almost equal, thus validating the above analysis. One common technique for further lowering of the disturbance between the units is to transmit at different polarizations, i.e. one unit can transmit at vertical polarization while the other can transmit at horizontal. This technique also lowers the possibility of saturating the radar receivers.

A final remark to the issue of random movements in general should be given. Today the trend is to integrate more and more features into portable devices such as smart phones and handheld medical equipment. Just as random body movements can obscure the VSD measurements, random movements of the measurement equipment itself can also pose severe degradation of performance. However, as the movements are located at the equipment side, it has been shown that they can be taken into account using for example precise accelerometers and a specially fitted algorithm for position correction, [33]. And this can be done without additional units being present in the radar setup. As the systems considered in this report are all stationary, these techniques for regaining performance in handheld devices will not be given any further consideration.

Chapter 3

The DTU-VISDAM X-band Prototype Radar

The Vital Signs Detection and Monitoring radar, here called VISDAM radar, has been implemented to gain experience with a low-IF heterodyne VSD radar and to verify the theory presented in Chapter 2. Furthermore, it serves the purpose of bringing a real piece of a rather advanced hardware into future microwave and radar courses and projects at DTU. To that end, it was therefore desirable to implement a low-power versatile radar unit with an easy interface. Two identical units have been manufactured to allow for random body movement cancellation setups. Detailed measurements performed on a test group is presented in Chapter 5.

The reason for using X-band is rather simple. Components are readily available and thus rather cheap. Furthermore, this frequency band allows for the microwaves to easily penetrate clothes, pillows and duvets while at the same time not penetrate (that much) into the body of the subject under test. A low-power X-band radar is not suited for through-the-wall monitoring. For this to be an option the carrier should be located somewhere below 3 GHz, perhaps even in the MHz-range. However, as was described in Chapter 2 this then lowers sensitivity. Going to higher frequency bands will give further improvements in sensitivity, but costs will also increase. Nonetheless, increased sensitivity and a much smaller system were the reasons for initiating the SiGe:C IC implementation of this prototype, which operate at K-band, see Chapter 6.

The actual RF design frequency for the prototype has been selected to be 9.45 GHz to lie within the bandwidth (9.05-10.15 GHz) of the implemented PLL/VCO (see below). The danish government, and most of European contries, have allowed bands within this range to be used for low power radio equipment (below 25 mW EIRP), see [34], without the need for a special permission.

The IF frequency is selected to be 1 kHz, which is easy to both generate and sample. Also, this frequency is conveniently far away from DC to implement IF bandpass filters rather easily.

3.1 A General Comment About Power Levels

The radar equation needs to be consulted at least once. Here, a simple form of the equation is used to estimate power levels and thus requirements for dynamic range and noise figure of the VISDAM unit. The received power, P_r, can be estimated as (see [35] for a detailed derivation and treatment)

$$P_r = \frac{P_t G^2 \lambda^2 \sigma}{(4\pi)^3 R^4} \qquad \Leftrightarrow \qquad G_{\text{sys}} = \frac{P_r}{P_t} = \frac{G^2 \lambda^2 \sigma}{(4\pi)^3 R^4} \tag{3.1}$$

where P_t is the transmitted power, σ is the radar cross section of the target, R is the range to the target and where it is assumed that the antenna gain, G, for the transmit and receive antennas are the same. λ is the wavelength of the transmitted signal. G_{sys} can be seen as the system propagation gain experienced from the input of the transmit antenna to the output of the receive antenna.

Estimating σ for a human target at close range is far from an easy task. In [35] a human person is estimated to have a radar cross section of $\sigma = 1$ m^2. However, this is for a full body. In the case of VSD radar, only part of the body is illuminated by the transmit antenna. A plot of G_{sys} is shown in Fig. 3.1 for multiple lower values of σ.

It is seen, that even for the smallest σ and a large range of 4 meters, the loss is no more than 75 dB. This means that even for a transmit power as low as -20 dBm, the receiver will have to collect a signal with a power of approximately -98 dBm. For a narrow band system such as the VISDAM radar, the input power will thus be much higher than the noise floor, indicating that receiver noise figure is not a concern. To reduce the amount of clutter signals, measurements are often taken at smaller ranges where the finite beamwidth of the antenna will collect most energy from the subject under test. This further improves the input signal strength.

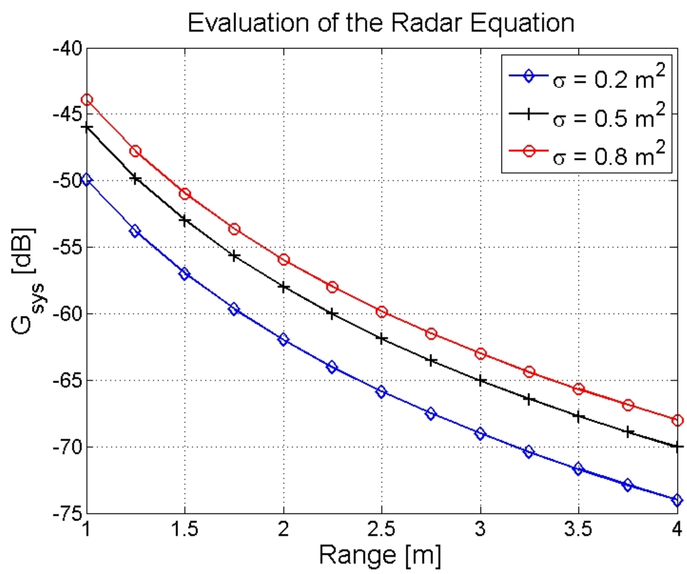

Figure 3.1: Radar Equation: Estimated system gain of VSD radar unit at 9.45 GHz carrier frequency. Antenna gain is assumed to be 10 dBi.

As the target is stationary the input power is rather constant. As such, the instantaneous dynamic range can be low. Here instantaneous refers to the fact that for different ranges and/or angles to the target the input power may vary, and thus the receiver gain might need to be adjusted prior to measuring.

In conclusion, a typical CW-type VSD radar such as the VISDAM unit, can have low, but adjustable, dynamic range with a noise figure which is basically not of concern. This is a major advantage when designing a VSD radar system.

3.2 System Overview

A block diagram of a VISDAM radar unit is shown in Fig. 3.2. It consists of an RF transceiver shown in the yellow area and two IF parts, shown in the green area, that handles IF signal amplification and filtering in the receive path as well as IF signal split in the transmission path. This latter block splits the IF input signal in two parts which are 90 degrees out of phase, and thus effectively operate the I/Q mixer as an image reject mixer (IRM). Further details is given below. The blue area shows the VISDAM control unit and user interface, while the red area shows the power supply unit (PSU) which powers the electronics from a single 15 Volt external supply. The IF input and output is accessible through standard SMA connectors and interfaces to a LabView application through a National Instruments PCIe data acquisition board mounted in a personal computer. Coherent operation is ensured by using the same clock source for both IF signal generation and sampling.

The control unit consists of a PIC18 micro controller unit (MCU) from Microchip Technology Inc. The MCU features an internal EEPROM memory for storing settings, inputtet through the user interface which includes a rotary encoder knop with push function for selection and a 20x2 character display. Custom firmware has been written to implement a display driver as well as an SPI control driver for PLL and IF circuitry setup. The user interface is custom tailored to the VISDAM application and includes decoding of the rotary encoder knop, the control of two seperate frequencies (see below), IF channel selection (I or Q out of receive mixer) and signal amplification. The selection of the IF channel is in theory not necessary. However, as the VISDAM radar is a prototype, this feature has been included to allow testing of different setups in the future.

One of the key components in the VISDAM radar, is the Hittite HMC769LP6CE PLL with integrated VCO. A photo of the PLL sub circuit is shown in Fig. 3.3. It features approximately 12 dBm of output power in the frequency range from 9.05 GHz to 10.15 GHz and has the capability to be operated in the following modes:

- Single Frequency Mode (integer and/or fractional)
- Frequency Shift Keying (FSK)
- Frequency Sweep Modulation (FM)
- Phase Shift Keying (PSK)
- Phase Sweep Modulation (PM)

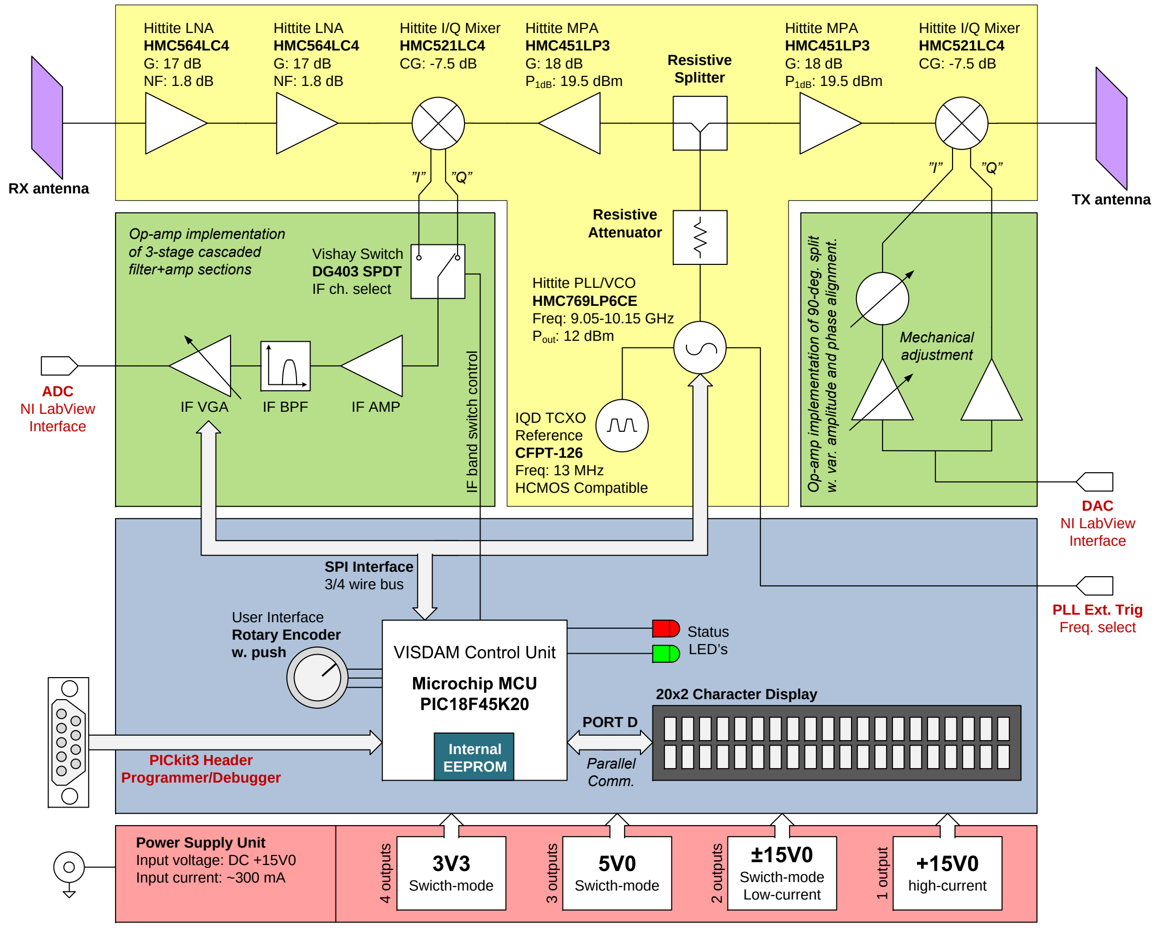

Figure 3.2: Block diagram of the DTU-VISDAM radar.

At the moment of writing, only the FSK mode is implemented in the control unit firmware and by that single frequency operation is also possible. The user can set up two different frequencies with a 1 MHz resolution and then switch between them by placing a logic high (3V3) or low (0V) on the external trigger pin, which is accessible through a standard SMA connector on the VISDAM unit.

The mixer LO inputs are provided through a set of medium power amplifiers (MPA), also from Hittite. This ensures high isolation between the transmit and receive paths as well as a proper LO drive level for the mixers. A combination of a resistive attenuator and a resistive splitter provides an option for tailoring the LO input power to the mixers. Fig. 3.4 shows a photo of a test circuit for the LO split sub circuit together with measurements. Only one MPA is included in the test circuit. With the measured gain (S31) of approximately 4 dB, the mixer LO power level is approximately 16 dBm.

At the transmit side, a single IF signal is provided externally. This signal is then provided as inputs for two active filters in parallel; one lowpass and the other highpass. By tuning the cut-off frequency of these filters to be at the IF center frequency, a 90-degree split is

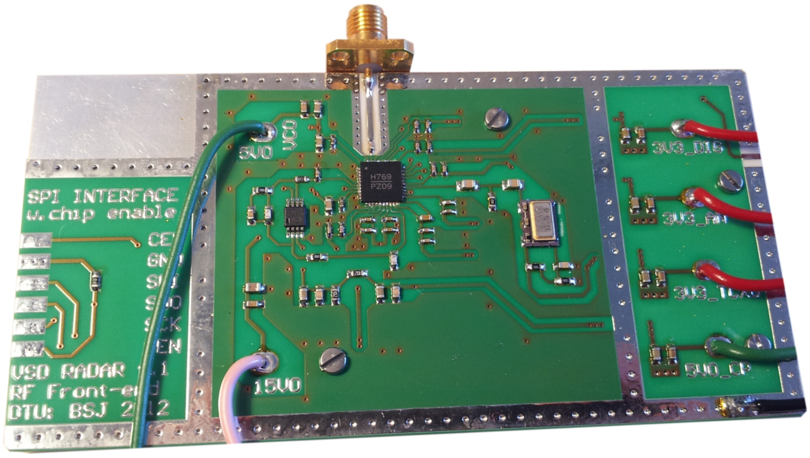

Figure 3.3: PLL sub-circuit using the Hittite HMC769LP6CE PLL with integrated VCO.

obtained. One filter is tunable in both amplification and phase, which allows for optimum IRM operation, taking into account even errors inherent in the transmit mixer. The tuning is done mechanically through two potentiometers.

Although noise figure is not of concern in the VISDAM radar, the RF front-end of the receive path is still implemented with two identical Hittite low noise amplifiers (LNA) providing a theoretic gain of 34 dB before the down-conversion mixer. A photo of the LNA sub

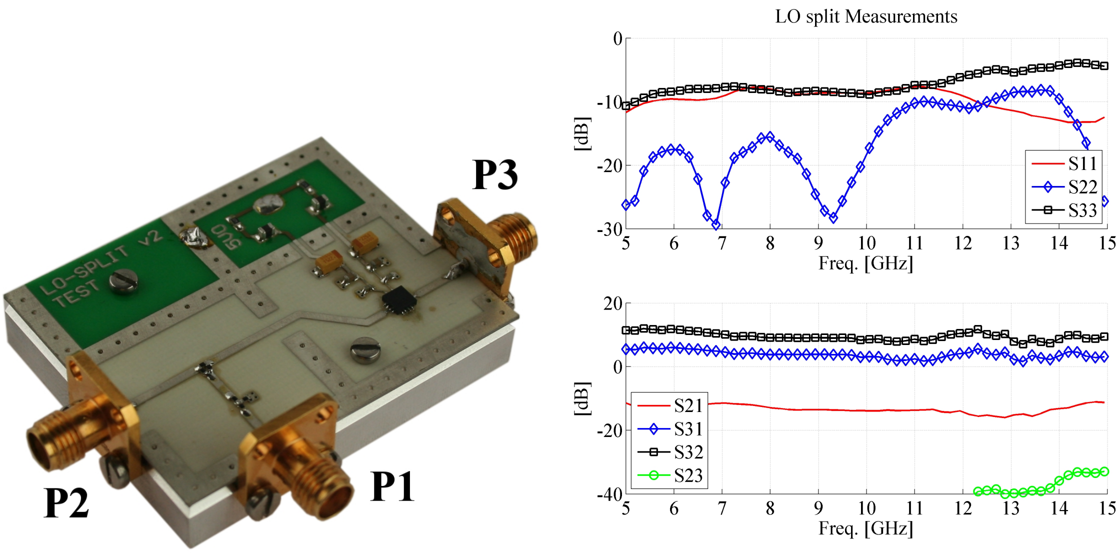

(a) (b)

Figure 3.4: Test circuit for the LO split sub circuit using the Hittite HMC451LP3 MPA as LO buffer. (a) showing picture and (b) showing S-parameter measurements.

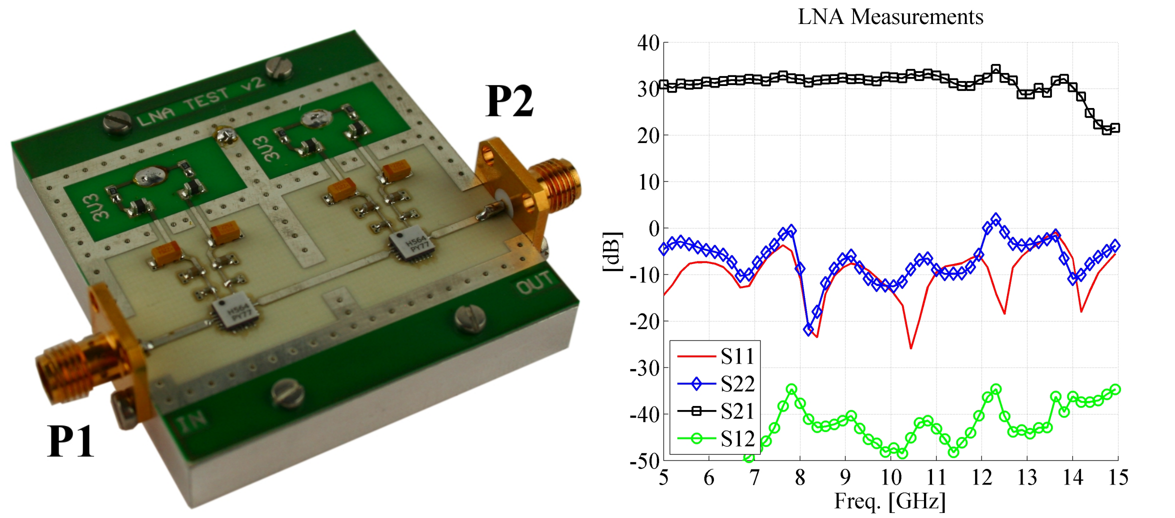

(a) (b)

Figure 3.5: LNA sub circuit using two cascaded Hittite HMC564LC4 LNA's. (a) showing picture and (b) showing S-parameter measurements.

circuit is shown in Fig. 3.5 together with S-parameter measurements, showing a lower gain of approximately 31 dB. The main reason for this difference is the loss in the SMA connector transitions. Taking into account the mixer conversion loss of approximately 8 dB, a total RF gain of approximately 24-26 dB is obtained.

Once down-converted, the IF signal is amplified and bandpass filtered through a three-stage

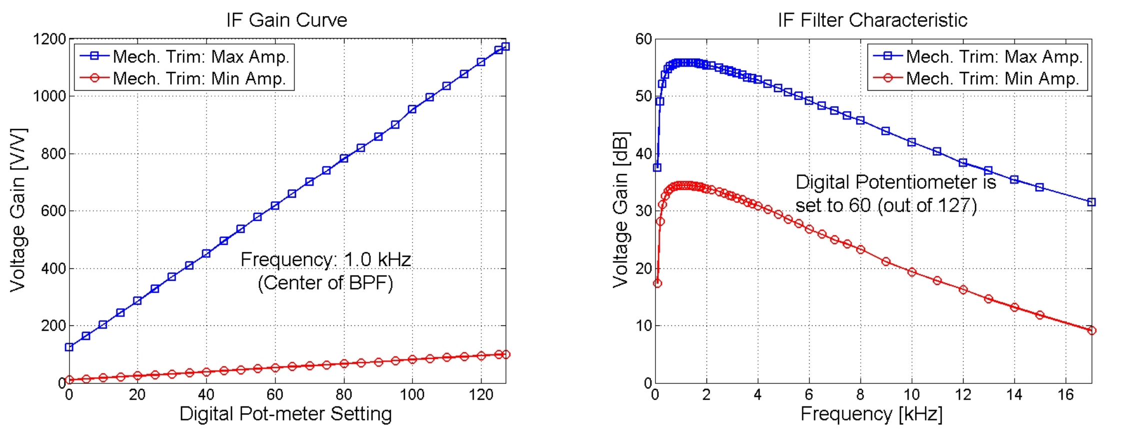

(a) (b)

Figure 3.6: Measured performance of the IF receiver stage. (a) shows voltage gain versus wiper position of the digital potentiometer for the maximum and minimum settings of the mechanically trimmed amplifier stage. (b) shows the BPF response when gain is constant at a digital potentiometer setting of 60 (out of 127).

active filter section implemented with operational amplifiers (op-amp). One of the stages is implemented with a digital potentiometer which then allows for digital control of the IF gain through an SPI interface to the VISDAM control unit. Also, a mechanical potentiometer is implemented in the last stage to allow for further adjustment before use. The measured gain and filter responses of the IF receiver stage is shown in Fig. 3.6. Notice that the gain curve of Fig. 3.6(a) is plottet in linear scale to show the linearity of the gain versus the setting of the digital potentiometer. As seen, the gain is fully adjustable from approximately 10 V/V to 1170 V/V and after setting the mechanical trim, the user is able to adjust gain through firmware, with a full-scale gain factor of 9.5. The supply rails of the IF receiver stage is ±15 V, so at this level, voltage clipping will occur. Furthermore, it is seen from Fig. 3.6(b) that the filter response effectively removes DC components and has a 3 dB upper cut-off at approximately 4 kHz. This helps to remove the sampling frequency of the DAC seen in the generated IF signal.

3.3 Antenna Design

The antennas used in the VISDAM radar are implemented as 2x2 microstrip patch antenna arrays, see Fig. 3.7. Although this type of antenna is rather narrowband, their simple design and reproducibility (even in-house) outshines the limitations encountered in performance; at least for the first prototype.

The reflection coefficient as well as the radiation characteristics of a single 2x2 array antenna were measured at the DTU-ESA Spherical Near-Field Antenna Test Facility [36], see Fig. 3.8. From the reflection measurement, it is seen that the 10 dB bandwidth is approximately 200 MHz (2.14% relative bandwidth) and lies within the band 9.235 GHz to 9.455 GHz. The simulation from ADS Momentum shows a resonance frequency slightly higher than the measured

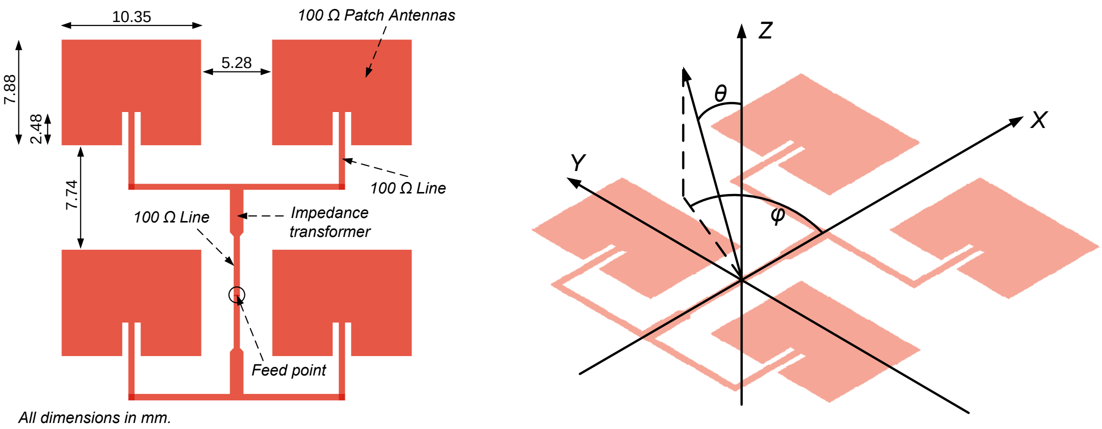

(a) (b)

Figure 3.7: 2x2 microstrip patch antenna array for VISDAM. (a) showing array design and (b) showing coordinate system used for verification in the DTU-ESA antenna test fascility. Notice that ground plane is not shown, see instead Fig. 3.11(a) for a picture of the antenna.

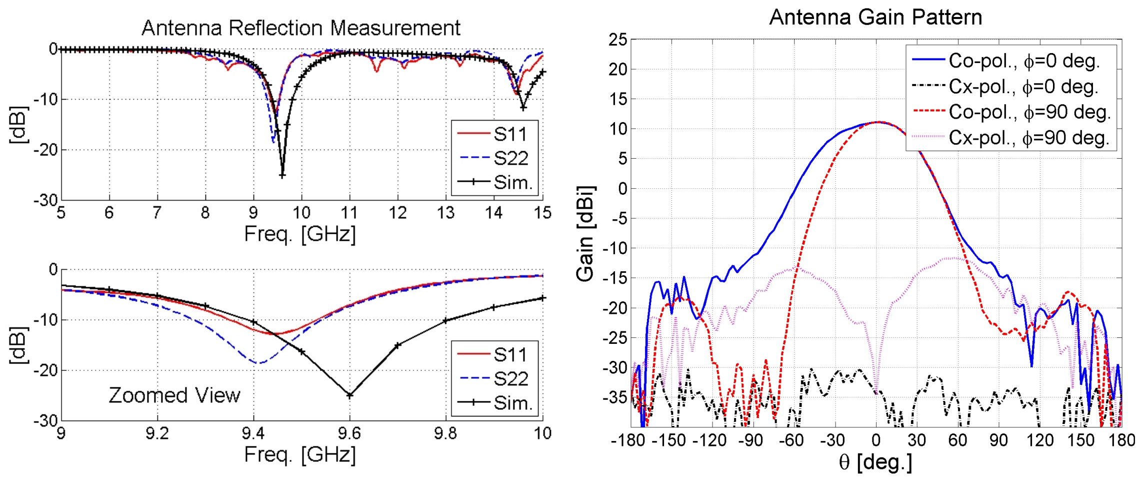

(a) (b)

Figure 3.8: Antenna Measurements: (a) reflection measurement, S_{11}, and (b) gain pattern at mid-band as measured at the DTU-ESA antenna test fascility.

one. This shift is due to an unintended under-etching which occured during the in-house production of the antennas, thus making the antennas slightly larger than intended. As all antennas experienced the same frequency shift and as the location of the resonance is still well within the intended band, it was decided not to tune the antennas further.

The gain pattern shown in Fig. 3.8(b) reveals that the antenna is rather symmetrical around the $\theta = 0$ direction where the gain peaks at approximately 11.1 dBi. This is fairly close to EM simulations done with ADS Momentum (known to underestimate loss) which predicted a gain of approximately 12.0 dBi. A small asymmetry is observed for both $\phi = 0$ and $\phi = 90$ degrees and can be explained by the intervention of the feed lines. The 3 dB beamwidth is approximately 58 degrees and no severe side- or back lobes are present. As intended, the antenna polarization is highly linear and vertical, with a cross-polarization component more than 26 dB down from the main lobe at all angles and more than 40 dB down in the main lope direction.

During measurements the target should be located in the far-field. The boundary between near- and far-fields can be estimated through, [37]

$$R_{ff} = \frac{2D^2}{\lambda} = \frac{2 \cdot 0.1^2}{c/f} = 0.63 \text{ m} \tag{3.2}$$

where D is the largest diameter of the antenna, which in this case is approximately 100 mm taking into account most of the ground plane to overestimate the antenna size and thus the range to the far-field. It can be concluded that at a distance of 1 meter, the subject under test is for sure in the far-field region.

The final placement of the antennas should seek to lower the cross-talk between the transmitter and receiver. At the same time, it is desirable to place the antennas close to each

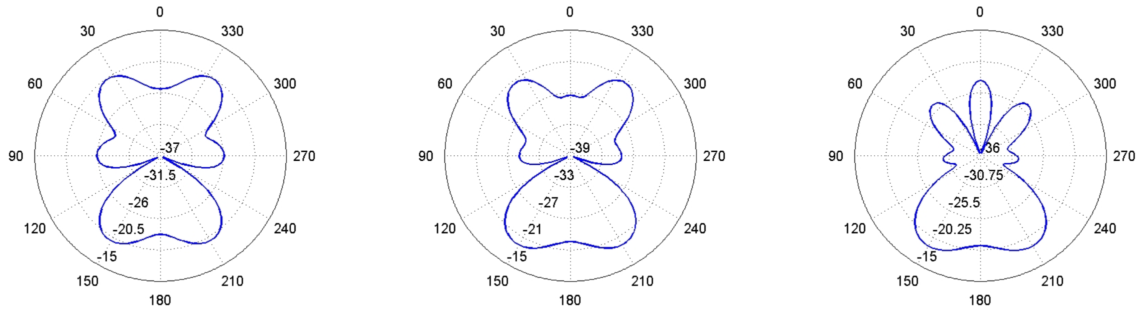

(a) **(b)** **(c)**

Figure 3.9: Simulated antenna pattern for $\theta = 90°$, at (a) 9.4 GHz, (b) 9.6 GHz (simulated center) and (c) 9.8 GHz. Simulation performed with ADS Momentum.

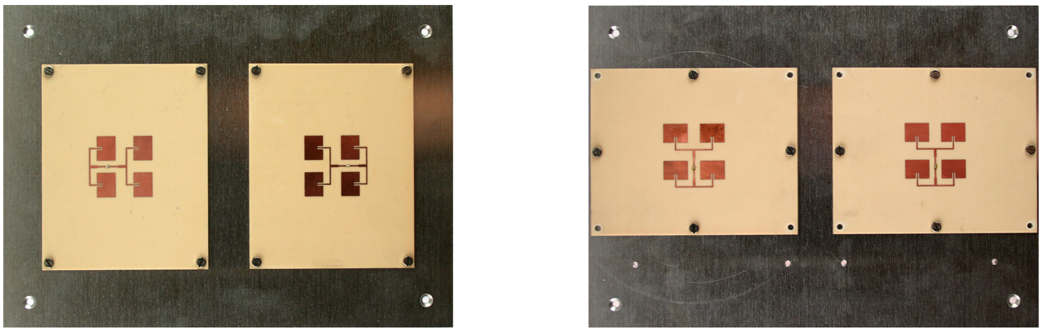

(a) **(b)**

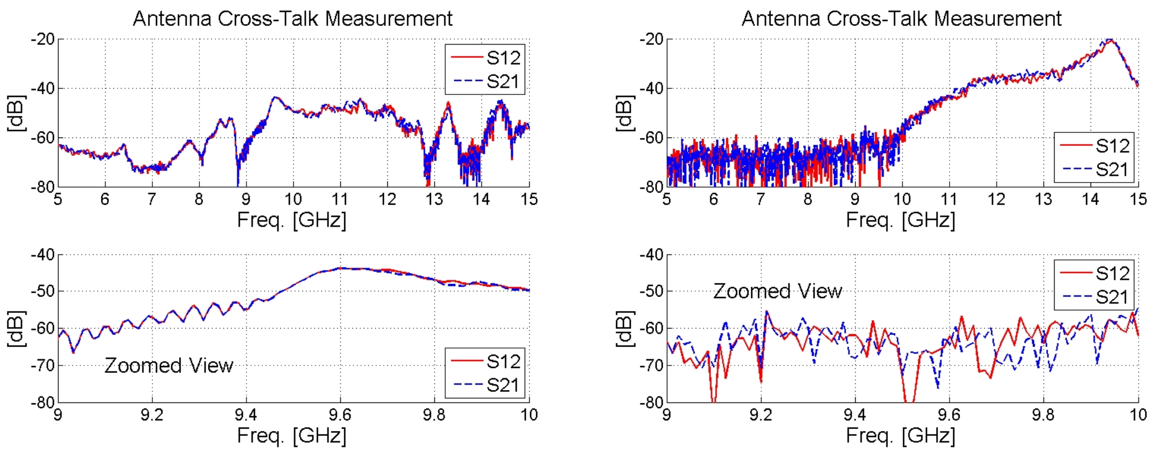

(c) **(d)**

Figure 3.10: Two antenna setups with (a) showing the non-optimized and (b) showing the optimized antenna placement while (c) and (d) shows the cross-talk measurements of the two placements, respectively. Measurement is done with a 2-port VNA and absorbers placed in front of the antennas.

other to ease both mechanical mounting (to interface to the RF unit) and radar aiming, i.e. lowering the pointing angle to the target. To decide on the antenna mounting scheme, the simulated radiation pattern for $\theta = 90^o$ is shown in Fig. 3.9 at three different frequencies within and near the antenna bandwidth. Notice again that this is for the simulated response which was at 9.6 GHz center frequency. It is clearly seen that the gain is strongest in the $\phi = 0^o$ and $\phi = 180^o$ directions. So placement of the antennas should be such that they are side-by-side, i.e. such that the feed networks point in the same direction.

To verify the choice of antenna placement, two different mounting positions were fabricated and measured, see Fig. 3.10. By placing microwave absorbers in front of the antenna mount, the cross-talk was measured using a 2-port VNA. For the non-ideal positioning, cross-talk at center frequency is approximately -55 dB. Also for this configuration, it is seen that cross-talk increases drastically right next to the center frequency. The reason for this increase is seen from Figures 3.9(a) and (c), where a small artifact of rather high gain is seen in the $\phi = 0^o$ direction, i.e. in the direction of the opposite antenna. Mounting the antennas in the direction shown in Fig. 3.10(c) it is seen that the cross-talk is improved considerably, obtaining now a cross-talk component of approximately -65 dB. Furthermore, the cross-talk is much more flat and especially does not increase as drastically at the sideband frequencies.

Depending on the physiological condition of the person under test as well as the distance to the person, this antenna cross-talk level might give rise to a DC-component (as explained in Section 2.2.4) so large as to affect the measurements in a destructive manner. This is why calibration is performed, see Chapter 4.

One final remark, as to the way the antenna positioning was optimized. The radiation patterns shown in Fig. 3.9 are for the far-field region, so strictly speaking these patterns are not valid seen from an antenna-to-antenna point-of-view. However, they indicate the general behavior, which is also shown in the measurements.

3.4 System Assembly and Verification

Figure 3.11 shows some photos of a complete VISDAM unit. The casing is custom made at the DTU-Electro / DTU-Photonics mechanical workshop. The RF design comprise a single PCB containing all sub circuits. To increase isolation between these, ground rings without solder mask has been placed for electrical connection between the PCB and a custom made milled frame. These ground rings are clearly seen in Fig. 3.3-3.5. The entire RF part is subdivided into 20x20x15 mm (width, length, height) compartments such that the cavity resonance frequency is located at approximately 10.6 GHz, see chapter 6 of [38]. Furthermore, this design helps to improve isolation between the transmit and receive paths. A threaded hole for standard camera mounting is placed in the bottom of the casing to allow easy mounting on a tripod and/or a custom made platform.

The antenna mounting is not permanently fixed to the casing. Instead, semi-rigid coaxial cables are used for connection between the antennas and the radar RF electronics. This makes seperate testing possible, even after assembly. And furthermore, it ensures that new antennas

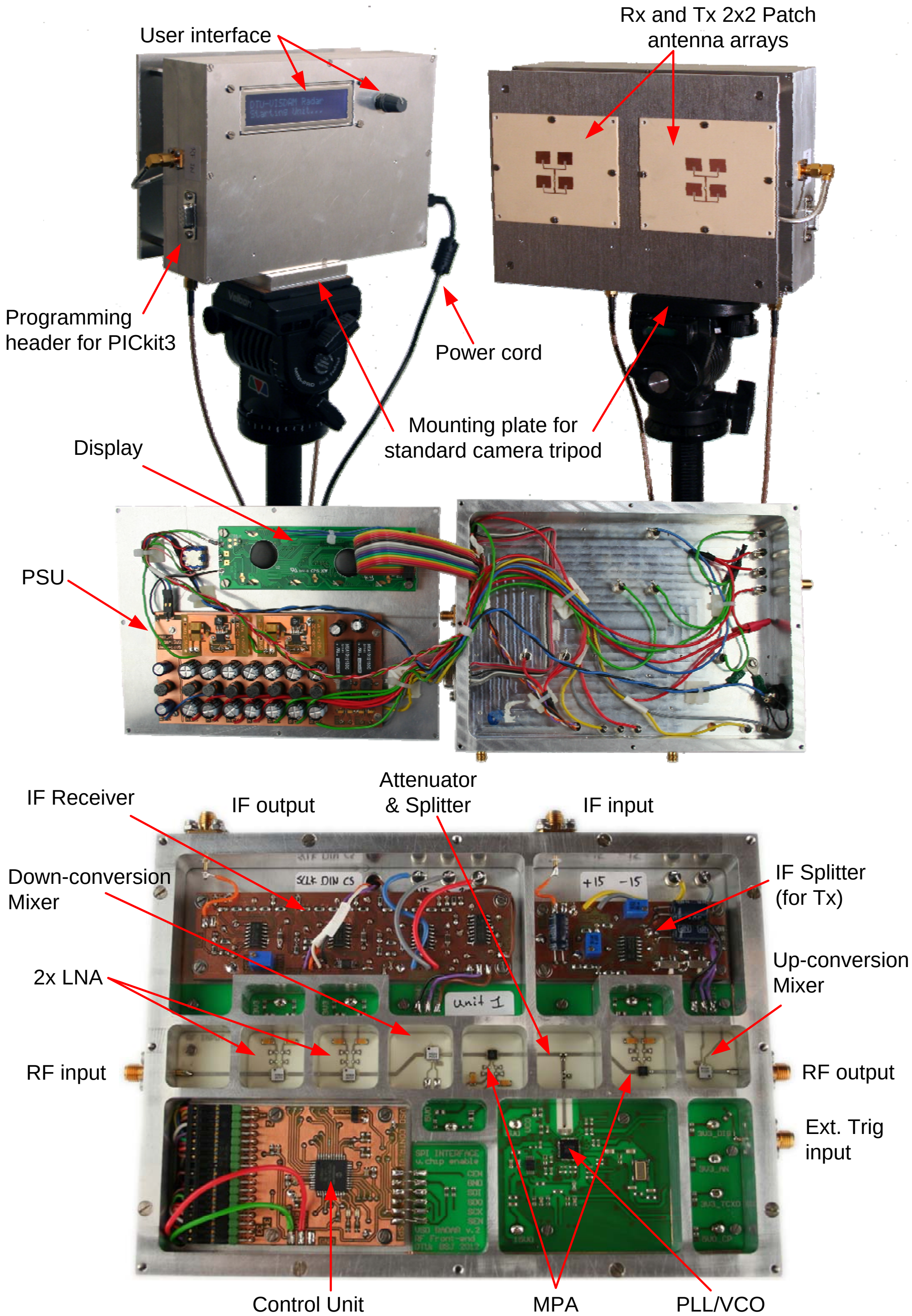

Figure 3.11: Pictures of the VISDAM radar unit.

	Performance	Units
RF Bandwidth (RF radar front end)	9.05 - 10.15	GHz
RF Bandwidth (including antennas)	9.235 - 9.455	GHz
Image Reject Ratio (output)	> 45	dB
Transmit Power	-40 to 0	dBm
Antenna Gain (both Tx and Rx)	11.1	dBi
Antenna Cross Talk (Tx-to-Rx)	< -65	dB
IF Center Frequency	1.0	kHz
IF Bandwidth	3.0	kHz
Tx-Rx Isolation (RF front-end)	75	dB
Supply Voltage	15.0	VDC
Power Consumption	5.25	W

Table 3.1: Performance parameters of the VISDAM radar unit after assembly.

can be developed at a later point without the need for a new front-end unit.

The performance of the complete unit is summarized in Table 3.1, with some of the most important parameters being the image reject ratio in the transmit signal and the transmit-to-receive isolation (in hardware alone). The latter has been measured by terminating both the RF output (Tx) and input (Rx) in 50 Ω loads and then measuring the IF output signal level. Also listed is the measured antenna cross coupling when mounted on the final back plate. Comparing the Tx-Rx isolation to the antenna cross-talk component, it is evident that the latter will dominate the C_a clutter offset component, see Fig. 2.7. The output power measurement depends upon the IF input signal level. This is measured at levels where the image rejection is unchanged.

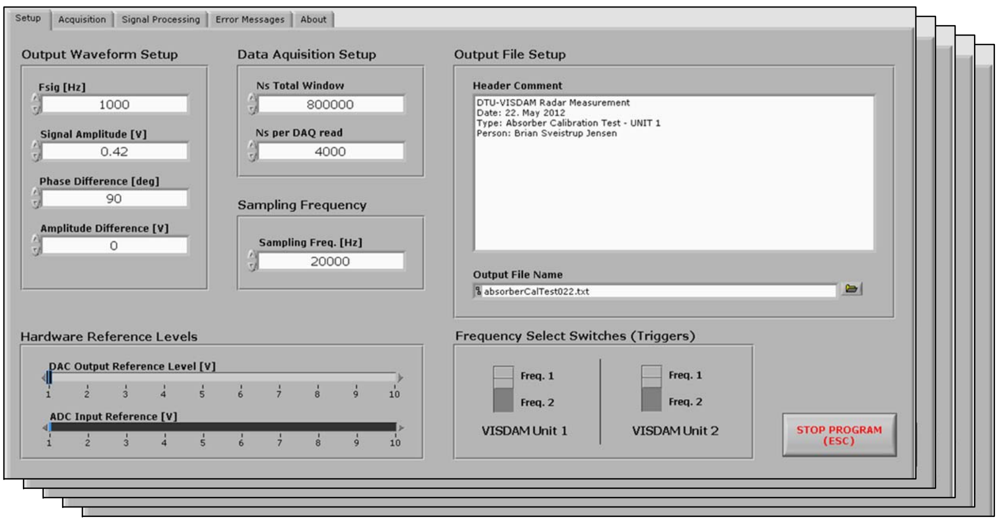

Figure 3.12: Screendump of the NI LabView VI acting as user interface for the VISDAM radars.

3.5 IF Data Generation and Acquisition

As indicated in the block diagram of Fig. 3.2, IF signal generation and acquisition is performed using a National Instruments (NI) PCIe-6251 DAQ card interfacing to an NI LabView Virtual Instrument (VI) acting as the user interface. A screendump of the VI setup- and acqusition pages is shown in Fig. 3.12. The user can set up two individual IF output signals with the same frequency but with selectable amplitude- and phase differences. Furthermore, the user can specify sampling frequency as well as the window size for data acquisition. Once data acqusition is stopped, the acquisition window is automatically stored on disk as a tab-delimited text file.

The physical connection is shown in Fig. 3.13(a). As seen, eight individual channels are

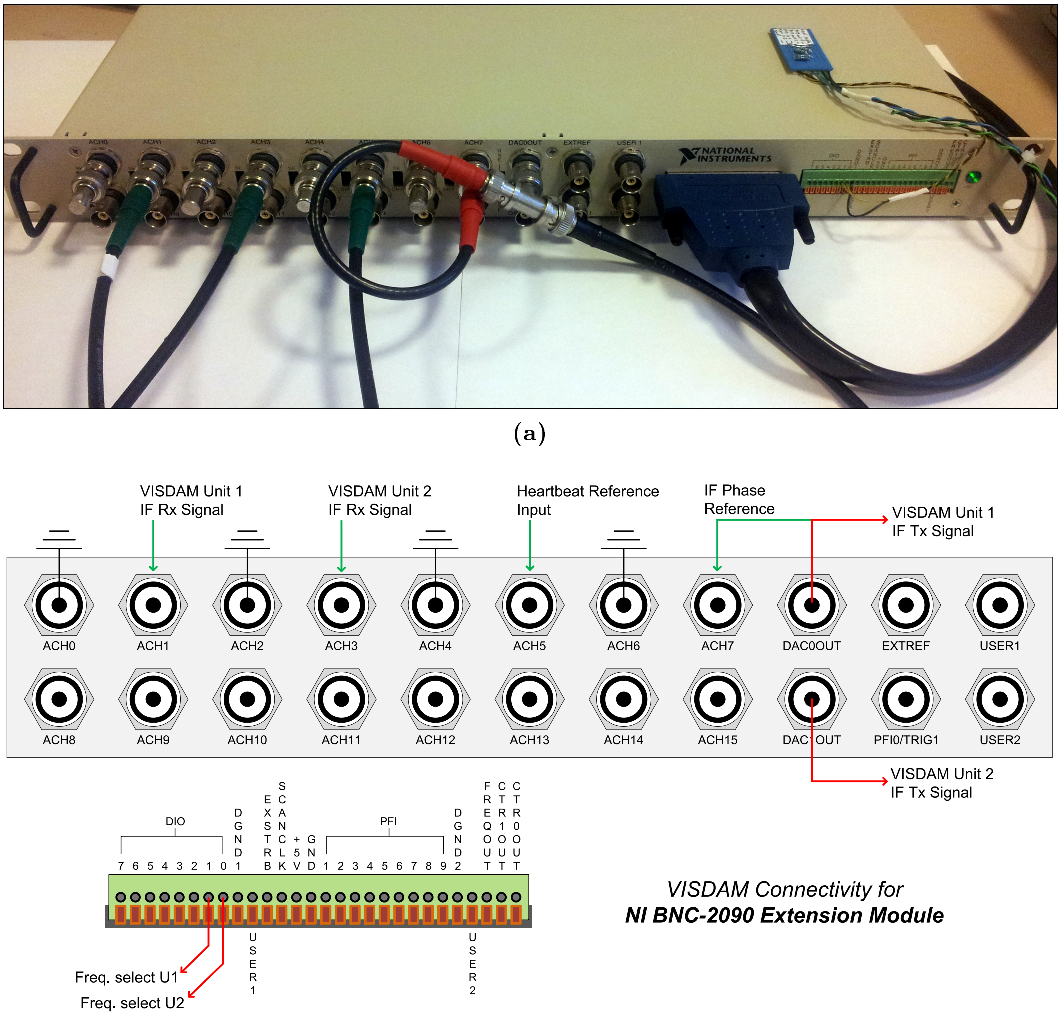

(a)

(b)

Figure 3.13: Physical connection between VISDAM units and NI DAQ card showing (a) photo of the NI BNC-2090 extension module (b) connectivity diagram.

inputtet to the hardware and sampled by the VI. Channels 1, 3, 5 and 7 are the actual input channels, which includes two radar inputs, a heart rate reference signal and a phase reference taken from the output. Channels 0, 2, 4 and 6 are terminated to GND to help reset the sampling circuit which is connected to each channel through a mux. Without this special configuration, the isolation between channels is poor. The reference signal is used for phase alignment between each measurement. This is important for aligning calibration data to measurement data, see Section 4.2.

Frequency selection for each VISDAM unit is performed on the setup page. The 5 V digital levels from the PCIe-6251 DAQ card is run through a level shifter (resistive divider) to obtain the 3.3 V levels required by the VISDAM units, see Fig. 3.13(b).

3.6 Summary on the DTU-VISDAM Implementation

As will be shown in Chapters 4 and 5 the DTU-VISDAM radar is able to detect both respiration and heart rates on human beings. The present state of the VISDAM system is versatile and highly reseach oriented in that it requires special equipment for data acquisition and Matlab for post-measurement signal processing (described in Chapter 4). As such; many steps could be taken to improve both performance and the user experience. These include the following:

- For a more versatile system, the antennas should be designed for a more broadband performance.
- The internal isolation should be controlled better. At the moment a combination of cobber foil and conductive paste is ensuring isolation.
- Consider using slightly higher IF frequencies, i.e. 10 or even 100 kHz to be sure that 1/f noise in the IF circuitry do not influence performance too much (also see comments in Section 5.2).
- Reduce size and weight considerably. This should be possible on a second version of the DTU VISDAM radar.
- Implement DSP units (i.e. DSP-MCU and/or FPGA) to make realtime tracking possible.
- Implement a more standardized interface to the computer, i.e. USB, LAN or WiFi, to facilitate the use of more units on a computer without speciel hardware, i.e. for example a laptop.
- Implement result/control interface in a stand-alone software package.

Many of these suggestions for improvements are especially suitable for further development towards a commercialization of the radar system.

Chapter 4

DTU-VISDAM Signal Processing and Calibration

Although the PhD project has been more about hardware than software, it is unavoidable and necessary at some point to consider the digital signal processing (DSP) of the acquired VISDAM data. This chapter introduces the signal processing steps performed to extract both respiration- and heart rate information from the radar data. The theory does not cover all aspects related to processing of radar signals containing vital signs information. However, it will be adequate to analyze the radar response from VISDAM.

Furthermore, this chapter will describe how VISDAM data are calibrated/corrected to remove the most dominant clutter components. The performance of this DSP step is evaluated on a real sample set obtained with VISDAM.

All signal processing steps are performed with Matlab. The Matlab function set developed for VISDAM is included on the appended DVD. For a listing of the DVD content see Appendix 9.

4.1 Characteristics of the Raw VISDAM Data

A 40 second window of a raw sample set obtained with VISDAM is shown in Fig. 4.1. One of the reasons for using a low-IF heterodyne architecture with SSB signal transmission, was to get rid of null-points and thus keep the envelope constant, see Section 2.3.1. Yet it is seen from the raw input signal that the envelope is still modulated slightly. As discussed in Section 2.3.3 three reasons for this is identified. These includes limited image-rejection in the transmitted SSB signal, modulation of the radar cross Section of the chest wall and finally interference by clutter signals, i.e. antenna cross-talk signals etc. The two latter are thought to be the major causes.

From the frequency spectrum of the data, a strong signal is showing up at ± 1 kHz indicating that the IF frequency is located at 1 kHz offset. Zooming into the location of the positive 1 kHz carrier, it is already now apparent, that some modulation has taken place. For example, the spectral peaks near 1.0 Hz offset from the IF carrier, indicates some activity at approximately

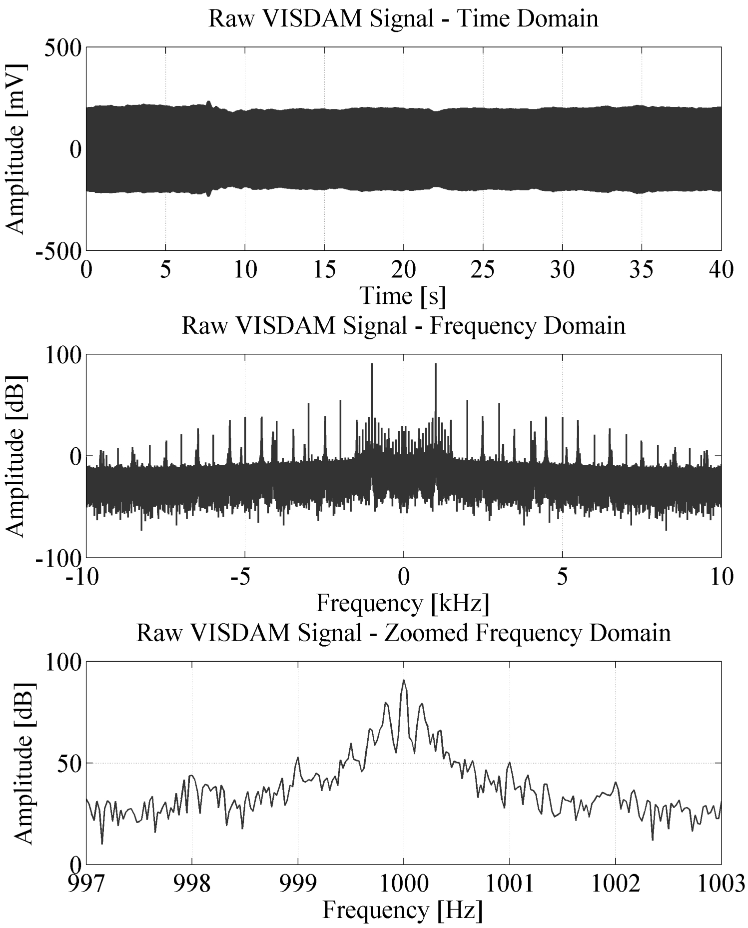

Figure 4.1: Raw VISDAM data. From the top showing raw time domain signal, full frequency domain and frequency domain zoomed to the 1 kHz IF carrier. Some activity is seen at approximately 1000±1 Hz indicating a periodic heartbeat signal at 60 bpm.

$1.0 \cdot 60 = 60$ bpm. As will be apparent in a few DSP steps, this is in fact the heartbeat signal of the person under test. Also, the respiration signal is showing up at approximately 0.2 Hz offset indicating a respiration rate of approximately 12 bpm.

4.2 Calibration and Extraction of Amplitude and Phase Information

The general procedure for extraction of the amplitude and phase information through a digital I/Q demodulation is outlined in Fig. 4.2. In general, two measurements are used, i.e. a vital signs measurement and a calibration measurement, both of which includes a reference signal for phase alignment between measurements taken at different times. This phase reference is

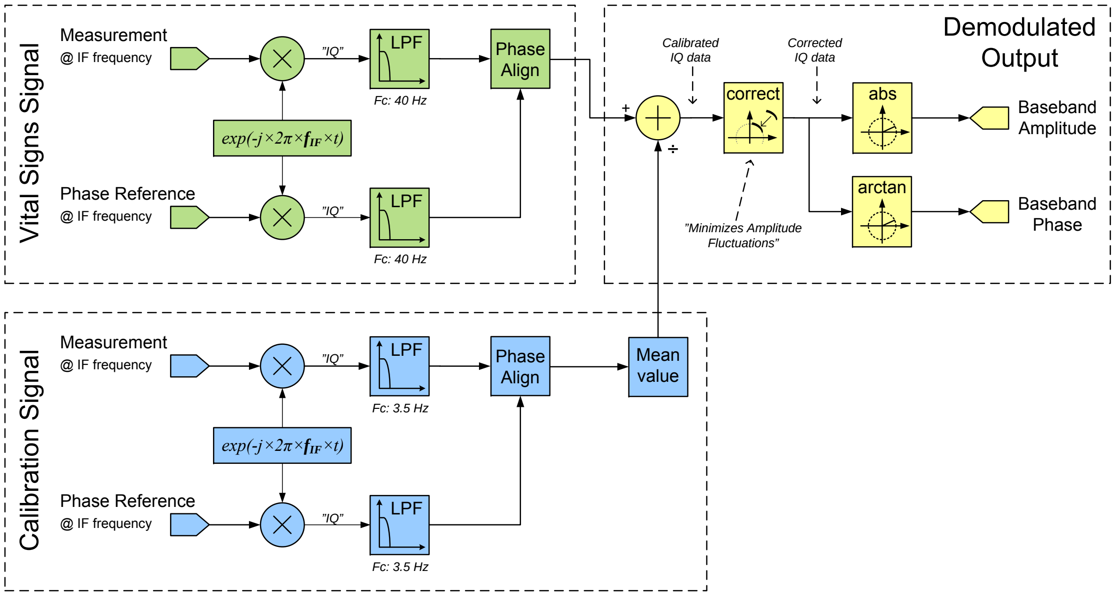

Figure 4.2: General procedure for amplitude and phase extraction through digital I/Q demodulation.

simply a loop-back of the outputted IF signal, see Fig. 3.13 in Section 3.5.

The first step in the demodulation is to down-convert the input signal using a cyclic rotation of the spectrum. In other words, baseband I/Q data are obtained by multiplying a complex carrier at the IF frequency, f_{IF}, onto the input data. Mathematically this first step can be written as,

$$B_{IQ}(n) = I(n) + j \cdot Q(n) = S(n) \cdot e^{-j \cdot 2\pi \cdot t(n) \cdot f_{IF}} \tag{4.1}$$

where $S(n)$ is the input IF data, $t(n)$ is the time vector and where $B_{IQ}(n)$ holds the I/Q representation of the baseband signal as shown. The reason for the minus sign in the exponential, is to rotate the spectrum backwards, such that the positive frequencies are down-converted. In essence, this is not important for extraction of the mere periodicity of a signal. However, using the positive part of the spectrum, ensures that the signal is not complex conjugated, [39]. Fig. 4.3 shows the rotated spectrum of the sample set presented above.

Once the baseband I/Q signal is obtained, a low pass filter (LPF) is applied to the data. A FIR filter with a cut-off frequency of 3.5 Hz (210 bpm) and based on a Chebyshev type window has been used for the calibration data while the same filter type, but with 40 Hz cut-off, is used for the VISDAM data. The 40 Hz filter is selected to remove the wall outlet net frequency of 50 Hz, while preserving most of the heartbeat signal characteristic. Using a FIR type filter, a linear phase transformation through the filter is ensured. After LPF, the complex signals from both the calibration and VSD signal, are phase corrected using the reference phase acquired during each measurement. This ensures that the calibration data can in fact be referenced to the VSD signal. Fig. 4.4 shows the I/Q-plot of the sample set before and after filtration and after phase correction. The latter is scaled in amplitude according to the reference. Although somewhat distorted, the filtered I/Q-plot is similar to the theoretical examples presented throughout Chapter 2.

Next the VSD measurement is corrected using calibration data obtained from a cross-talk calibration measurement, see Fig. 4.5. This measurement is taken while the radar unit is

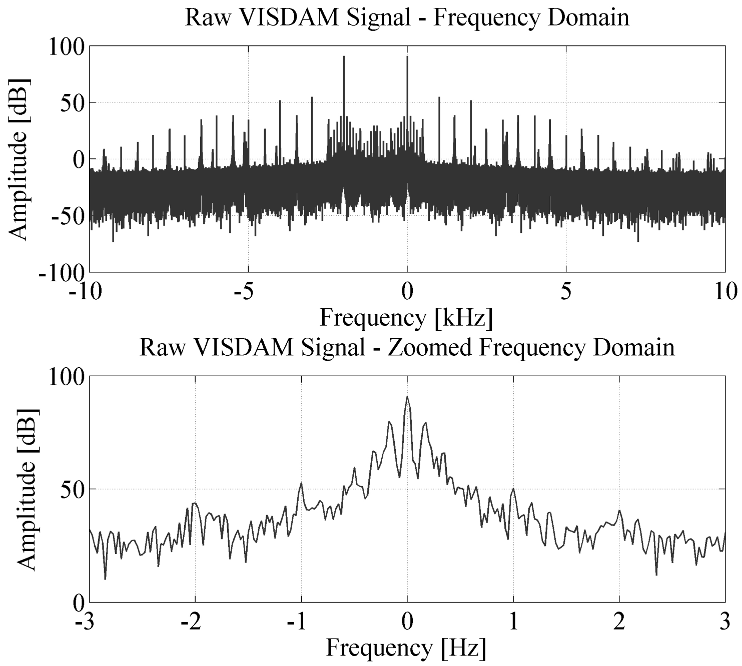

Figure 4.3: Spectrum after cyclic rotation (down-conversion). Top shows full spectrum, and bottom shows zoom to DC.

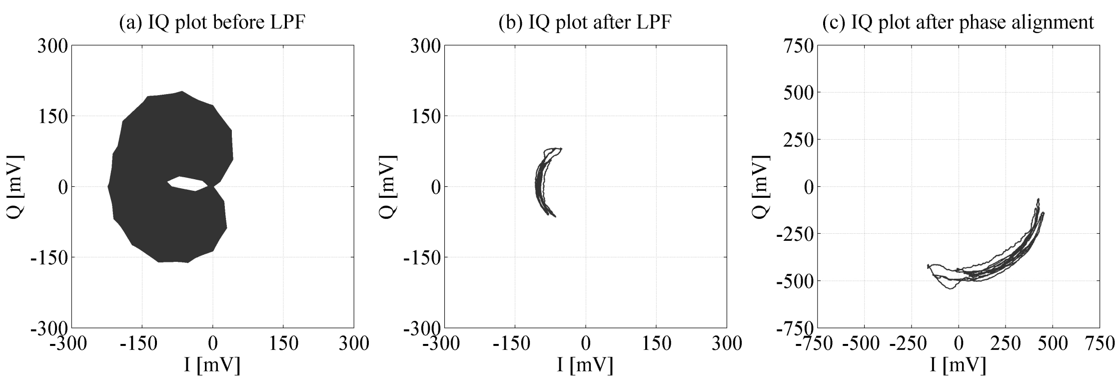

Figure 4.4: I/Q plots of the sample set. From the left: Before LPF, after LPF and after phase alignment. Notice that the latter is scaled in amplitude according to the reference. Calibration data are not shown.

pointed into a microwave absorber to shield it from the surroundings. This ensures that only the antenna cross-talk (and internal cross-talk) component is measured.

As seen in Fig. 4.2 the first two DSP steps encountered by the calibration measurement are identical to the ones used for the VSD input data. As the calibration data are not modulated, they resemble ideally a single point DC measurement in the I/Q plane. The mean value of the calibration data is calculated to remove noise and then this calibration point is subtracted from the VSD data to obtain a corrected response.

During measurements, it was quickly realised that because clutter signals are too high, cross-talk calibration is often not sufficient for proper detection. The calibrated signal is therefore run through a simplified *best circle fitting* algorithm which basically has the same purpose as the Levenberg-Marquardt algorithm implemented in [28]. It fits the data to a circle with origin near (0,0) by running through a number of DC offset points around the calibrated data and finding the point at which the standard deviation of the amplitude signal is lowest, i.e. where the amplitude variations are smallest. Fig. 4.6 shows the original I/Q plot together with corrected plots using antenna cross-talk calibration alone and cross-talk calibration plus the additional curve fitting. In this particular case, it is seen, that the calibration step alone, Fig. 4.6(b), actually has a negative effect on the DC adjustment, as the curve is moved too much down in the I/Q plane. However, the curve fitting algorithm compensates for this problem as seen in Fig. 4.6(c). It can be argued that calibration is in fact unnecessary, at least when only a simple cross-talk calibration is performed. From the corrected I/Q data, the signal amplitude and phase can now be extracted.

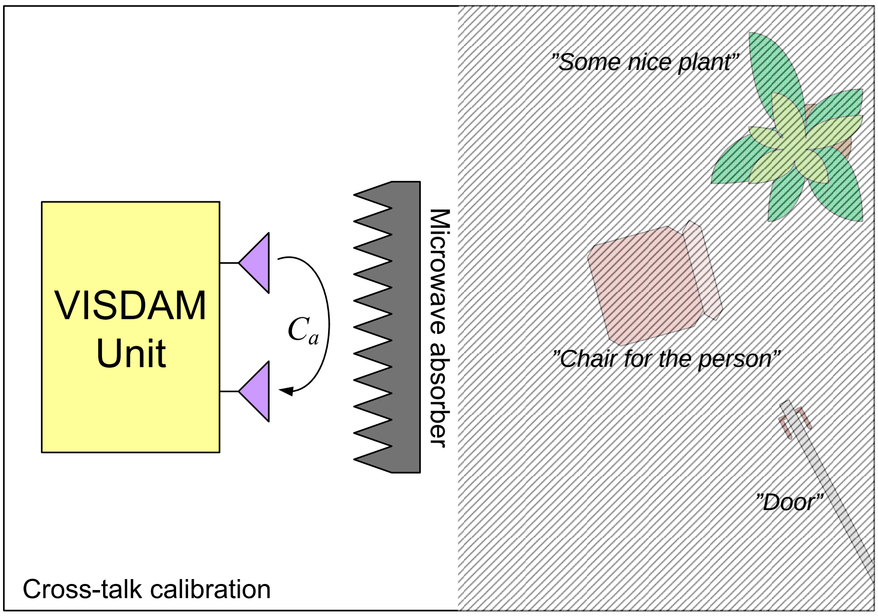

Figure 4.5: Cross-talk calibration procedure using microwave absorber to shield the radar from the surroundings.

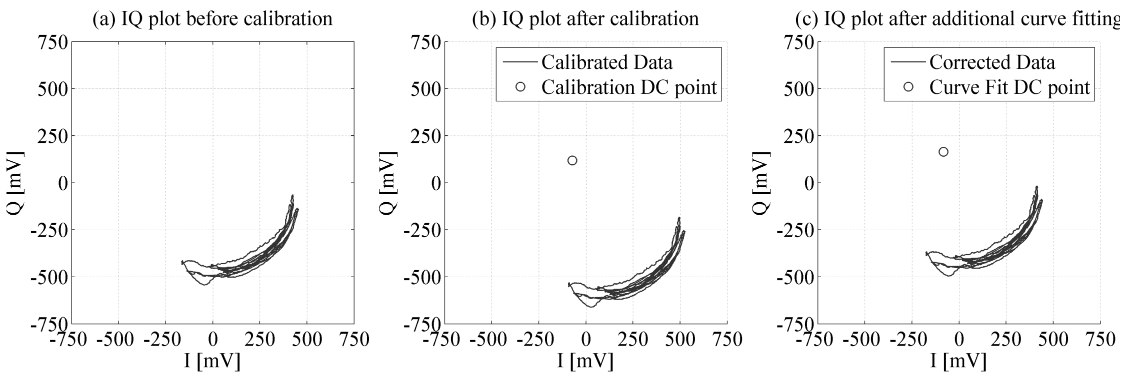

Figure 4.6: Original I/Q plot (a) together with corrected plot (b) using antenna cross-talk calibration alone and with additional curve fitting (c).

4.3 Analysis of Extracted I/Q Signals

The FFT spectra presented above were applied to the entire 40 second sample set window and gives a good indication of the heartbeat and respiration rate measures. However, a more real-time tracking of especially the heartbeat signal is desired. The analysis method performed on the output phase signal from Fig. 4.2 is shown in Fig. 4.7.

As the sampling frequency is much higher than needed, the first step in the analysis is to down-sample the phase signal to a sampling frequency of 100 S/s. This is approximately a factor 20 of the maximum frequency present (≈3.5-5 Hz) in the phase signal after the LPF operation in the I/Q demodulation. Down-sampling the phase signal will make storing of the data take up less memory and ease the computer power requirements for the following analysis steps.

After down-sampling, the next step is to filter the phase signal, to obtain seperate signals containing respiration or heartbeat signals. Fig. 4.8 shows these two signals when extracted from the data set presented above. The filtering start-up behaviour, seen in the beginning

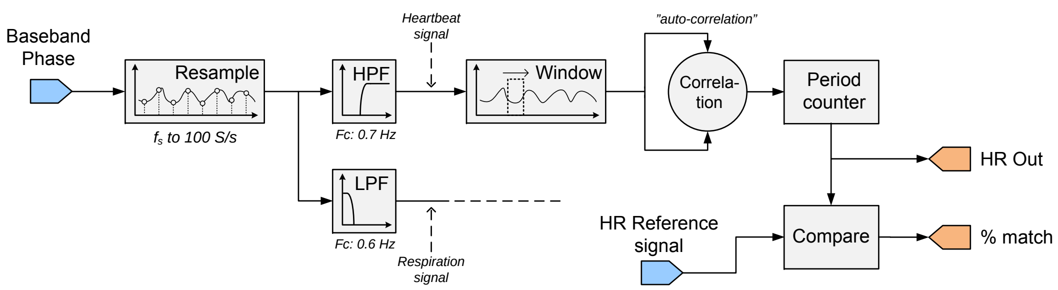

Figure 4.7: Analysis method for tracking of heartbeat signal and comparison to reference data.

of each signal is of no importance, as long as the distorted data are neglected in the further analysis. From this point on, we will concentrate mainly on the heartbeat signal. However, analysis steps for evaluation and tracking of the respiration rate is identical to the ones described below.

Having isolated the heartbeat signal, a moving window is applied for tracking of the heart rate. The required window size (time and number of samples) can be calculated as

$$T_{win} = \frac{N_{hb}}{HR_{min}/60} \quad \Leftrightarrow \quad N_{win} = \frac{N_{hb} \cdot f_s}{HR_{min}/60} \tag{4.2}$$

where N_{hb} is the required number of heartbeats for proper detection, HR_{min} is the minimum expected heart rate in units of [bpm] and where f_s is the sampling frequency of the data, i.e. 100 S/s in this case. HR_{min} is set to 45 bpm (0.75 Hz) and N_{hb} is nominally set to 3, but

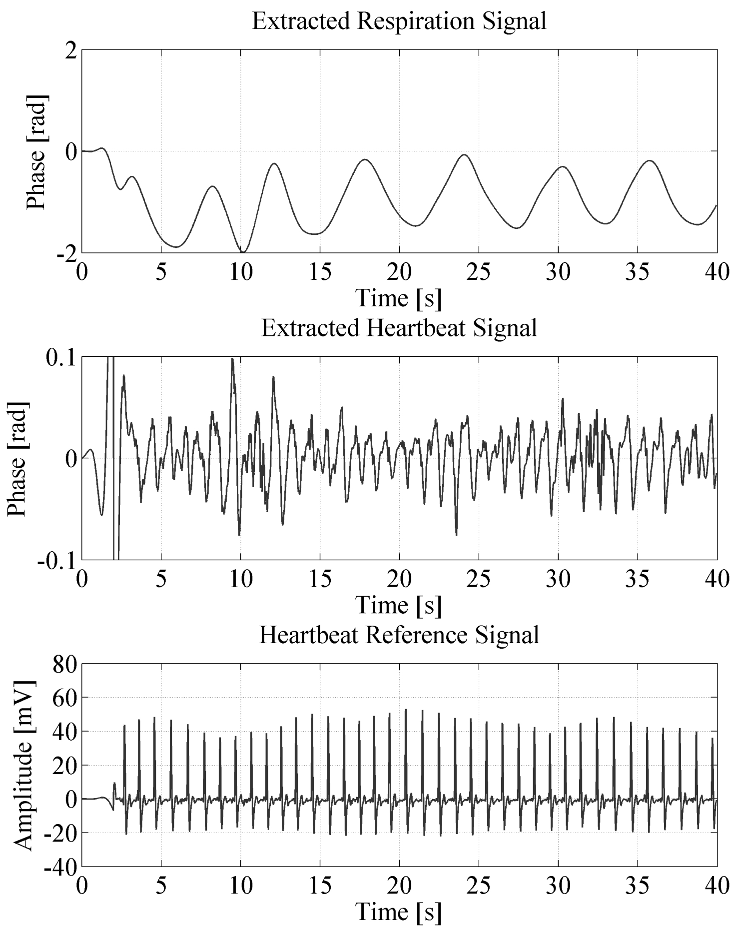

Figure 4.8: Extracted respiration and heartbeat signals after down-sampling and filtering. Bottom plot shows the heartbeat reference signal obtained with a finger pressure transducer.

is varied to assess performance based on window size. Using (4.2) with N_{hb}=3 the required number of samples in the window is $N_{win} = 400$.

Averaging of the data is performed by moving the window only a fraction of the window size each time. This means that tracking is updated more often than the total number of windows in a sample set. However, the update procedure causes one reading to depend to some extend on former readings.

For extracion of the actual heart rate, two different methods could be applied; i.e. calculating the FFT spectrum and look for the highest spectral peak or calculate the cross-correlation (auto-correlation in this case) of the time signal and find the periodicity in the resulting signal. As the signals are not truly sinusoidal in nature, the latter analysis technique is applied. Furthermore, the auto-correlation has the property of enhancing any periodic signal while reducing the noise components, see [40]. Fig. 4.9 shows the auto-correlation signal of one window of the sample set from above. The heart rate is now calculated as one divided by the average time lag between at least three peaks in the auto-correlation.

Performing this window analysis for the entire dataset presented throughout this chapter, results in the heartbeat tracking curves shown in Fig. 4.10 for window widths of 4 and 8 seconds. The figure also includes the heartbeat track of the reference signal together with a deviation curve indicating how much the VISDAM measurement is off from the reference. To avoid sudden drop-outs due to inadequate tracking, a simple error-correction has been imple-

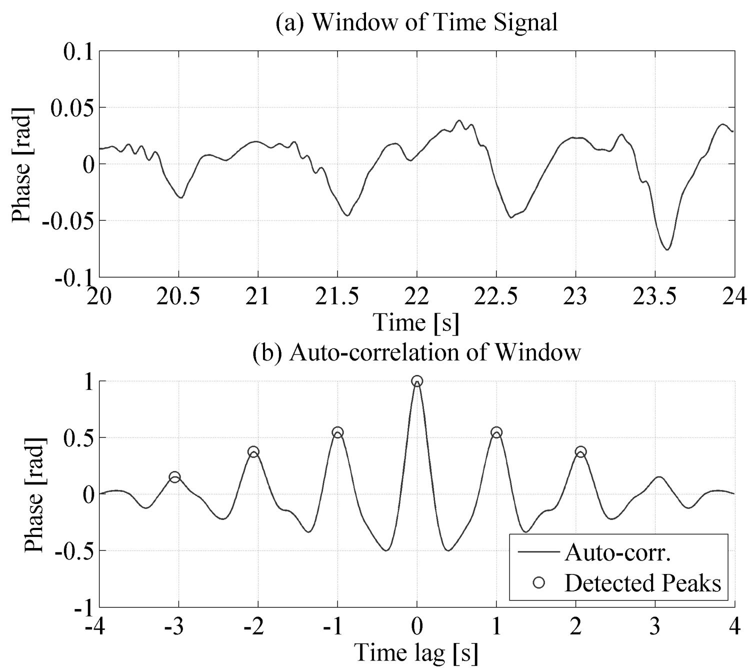

Figure 4.9: Extraction of heart rate showing (a) one 4 second window from the heartbeat signal and (b) the auto-correlation signal of that window together with the detected peaks.

mented such that the heart rate is forced to the range 40-180 bpm and such that jumps of more than 80% is not allowed between window moves. By showing the error-corrected points in the tracking curve to the user, he or she can assess the quality of the tracking and become aware that these points are not actual measurements.

Only 36 seconds out of the total 40 seconds sample set is shown. The reason for this is that the various filters used throughout the analysis, corrupt the data in the beginning where the filters are not properly started. These data points are therefore removed. From the example tracking curve of Fig. 4.10(a), it is seen that for a 4 second sliding window, the heart rate is tracked within 10% of the reference at all times and often it is better than 5%. As shown in Fig. 4.10(b), for an 8 second sliding window, the use of a longer windows improves the tracking accuracy, however, at the cost of a less real-time tracking.

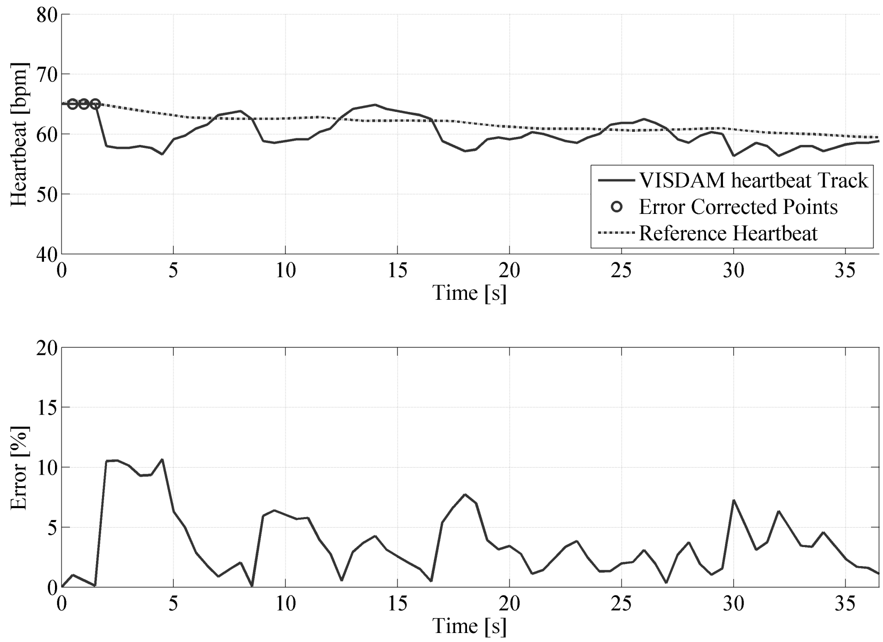

(a)

Figure 4.10: Heartbeat tracking curves obtained with (a) 4 seconds sliding window width and (b) 8 seconds sliding window width. Bottom plots show the deviation in percent of the reference. **Figure continuous on next page...**

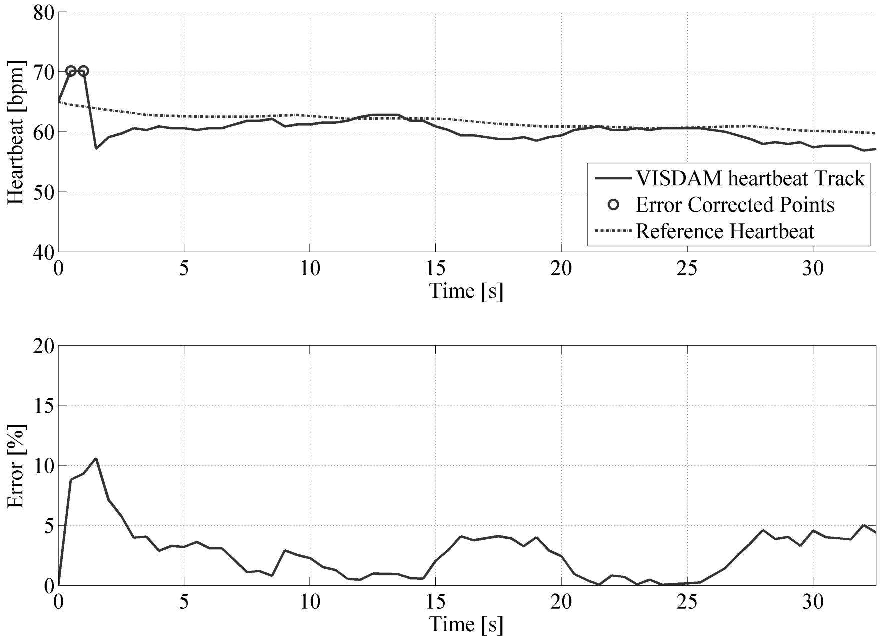

(b)

Figure 4.10: ... continued figure.

4.4 Correcting for Random Body Movements in a 2-unit Setup

As was stated in Section 2.4 the compensation of random body movements, require at least two measurements from either side of the person. Based on these, the phase vectors can be added to remove much of the random movement while enhancing the vital signs signals.

The software handles this issue by multiplying the I/Q data from the front-unit by that of the back-unit. This is done before the final low pass filtering of the phase data, such that most of the original high frequency signals from random movements are preserved in each signal, and thus cancelled the most. Results obtained with such a double-unit setup is presented in Chapter 5. For details on the cancellation, the reader is refered to the "runVISDAMdemod" function on the appended DVD, see Appendix 9.

Chapter 5

Small Scale Verification of the DTU-VISDAM Radar

To verify the operation and estimate the performance of VISDAM, a small scale verification test has been carried out, using the signal processing algorithms presented in Chapter 4 above. The main focus has been to test the capabilities of the hardware. The verification presented, is based on measurements from five different persons. Although a larger test group would have been of benefit to increase the accuracy, time did not allow for such an extensive verification.

5.1 Test Setups and Test Group

To test the hardware, three different scenarios were set up, see Fig. 5.1. In case I the person is seated between the two radar units facing the front radar. Case II presents the same radar placement, however, now with the person lying on his/hers back on a wooden couch. In this scenario the radars are facing each side of the person. Case III represents perhaps the most relevant case of them all for medical purposes, namely that the person is lying on a bed facing a radar placed in the ceiling. In cases I and II, measurements have been taken using either one radar unit or both radar units simultaneously. This has been done to test for random body movement cancellation. Furthermore, these double unit cases, were set up with a 50 MHz difference in carrier frequency (9.35 GHz and 9.40 GHz) and with one unit tilted 90^o to have orthogonal polarizations, see the figure. Both of these measures have been taken to lower the unit-to-unit cross-talk. Fig. 5.2 shows photos taken during measurements. Notice that due to limitations in the angular adjustment of the tripods, the orthogonal polarization is obtained by tilting each radar 45^o in opposite directions.

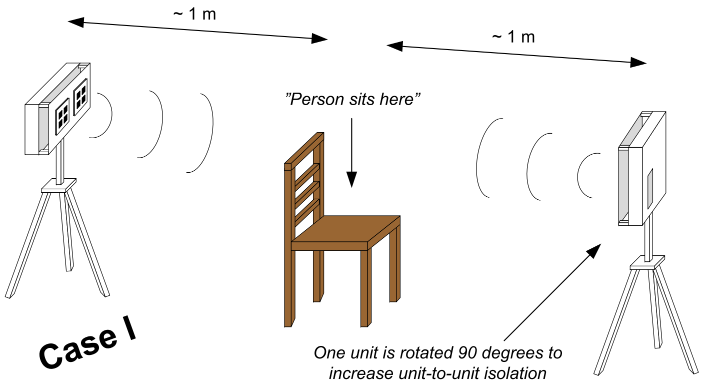

(a)

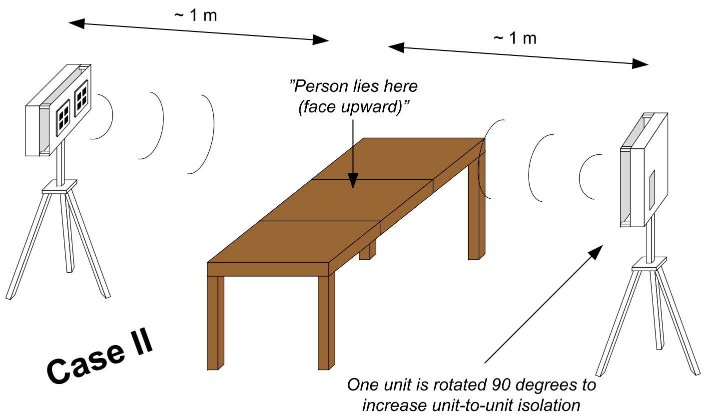

(b)

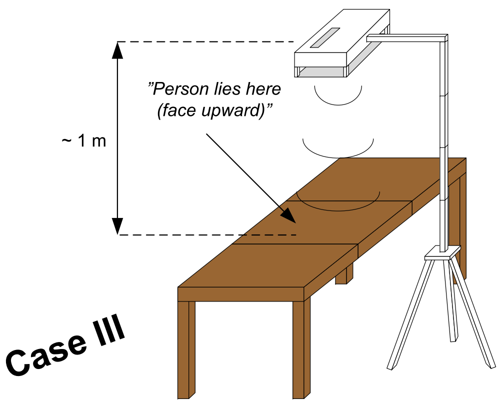

(c)

Figure 5.1: Measurement setups showing (a) Case I with single/double unit setup and a person sitting on a chair, (b) Case II with single/double unit setup and a person lying on a wooden couch facing upwards and (c) Case III; the same as Case II but with single unit setup, looking down on the person.

As mentioned above, the test group comprised five people. Ages were ranging from 28 to 66 years. Each person was measured in all three scenarios and three seperate measurements were taken for each person in each scenario. Furthermore, as cases I and II were taken as both single- and double-unit measurements, this roughly represent a total of 45 individual single-unit measurements and 30 individual double-unit measurements.

The persons were instructed to keep relatively still during each measurement, but was otherwise allowed to sit or lie as they pleased. Furthermore, they were allowed to wear their everyday cloth and jewelry, such that no assumptions/restrictions were made with respect to the person being measured.

Figure 5.2: Photos of the measurement setup while in use. Notice the $\pm 45^{\circ}$ alignment of the radars, to have orthogonal polarizations for minimum cross-talk.

For two of the persons, performance limitations were observed for the finger pressure reference sensor. Despite the use of a buffer, the low heartbeat strength in their fingers produced a very low voltage swing, which was rather noisy. The result has been a lowering of the accuracy of the reference for these measurements and thus for the verification. A better reference should therefore be designed for future verification and larger scale tests.

5.2 Measurement Results

Measurements have been collected in the exact same manner as presented in Chapter 4. To analyze the general performance, the heartbeat, measured with VISDAM was compared to that measured by the finger pressure reference. The difference curve has then been stored for each measurement such that an error distribution graph can be created based on multiple sample sets. This also allows for an evaluation of the mean error as well as the standard deviation.

Figure 5.3 shows error distribution graphs for each of the three measurement cases as well as one distribution graph for the entire collection of measurements, i.e. Fig. 5.3(f). Table 5.1 shows statistical data for all the graphs. It is clearly seen that the error distribution is not truly Gaussian (normal distributed) and especially, the mean error is not exactly zero. The main reason for this is primarily that the signal processing does not track the heartbeat in a sufficient manner. There are simply too many parameters that can be adjusted in the peak-detection algorithm of the auto-correlation procedure, such that the error distribution graphs can be manipulated. This indicates that the signal processing is not robust and indeed lacks a more adaptable detection algorithm to cope with different scenarios. At a point in time, all parameters were fixed to produce the results presented here. The VISDAM function

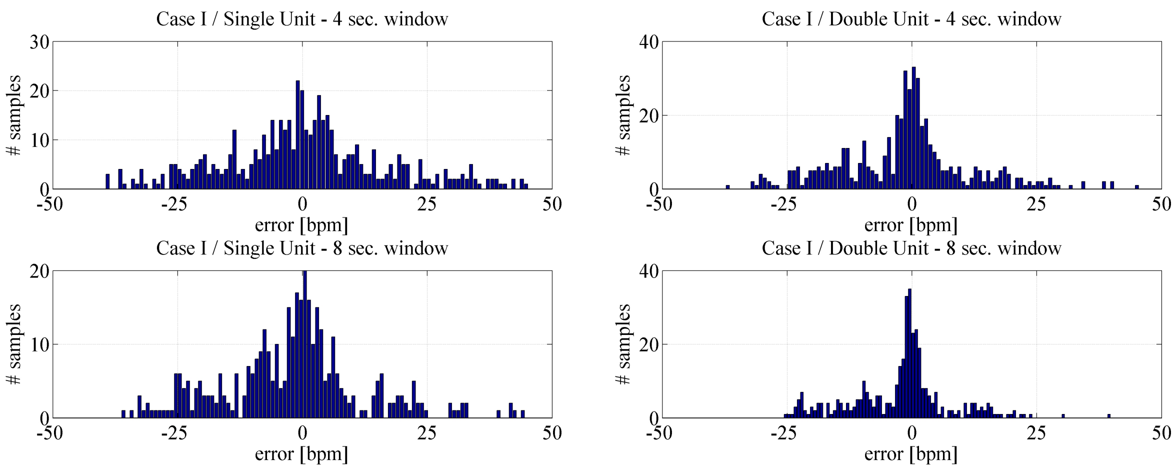

(a) (b)

Figure 5.3: Error distribution graphs: (a) Case I - single unit, (b) Case I - double unit, (c) Case II - single unit, (d) case II - double unit, (e) Case III - Single unit and (f) all measurements. Error distributions when using a 4 second window and an 8 second window is presented. **Figure continuous on next page...**

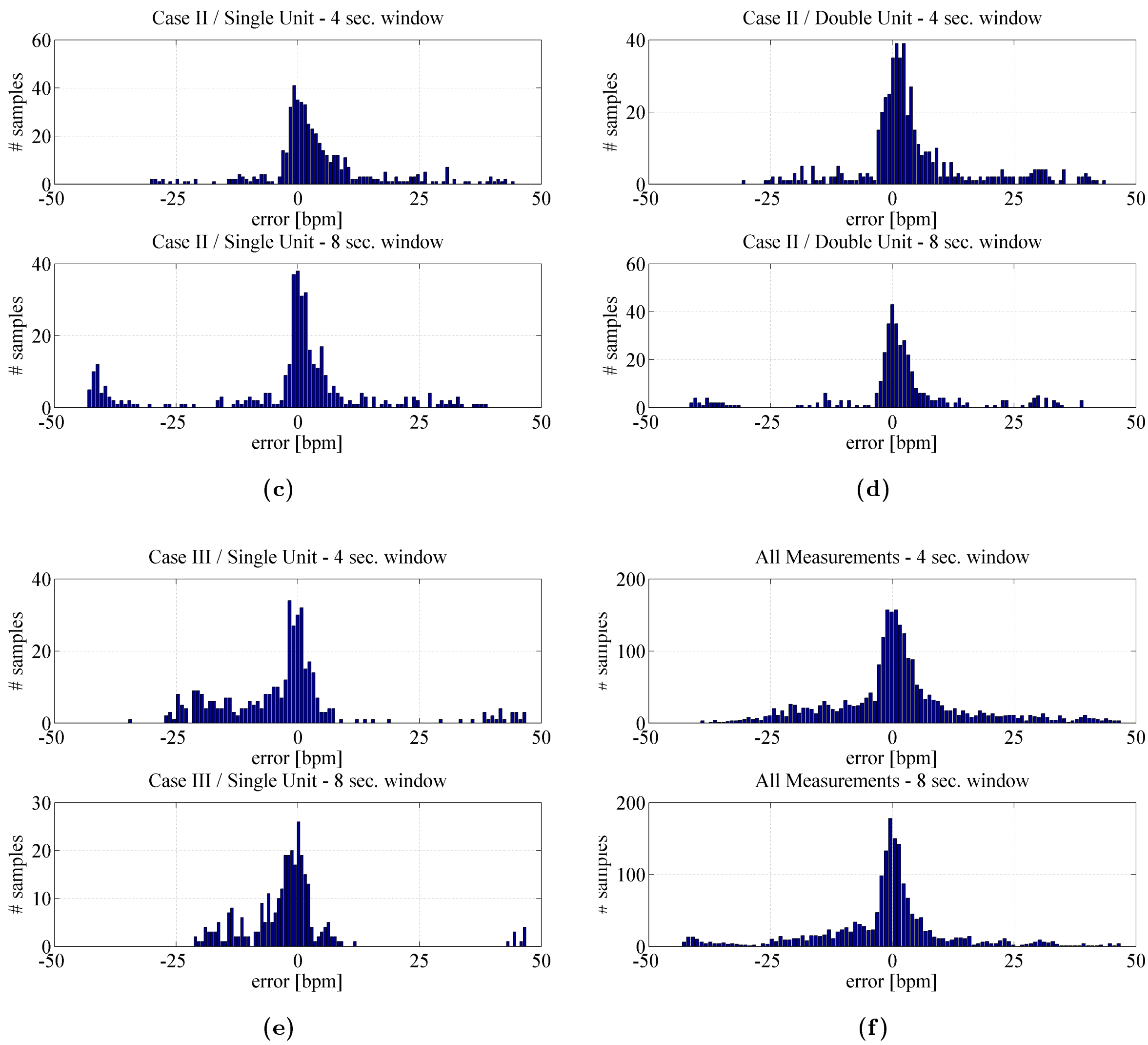

Figure 5.3: ... continued figure.

set files, located on the attached DVD (see Appendix 9) uses these fixed parameters.

Despite the limitations in the signal processing, the graphs and Table 5.1 show that VISDAM is in fact able to track the heartbeat of various persons in various scenarios. Also, when looking at single-unit measurements versus double-unit measurements, most measurements show a small improvement for the latter type; just as expected. The only exception is Case II with a 4 second window. This deviation could partly be explained by the rather small amount of available data and thus relatively high inaccuracy of the test. Measurements where the person is moving a lot, have not been carried out. However, it is expected that for such measurements, the effect of cancelling the random body movements would be even better.

For all cases, it is seen that the accuracy of the tracking becomes better when using a longer

	Setup	Win. Size [sec.]	Mean Error [bpm]	Std* [bpm]	corrected data [%]
All Cases	-	4	1.07	13.85	5.6
		8	-1.55	13.66	7.95
Case I	Single Unit	4	0.36	16.42	5.04
		8	-1.88	14.09	4.26
	Double Unit	4	-1.45	12.94	7.26
		8	-2.23	9.79	3.46
Case II	Single Unit	4	4.04	11.38	3.23
		8	-2.53	17.58	14.63
	Double Unit	4	4.36	12.17	4.64
		8	0.90	13.99	8.51
Case III	Single Unit	4	-2.69	14.50	8.31
		8	-2.12	10.51	8.97

*Std: standard deviation

Table 5.1: Statistical data for the small scale test performed with VISDAM.

window for detection. This could indicate that noise is to some extend limiting the accuracy (together with signal processing). To this end, it would be interesting to try to move the IF frequency to 10 or even 100 kHz to get outside the region in which 1/f noise is expected to dominate in the IF circuitry.

Until now emphasis has been on detecting the heart beat only. The reason for not including the respiration rate in the discussion is that no reference has been recorded for this parameter, and thus no direct comparison and statistical treatment of the error can be made. As was seen in Fig. 4.8 on page 49 the respiration signal is much stronger than the heartbeat signal. Ability to track the heartbeat signal therefore often also implies ability to track the respiration signal. Fig. 5.4 shows examples of extracted respiration signals from all three test cases, with the same person in front of the radar. As expected, it is seen that case II with the radar pointing towards the side of the person, presents a much weaker respiration signal than the other two cases. Furthermore, it is seen that the respiration response is somewhat more distorted in case I than in case III. This is also expected, as a person sitting in an upright position will create more random movements than a person lying still on the back.

It is evident from this small scale test, that VISDAM can track both heartbeat and respiration signals. A very convincing example was also shown throughout Chapter 4. However, it is strongly recommended that a skilled person within signal processing, take on much of the future work on VISDAM, before moving on to improve too much of the hardware. This way it might become clear which hardware parameters should be improved first. Also, many more tests should be carried out to reduce the uncertainty in the measurements and explore the capabilities for removing random body movements.

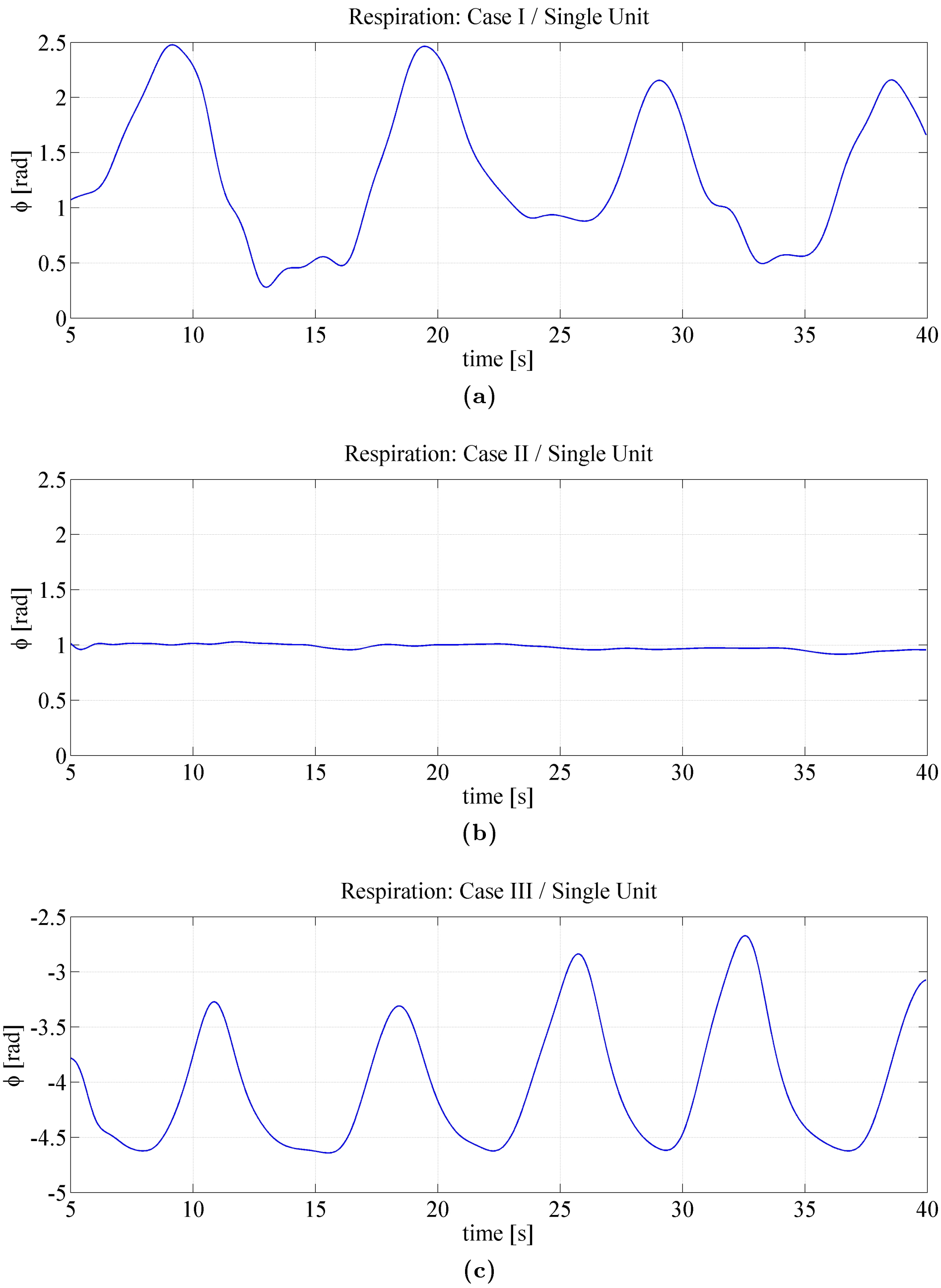

Figure 5.4: Examples of extracted respiration signals from (a) case I, (b) case II and (c) case III with the same person located in front of the radar. Single unit measurements are used.

Chapter 6

24 GHz VSD Radar IC in SiGe:C Technology

To explore a more compact solution, a full VSD radar front-end has been designed and manufactured as an integrated circuit (IC) in the 0.25 μm SG25H3 SiGe:C BiCMOS technology[1], [41], from the German company and research institute "Innovations for High Performance Microelectronics GmbH"; abbreviated IHP GmbH. This technology is cheaper but otherwise similar to the technology used in [JP1] and features five metal layers from which the two topmost layers are thicker for improved implementation of inductors and microwave structures etc. The high frequency npn heterojunction bipolar transistors (HBT) available in this technology features $F_t/F_{max} = 110/180$ GHz while having breakdown voltages of 2.3 V.

The radar IC has been designed for operation in the K-band, at a center frequency of approximately 24 GHz. Compared to the VISDAM radar at X-band and according to (2.14) this should eventually improve the overall sensitivity of the radar in which the chip is being implemented. Although higher frequencies could have been pursued, the selection of the K-band frequencies ensures that special licensing for using the radio band is unnecessary. Furthermore, a wide range of commercial products are available at these frequencies, which means that the radar chip can be combined with other IC's to improve the final performance.

This chapter first introduces the chip overview and then moves on to explain the sub-designs in more details. Simulations will be shown together with measurements of the manufactured IC at the end of the chapter. Simulations have been performed using Agilent ADS 2011 and the chip has been laid out using Cadence v.6.1.3.

Costs associated with the manufacturing of the VSD IC has been financed by the danish fund *H. C. Ørsteds Fonden.*

[1]SiGe:C stands for Silicium Germanium - Carbon Doped Base. BiCMOS refers to the technology as having Bipolar transistors and complementary MOSFET devices.

6.1 Chip Overview

Figure 6.1 shows the schematic overview of the 24 GHz VSD IC. It consists of a transmitter chain (Tx) and a Receiver chain (Rx) both of which utilize I/Q mixer topologies for SSB operation. Although the Rx chain could suffice with a DSB mixer, the mixer design chosen (see below) is capable of both up- and down-conversion and is therefore reused for ease of system implementation. The LO signal is split in $\pm 45^o$ branches through a second-order poly-phase filter network and buffers help maintain LO signal strength all the way to the mixers. An LO input buffer has been implemented to lower the requirement for the LO input power. In order to ease the testing of the IC, the LO generator is not implemented on-chip. The IF input (I and Q) are feed from an external source to provide a means for optimizing IRM performance through external adjustment of phase- and amplitude balance. At the Tx side output, an external balun is needed to transform the differential output signal into a single-ended signal for the Tx antenna. Unfortunately, such a balun was not available during measurements of the IC, see Section 6.4. Nonetheless, the IC was still tested and raw measurements as well as corrected measurements taking into account the theoretical loss of power (3 dB) are presented.

The Rx chain consists of two cascaded LNA's designed to provide approximately 27 dB of gain before entering the down-conversion mixer. The mixer conversion loss has been designed to be approximately 14 dB, indicating an expected total receiver gain of approximately 13 dB. Although only one IF output is needed, both branches of the I/Q mixer is taken out of the chip. When retrieving only one IF output, the expected receiver gain thus drops to approximately 10 dB (i.e. 3 dB lower).

As indicated in the schematic, the entire chip has been implemented using differential

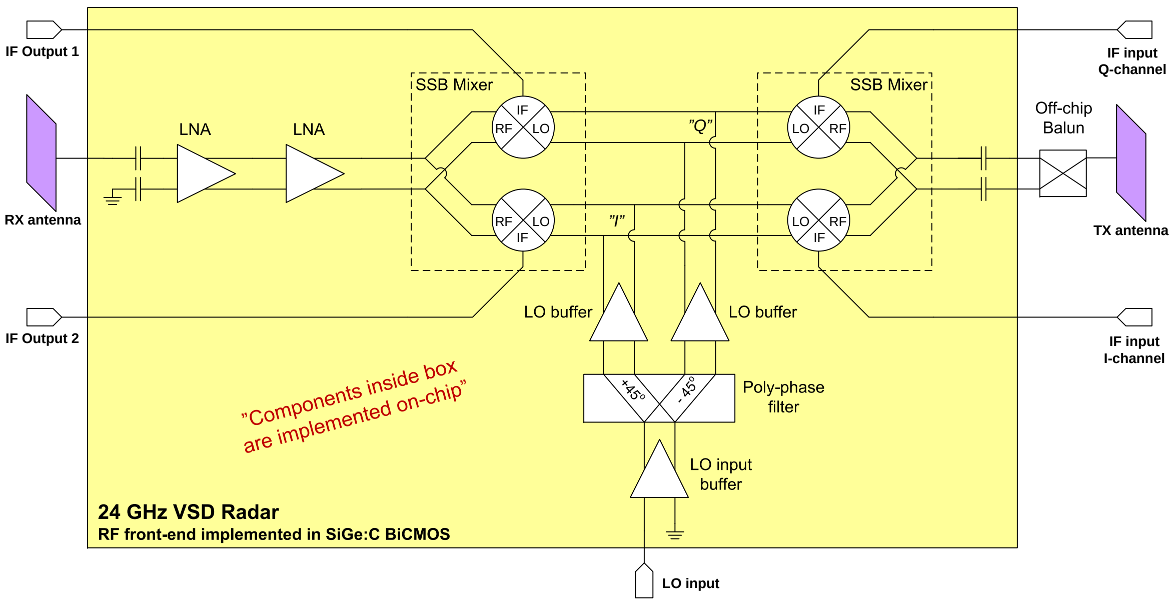

Figure 6.1: Schematic of the VSD radar front-end implemented in SiGe:C BiCMOS.

designs. This ensures that common-mode noise rejection and DC offsets are lowered considerably; two factors which can be rather high when implementing circuits on lossy substrates such as SiGe. The only exception is the IF input and output branches, which are implemented single-ended. However, as shown below, the mixer cores are still operating in a differential fashion.

6.2 Transformer Loaded Low Noise Amplifier Design

Figure 6.2 shows a circuit diagram of the two cascaded LNA's. The core of each amplifier is based on a cascode bipolar differential pair. The input signal is provided single-ended through the coupling capacitors C_C while C_{M1} and L_M provide input matching. Biasing of the bipolar pairs Q1/Q2 and Q5/Q6 is provided externally through bias resistors R_B and the emitter inductors, L_E, which are rather small are provided for a trade-off between gain and bandwidth performance. The cascode transistors Q3/Q4 and Q7/Q8 are biased directly to VCC through a resistor. The bias current for each stage is provided through a bipolar current mirror which is degenerated through R_{DEG}.

Each amplifier is loaded by a transformer with a center tap in one coil for DC biasing. As presented in [42, 43], the use of transformers have several advantages, as compared to a more traditional topology using inductors for loading of a single amplifier. First of all it provides a direct AC coupling between the output and the input of the next stage. Furthermore, as the base input of the HBT (or gate of a MOS) is inherently capacitive, the secondary coil of the transformer acts as a direct matching component between the output and the input

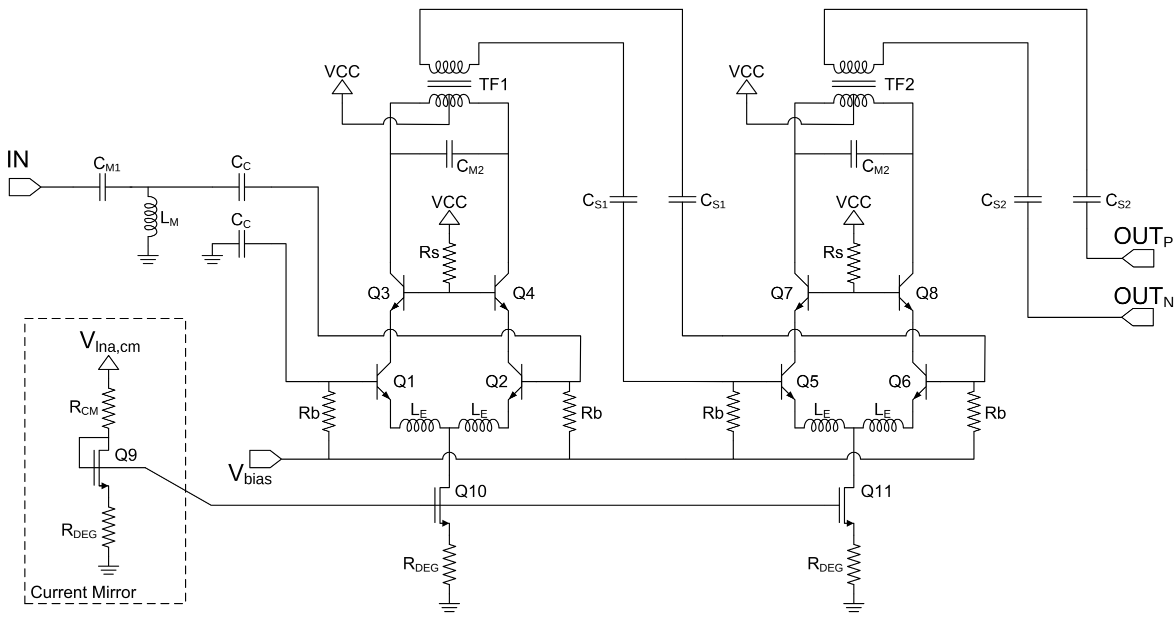

Figure 6.2: Schematic of the transformer loaded LNA.

of the next stage. Topologies not exploiting transformers would normally need additional series matching inductors and thus would typically occupy a larger chip area. Furthermore, when lowering the number and sizes of matching components, bandwidth can normally be increased and the loss decreased. For precise tuning of the load transformer, the capacitors C_{M2} and C_{S1}/C_{S2} are provided. The latter series capacitors are not identical for both stages. The reason for this is that the output of the cascade is matched to 50 Ω while the interstage matching is tuned for a higher bandwidth.

Transformers and inductors are used in all sub-circuits of the VSD IC design. As the simulation and estimation of their performance parameters has been one of the most challenging tasks throughout the implementation, the following discussion will explain the general parameter extraction method used for these components.

A 3D rendering of the LNA loading transformer is shown in Fig. 6.3. The series resistance of each coil and thus the transformer loss is decreased (higher quality factor, Q) by using both of the two top-most thick-metal layers for the windings. Although the use of multiple metal layers decrease the series resistance, it also increase the capacitive coupling to both the lossy sustrate and the ground ring occupying the periphery of the transformer design. This then again decrease Q and the self-resonance-frequency (SRF). Inductors and transformers should be operated below their peak Q value (SRF point) to ensure proper functionality. Simulations using the SG25H3 technology layer stack, showed that the use of the lower three metals (thin metals) would only decrease Q (and SRF), and thus windings for the final design was not created in these layers.

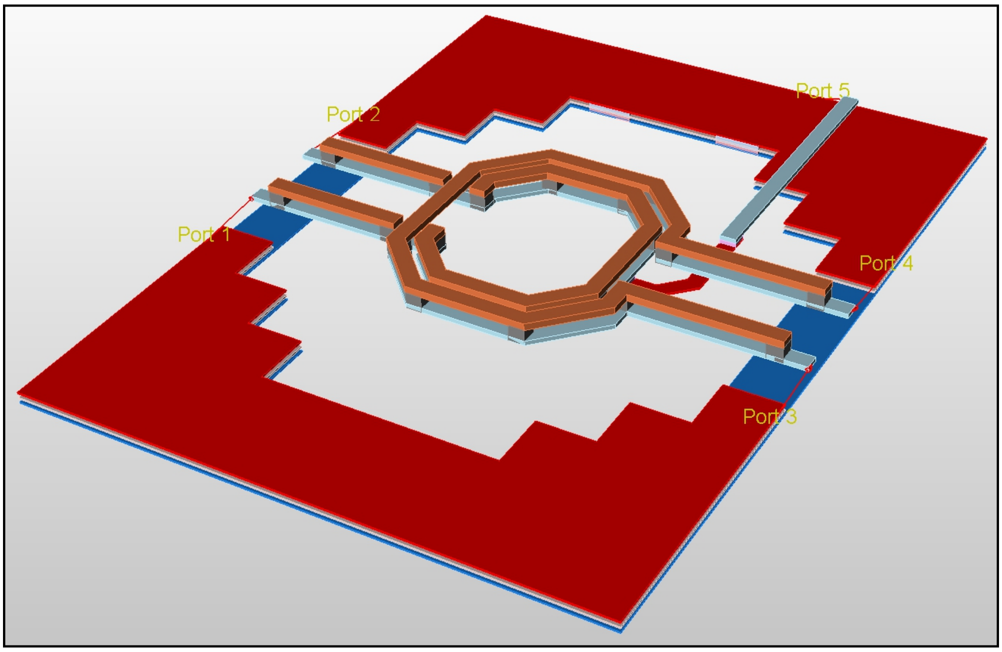

Figure 6.3: 3D rendering of the LNA loading transformer with center tap on one coil for DC biasing.

The ground ring is important for two things. Firstly, from a circuit performance point-of-view it isolates the transformer from the rest of the circuit and thus lowers the cross-talk between circuit blocks. Secondly, and far more importantly, it helps to control the surroundings and especially also the return-current during simulations, [44]. To increase Q, the capacitive coupling has been lowered by implementing the ground ring in the three lower metal layers only. As shown in Fig. 6.3, internal ports placed between the ground ring and the transformer is used for proper handling of the return-current. Placing the ports between the back ground plane (beneath the substrate) and the transformer would force the current to run through the substrate, and this does not resemble the physical situation.

To lower substrate effects such as induced eddy currents forming unwanted loop currents, [45], patterned ground shields are often employed, [46,47]. However, as the frequency goes up, the parallel capacitance to ground increases, thus lowering Q. Some initial simulations of the transformers developed for the VSD IC investigated the use of patterned ground shields. It was found, that the capacitive coupling eliminated the benefit of the ground shield and in fact lowered the overall Q of the transformers. The final transformer design therefore does not employ a ground shield.

Throughout the optimization of the circuit, the extraction of inductor/transformer parameters (inductance, series resistance, parallel capacitance etc.) was based primarily on the simple inductor pi-model, [48], shown in Fig. 6.4. Although this model does not split *all* parasitics into physically meaningfull parameters, it is adequate as an optimization technique. For a more physical model, the parameters should be extracted using the method presented in [49]. For the final verification of the circuit behaviour, the EM simulation was used directly in a schematic co-simulation, thus taking into account all simulated parasitics.

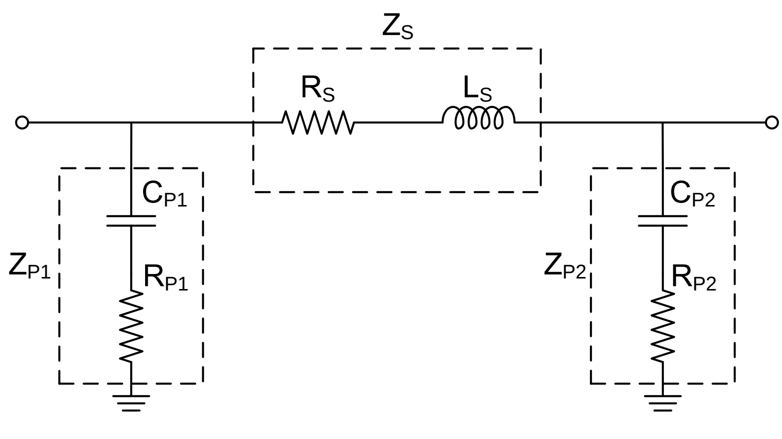

Figure 6.4: Simple pi-model of an inductor. The series impedance is split into an inductive and a resistive part while the parallel impedance is split into a capacitive and a resistive part.

Using 2-port Y-parameter arithmetic the model parameters from Fig. 6.4 has been extracted using

$$L_S = \frac{-\Im\Big\{Y_{12}^{-1}\Big\}}{\omega} \qquad R_S = \Re\Big\{-Y_{12}^{-1}\Big\} \tag{6.1a}$$

$$C_{P1} = \frac{1}{\omega \cdot \Im\big\{Y_{11} + Y_{12}\big\}} \qquad R_{P1} = \Re\Big\{\big(Y_{11} + Y_{12}\big)^{-1}\Big\} \tag{6.1b}$$

$$C_{P2} = \frac{1}{\omega \cdot \Im\big\{Y_{22} + Y_{21}\big\}} \qquad R_{P2} = \Re\Big\{\big(Y_{22} + Y_{21}\big)^{-1}\Big\} \tag{6.1c}$$

where $\Re\{\cdot\}$ is the real part, $\Im\{\cdot\}$ is the imaginary part and where $\omega = 2\pi f$ is the angular frequency. Furthermore, the effective quality factor can be found as

$$Q_e = \frac{-\Im\big\{Y_{11}\big\}}{\Re\big\{Y_{11}\big\}} \tag{6.2}$$

The transformer parameters such as mutual coupling, M, and coupling factor, k, for the LNA loading transformer shown in Fig. 6.3 has been extracted based on three seperate simulations, i.e. two simulations for each coil seperately and one simulation for the actual transformer. Extracting the inductance for each coil without the influence of the other, gives the ideal mutual coupling as

$$M_{\text{ideal}} = \sqrt{L_{S,pri} \cdot L_{S,sec}} \tag{6.3}$$

where $L_{S,pri}$ and $L_{S,sec}$ is the inductance values for the primary and secondary coils, respectively. The simulation of the actual transformer then gives the performance of each coil under influence of the other, such that the actual mutual coupling and coupling factor can be found as

$$M_{\text{actual}} = \sqrt{L_{S,priT} \cdot L_{S,secT}} \qquad k = \frac{M_{\text{actual}}}{M_{\text{ideal}}} \tag{6.4}$$

where $L_{S,priT}$ and $L_{S,secT}$ is the inductance values for the primary and secondary coils when simulated in the transformer. Fig. 6.5 shows the simulated parameters for the transformer used in the LNA. The quality factor is rather high indicating low loss. The curve becomes flat at approximately 29 GHz, beyond which the inductor should not be used. A coupling factor of 0.81 at 24 GHz is a rather strong coupling and ensures low insertion loss.

Another parameter that has been used for optimization of the transformers is the so-called Transformer Characteristic Impedance (TCR), given by, [42].

$$TCR = \omega \cdot \left(\frac{k^2 \cdot Q_P^2 \cdot Q_S}{1 + k^2 \cdot Q_P \cdot Q_S}\right) \cdot \left(L_{S,pri} + \frac{L_{S,pri}}{Q_P^2} + \frac{k^2 \cdot L_{S,pri} \cdot Q_S}{Q_P}\right) \tag{6.5}$$

where Q_P and Q_S are the quality factors for the primary and secondary coils, respectively.

It has been shown in [42] that for transformer loaded circuits, the available output power is proportional to the TCR value and thus the gain of each LNA. Fig. 6.6 shows the simulated TCR for the LNA transformer. The TCR is seen to be higher than 800 Ω at the design frequency of 24 GHz. For comparison, the optimized designs in [43] provided a slightly higher TCR of approximately 900 Ω.

Recently, IHP GmbH has introduced back-side etching of their substrates after IC production, which help increase Q of inductors and transformers, [50]. In future SiGe IC designs,

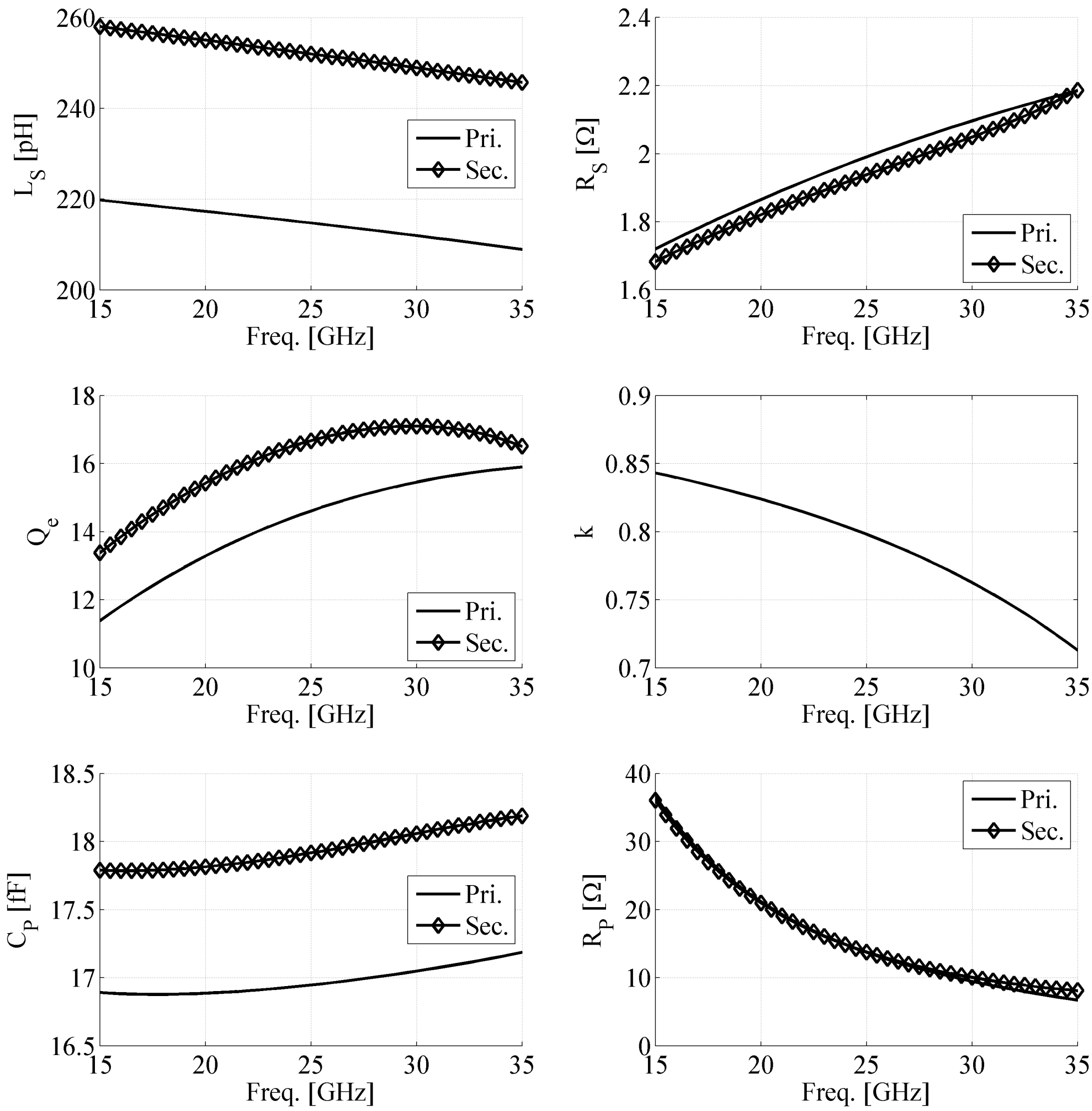

Figure 6.5: Performance of the LNA loading transformer.

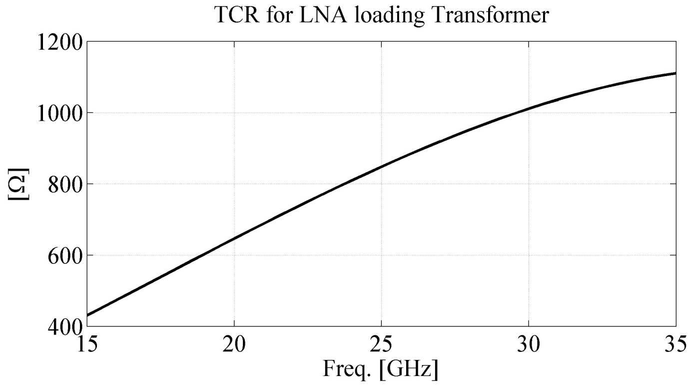

Figure 6.6: TCR of the LNA loading transformer.

this should be exploited for a better overall performance.

6.3 Single-Sideband Mixer Design

Figure 6.7 shows the core of the I/Q mixer, consisting of two identical double-balanced FET resistive ring mixers. Double-balancing is important for isolation between the different inputs and outputs of the mixer, and ensures that leakage should be kept at a minimum. The passive FET mixer is incapable of conversion gain and the reverse-isolation is practically non-existing. On the other hand this ensures that it can be used for both the up- and down-conversion processes, which made the design process for the VSD IC much simpler.

Using a passive FET resistive topology also reduces the 1/f noise compared to topologies with a DC biasing current and lowers unwanted intermodulation products for high RF drive levels, [51, 52]. As was discussed in [CP2] this is important, because the range-correlation effect, most often makes the 1/f noise components in the receiver (LNA and down-conversion mixer) more critical than the phase noise component inherent in the LO generator. Furthermore, using a non-biased topology for low-frequency IF operation, ensures that the DC component is kept at a minimum.

As shown in the figure, the RF signal is split between each mixer. A combined matching is provided through the differentially operated inductor $L_{M,RF}$ and the series capacitors $C_{M,RF}$. Each of the LO input ports (I and Q) are fed through a similar matching network and combined with a DC bias voltage through a set of large resistors, R_B. This biasing lowers the requirement for the LO signal swing amplitude, without sacrificing switching capability in the MOS devices, i.e. the required LO power can be lowered. The DC current, caused by the biasing will be kept low through a set of large DC pull-down resistors, R_{PD}, whos purpose is to ensure a close-to-zero DC voltage on all drains and sources of the devices. The IF signal for each mixer is taken single-ended. The IF branch not being used has been connected to ground, as shown.

The quadrature LO inputs are generated by a second-order poly-phase filter circuit, [53], shown in Fig. 6.8. The externally provided single-ended LO signal is coupled into the cir-

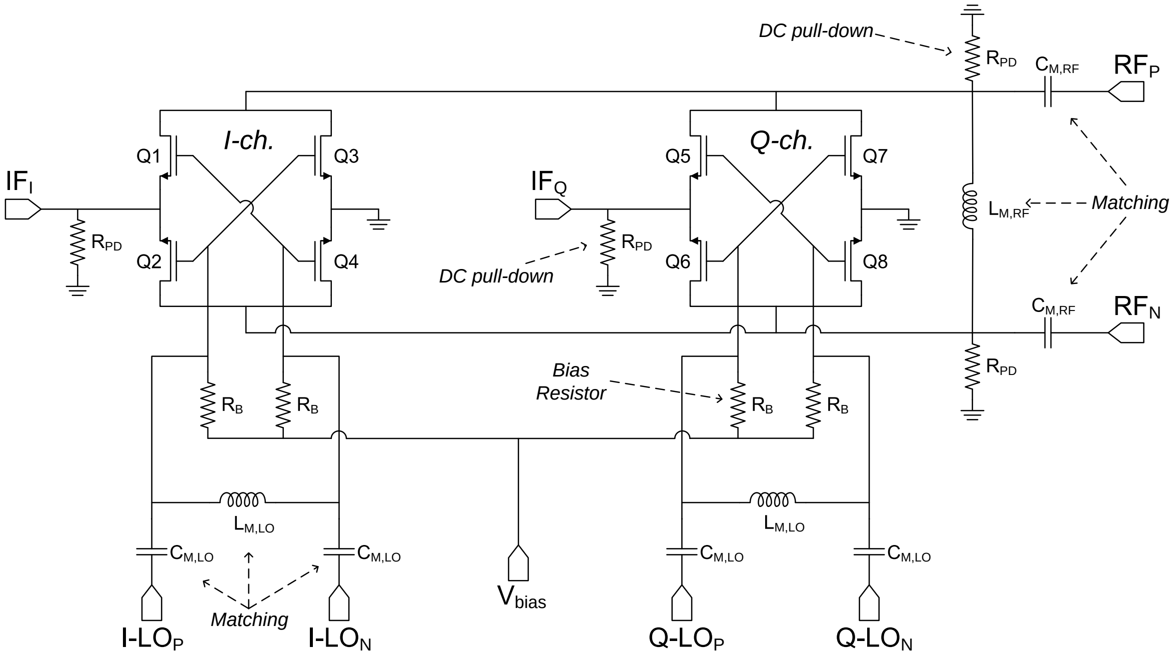

Figure 6.7: Schematic of the I/Q Mixer Core.

cuit through the transformer, TF1, which makes the LO signal differential. The single-ended matching of the LO input is provided through C_{M1} and C_{M2} and is necessary in order to be able to connect the transformer to ground. C_{IN} provides matching between the transformer and the input buffer consisting of two parallel emitter followers, Q1 and Q2. The capacitors C_C acts as DC blocks such that the emitter followers can be biased through the R_B resistors.

As the poly-phase filter is inherently lossy, LO drivers are needed to provide the two mixers with an adequate LO signal swing. These LO drivers are implemented as bipolar differential stages (Q6 and Q7) using double the amount of tail current as the input buffers. The bases of the differential pair are biased directly through the emitter DC voltage of the emitter followers and thus do not need an additional bias voltage. Current sources for the entire LO input chain is provided through a bipolar current mirror setup using the same reference (Q5). Degeneration resistors, R_{DEG}, are used for higher output resistance in the current sources. Both the buffer bias voltage, $V_{buf,bias}$, and the current mirror reference supply, $V_{buf,cm}$, is externally feed to the circuit in order to be able to adjust the biasing when testing the IC.

6.4 Experimental Results

Figure 6.9 shows a photo of the manufactured VSD IC with the different circuit blocks marked by rectangles and labels. The IC measures 2690x1390 μm. Measurements on individiul circuit blocks are not possible, so the IC has been tested as a complete radar front-end. First the transmit branch has been tested using an Anritsu MG3694A 40 GHz signal generator for the

LO input and a TTi TG120 20 MHz function generator for the IF input. The RF output power has then been measured on an HP 8563E spectrum analyzer taking into account all losses related to cables and interconnects. The spectrum analyzer can measure signals in the range from 9 kHz to 26.5 GHz. Therefore, throughout the testing of the IC, the IF frequency was set to 12 kHz, such that the spectrum analyzer could be used for both transmit and receive test. IRM performance has briefly been tested at 1 kHz IF using the splitter circuit from VISDAM, and an IRM better than 40 dB was observed. However, for the measurements shown below, DSB transmission has been used due to two issues. Firstly, the VISDAM splitter only operates up to approximately 3 kHz and secondly when sweeping the LO frequency, the circuit would have to be adjusted every time a measurement is taken. The theoretical SSB performance is then estimated by adding 3 dB to the measurements of the output power. DSB measurements only affect the receiver testing, as will be explained below. The power consumption of the entire IC is approximately 164 mW. The total current is approximately 57 mA at several different bias voltages between 1.6 V and 3.0 V.

Figure 6.10 shows the measured output power from the transmitter using a 0.26 mV_{pp} IF signal and 0 dBm LO power at the IC interface. Unfortunately, a K-band balun was not available for the measurements, so only one end of the differential transmitter output was

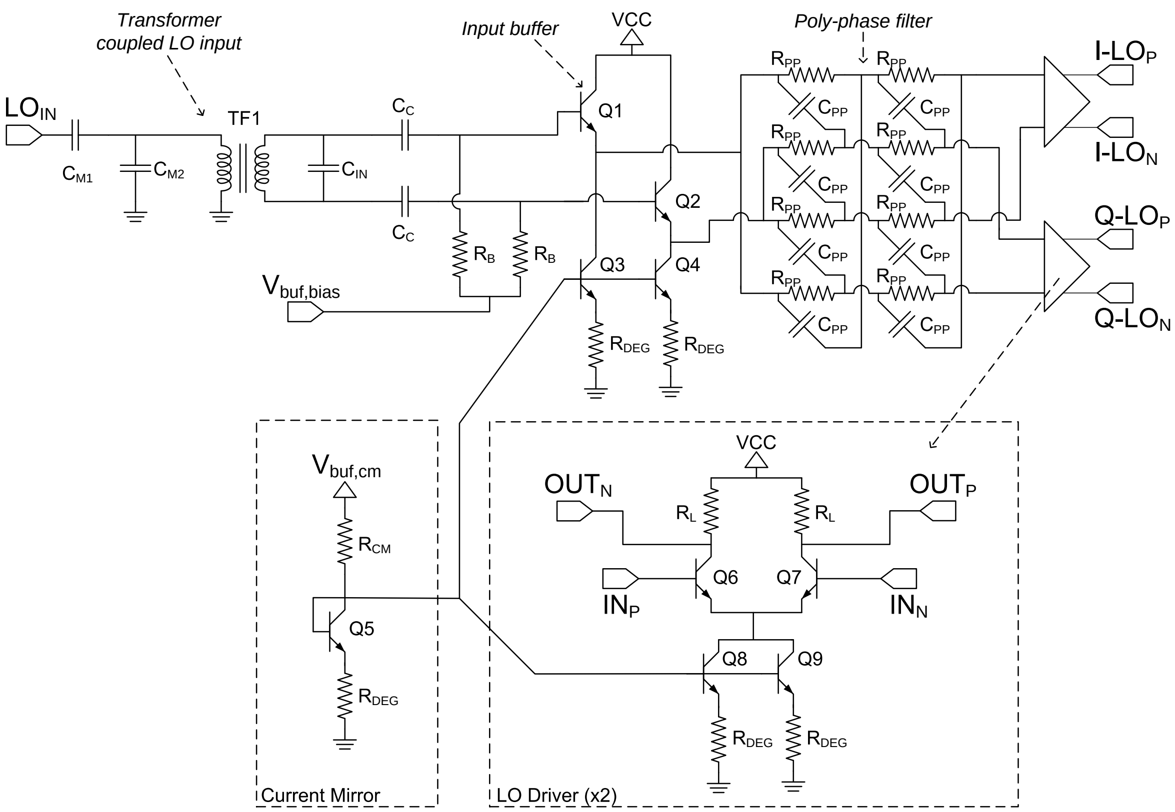

Figure 6.8: Schematic of the LO input buffer, poly-phase filter for 90 degree split and LO driver for the mixer inputs.

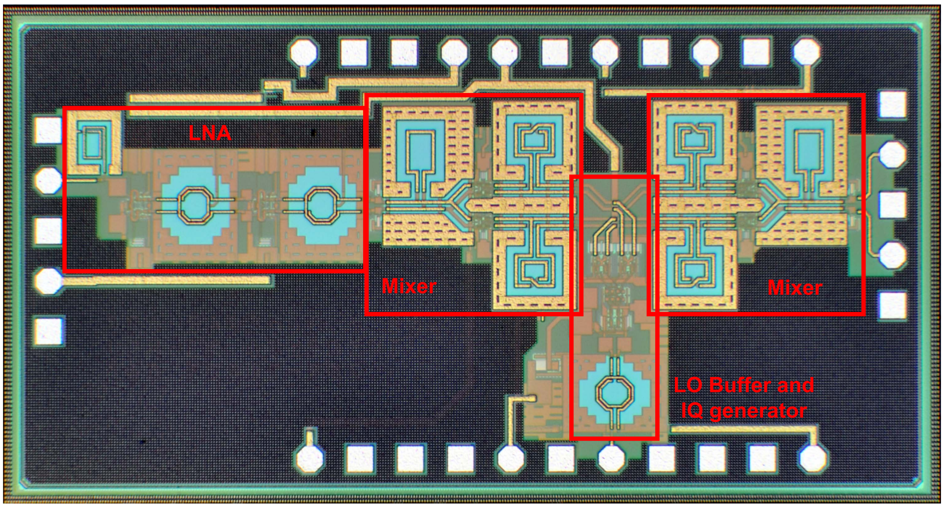

Figure 6.9: Chip photo of the VSD IC fabricated in the IHP SG25H3 SiGe:C HBT technology.

measured, while the other end was terminated into 50 Ω. The measurement shown in Fig. 6.10 shows the theoretical differential power which is 3 dB higher than the original measurement of the total DSB signal power, i.e. the power that would be transmitted in a given SSB signal if IRM was employed. As seen, the transmitter has a center frequency of approximately 24 GHz as intended. However, the output power is approximately 5 dB lower than simulations. The reason for this could be an underestimation of the losses in the critical matching inductors of the mixer and a lowering of the LO drive level provided by the LO buffer network. Bias points for the buffer network were swept to see the general characteristics. Optimum points were located very close to the simulated values.

Figure 6.11 shows a sweep of the LO input power at 23 GHz with all bias points kept constant at their nominal (close to optimum) values. As seen, the buffer network starts to saturate at around 3 dBm LO input power, beyond which the transmitter output power is

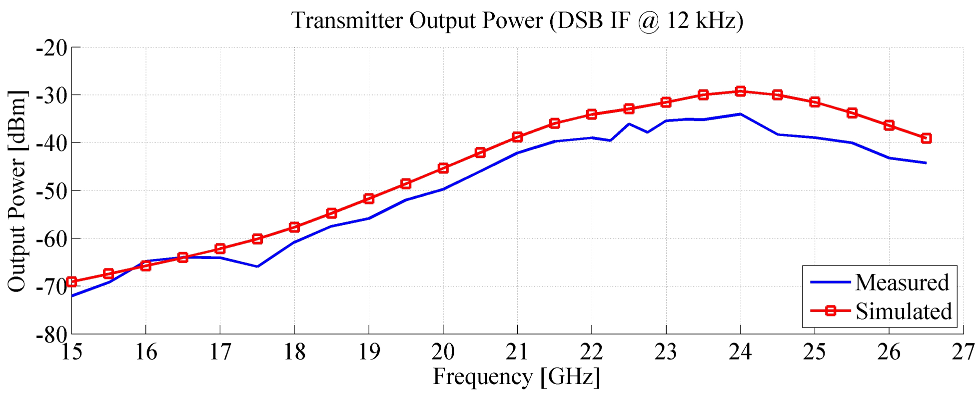

Figure 6.10: DSB output power as function of LO frequency at an IF drive level of 0.26 mV_{pp} at 12 kHz. LO input power was set to 0 dBm at the IC interface.

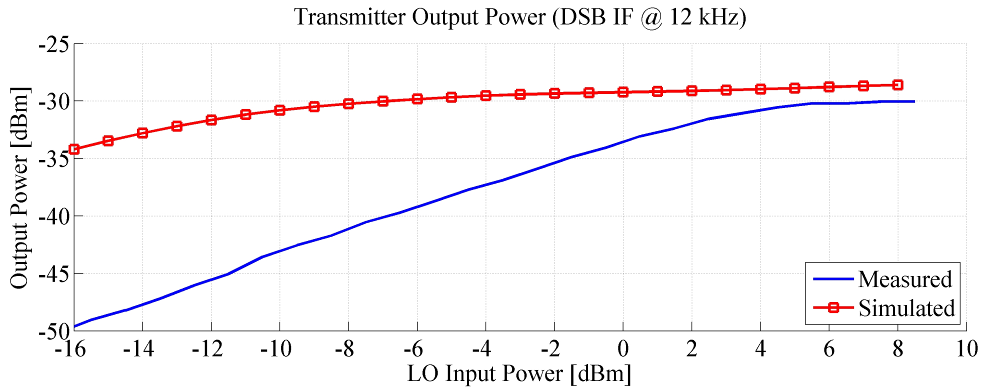

Figure 6.11: DSB output power as function of LO input power at 23 GHz with all other parameters kept constant. IF is again 12 kHz with a drive level of 0.26 mV_{pp}.

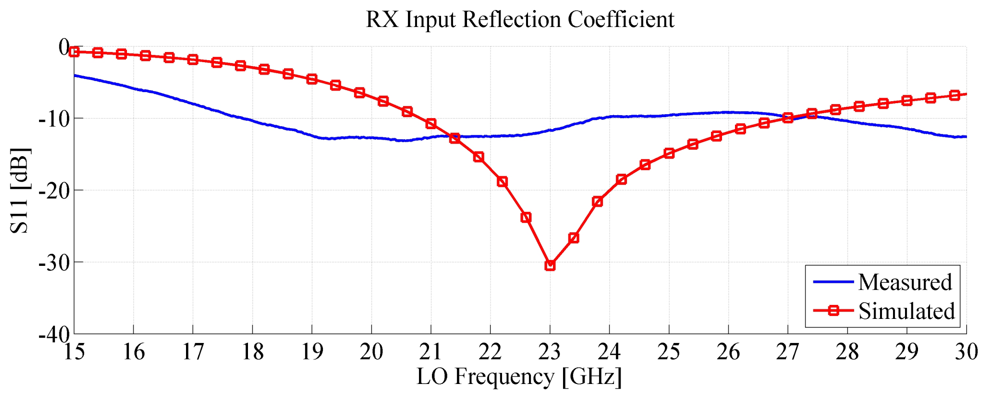

Figure 6.12: Reflection measurement at the receiver input, obtained with an Anritsu ME7808B VNA.

only increased slightly. At the maximum drive level (10 dBm) provided by the Anritsu RF generator, the output power is approximately -30 dBm.

The return loss of the receiver has been measured on an Anritsu ME7808B VNA, see Fig. 6.12. Although comparison to simulation reveals a small down-shift in frequency and a poorer match, the return loss is better than 10 dB for the band between 18 and 24 GHz. This is satisfactory.

The down-conversion operation of the receiver has been measured in a loop back test, where the output of the transmitter has been connected to the input of the receiver. Again, the bias points of the LNA block was swept and optimum points were located very close to the simulated response. As DSB signals of almost equal wavelength are transmitted, the envelope of the down-converted signal will be modulated in much the same way as in (2.22a) for the transmission of DSB signals in the low-IF VSD radar architecture, i.e.

$$S_{DSB}(t) = \cos\left(\frac{2\pi}{\lambda_{RF}} d_0\right) \cdot \cos\left(\omega_{IF} t\right) \tag{6.6a}$$

$$= \cos\left(\frac{2\pi f_{RF}\sqrt{\epsilon_r}}{c} d_0\right) \cdot \cos\left(\omega_{IF} t\right) \tag{6.6b}$$

where f_{RF} is the carrier frequency, ϵ_r is the relative permitivity of the cable used for loop-back, d_0 is the length of the cable and where a factor of 2 is removed in the phase because the wave only travels one way. As seen, the sweeping of the frequency will modulate the envelope of the measured IF receiver signal. It is therefore important that the sweep step is sufficiently small such that the maximum values of this modulation can be caught.

Figure 6.13(a) shows the measurement of the receiver gain when the variations of the transmit power has been compensated for. The envelope modulation as a function of the LO frequency is clearly seen from the measurement data. Identifying all the peaks and connecting those points in a single graph as shown in Figure 6.13(b) gives the gain curve that would

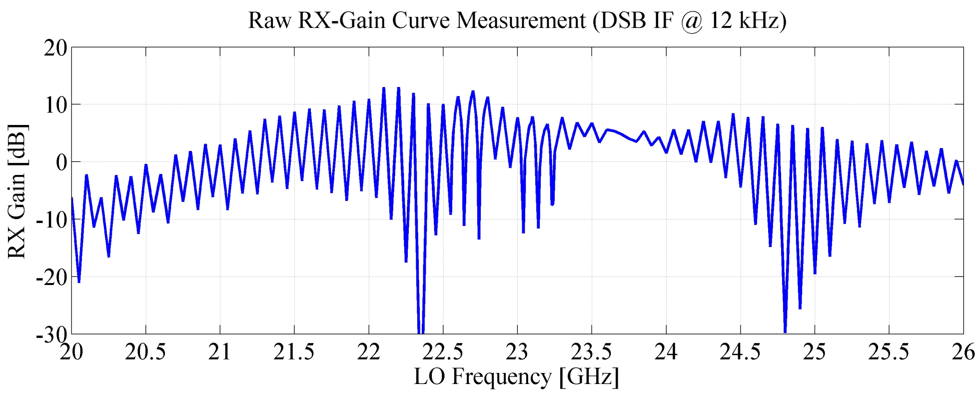

(a)

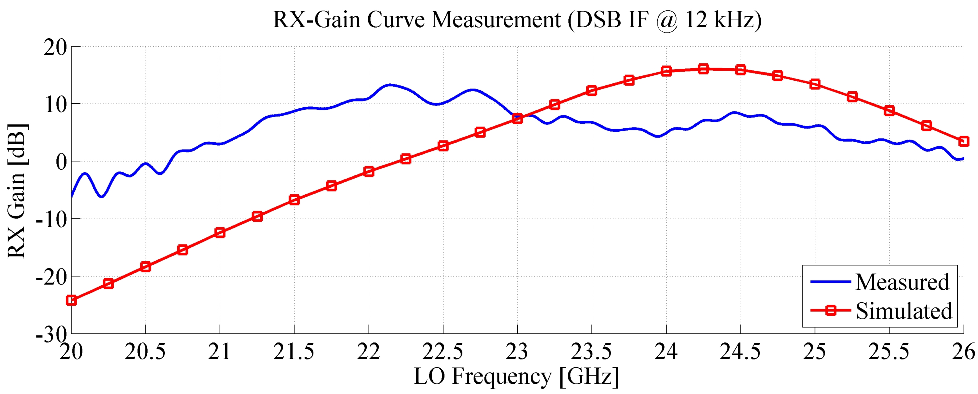

(b)

Figure 6.13: Receiver gain measurement performed with a loop-back test of the IC transmit signal. (a) shows the actual measurement using DSB transmit signal and (b) shows the predicted gain curve in the case of an SSB signal.

be observed if SSB signals had been used, i.e. when the envelope would not have been modulated. Besides having some rather large ripples, it is seen that the receiver is shifted slightly down in frequency, with a peak gain of 13.3 dB at around 22.15 GHz. Thus the mixer and the LNA circuits are not fully aligned with respect to carrier frequency. It is reasonable to think that if a future design manages to align the two circuit blocks, then the overall gain curve will become closer to the simulated result. Nontheless, the receiver produces gain through the down-conversion process and it can be concluded that the IC seems usable in a VSD system. Most likely, a small power amplifier should be added to the transmit branch to boost the signal before the transmit antenna.

Chapter 7

Conclusion

In this thesis a technology study of CW radars for detection and monitoring of human vital signs has been performed. These radars are able to detect both respiration and heartbeat signals. Emphasis has primarily been on the latter parameter, which is also the most difficult to extract. The study includes a theoretical treatment of different CW radar architectures, including the single-channel and quadrature homodyne (direct conversion) architectures as well as the single-channel low-IF heterodyne architecture. The latter has traditionally been avoided due to phase noise concerns related to the small offset frequencies presented by the human vital signs, i.e. below 3.5 Hz. However, it is shown that not only can the heterodyne architecture overcome phase noise problems; it can do so with a reduced number of receiver channels and thus fewer number of error sources such as channel mismatches etc. The key design parameter for this to be true, is to ensure signal coherency in the radar.

The homodyne architectures have traditionally been limited by the so-called null-detection points related to the nominal target range and caused by a destructive combination of signals in the down-converter. The theoretical treatment in this thesis shows that these null-detection points also occurs in heterodyne architectures using DSB transmission or down-conversion. For the architecture to overcome null-detection points, it is essential to employ SSB signals instead.

To investigate the heterodyne architecture with low IF in practice, the DTU-VISDAM X-band system has been developed. This system consists of two identical radar units employing a single-channel heterodyne architecture with an IF frequency of 1 kHz. Interfacing is done through LabView and signal processing is performed in Matlab. Ability to track the heart rate has been demonstrated through a running example presented while discussing the implemented signal processing algorithm and a small-scale verification performed on 5 persons. From these investigations it is evident that the present state of the signal processing lacks a better adaptation scheme for different signal conditions. One of the major future tasks with the VISDAM system, is therefore to implement even more automated and more sophisticated algorithms for real-time processing with dynamic error-correction for a robust detection. Furthermore, it would be of interest to investigate the use of a 10 kHz or even 100 kHz IF frequency to move further away from the 1/f noise region in the IF circuitry.

Future work should include a more comprehensive test of VISDAM. Especially, the effect of cancelling random body movements with a double-unit setup should be investigated more thoroughly; but also, it would be of benefit to investigate the effect of using different aiming angles and polarization orientaions. To increase the overall detectability it is likely that the use of multiple frequencies, either in the form of FSK or swept frequency measurements, could be of benefit. An investigation on these methods should therefore be conducted.

To investigate the possibilities for reducing instrument size while at the same time lowering overall power consumption, the implementation of a VSD front-end IC has been carried out. Manufactured in the SG25H3 SiGe:C BiCMOS technology from IHP GmbH, Germany, this IC integrates a heterodyne radar transceiver, similar to the VISDAM RF front-end. Compared to VISDAM, the IC is designed to operate at a higher carrier frequency around 24 GHz potentially increasing the sensitivity for a future VSD instrument. The IC includes LO buffering and quadrature splitting, up- and down-conversion SSB mixers and two cascaded receiver LNA's. The RF signal source (LO source) has not been included. Measurements reveal some smaller discrepancies when compared to simulations. However, the obtained performance of the VSD IC, show that it is suitable for replacing large parts of a CW VSD instrument at 24 GHz.

Technical University of Denmark
Kgs. Lyngby, Denmark
July, 2012

Brian Sveistrup Jensen

References

[1] M. Khafaji, H. Gustat, and C. Scheytt, "A 6 Bit Linear Binary RF DAC in 0.25 mm SiGe BiCMOS for Communication Systems," in *IEEE/MTT-S International Microwave Symposium*, pp. 916–919, 2010.

[2] J. C. Lin, "Noninvasive Microwave Measurement of Respiration," *Proceedings of the IEEE*, vol. 63, p. 1530, October 1975.

[3] E. F. Greneker, "Radar Sensing of Heartbeat and Respiration at a Distance with Applications of the Technology," in *IEE Proceedings of Radar Systems*, pp. 150–154, 1997.

[4] J. Geisheimer, "RVSM [Radar Vital Signs Monitor]," *IEEE Potentials*, vol. 17, pp. 21–24, December 1998.

[5] A. D. Droitcour, O. Boric-Lubecke, V. M. Lubecke, J. Lin, and G. T. A. Kovacs, "Range Correlation and I/Q Performance Benefits in Single-Chip Silicon Doppler Radars for Noncontact Cardiopulmonary Monitoring," *IEEE Transactions on Microwave Theory and Techniques*, vol. 52, no. 3, pp. 838–848, 2004.

[6] Y. Xiao, J. Lin, O. Boric-Lubecke, and M. Lubecke, "Frequency-tuning Technique for Remote Detection of Heartbeat and Respiration Using Low-Power Double-Sideband Transmission in the Ka-band," *IEEE Transactions on Microwave Theory and Techniques*, vol. 54, no. 5, pp. 2023–2032, 2006.

[7] E. M. Staderini, "UWB Radars in Medicine," *IEEE Aerospace and Electronics Systems Magazine*, vol. 17, pp. 13–18, January 2002.

[8] C. N. Paulson, J. T. Chang, C. E. Romero, J. Watson, F. J. Pearce, and N. Levin, "Ultra-Wideband Radar Methods and Techniques of Medical Sensing and Imaging," in *Proceedings of SPIE - The International Society for Optical Engineering*, vol. 6007, 2005.

[9] F.-K. Wang, T.-S. Horng, K.-C. Peng, J.-K. Jau, J.-Y. Li, and C.-C. Chen, "Single-Antenna Doppler Radars Using Self and Mutual Injection Locking for Vital Sign Detection With Random Body Movement Cancellation," *IEEE Transactions on Microwave Theory and Techniques*, vol. 59, pp. 3577–3587, December 2011.

[10] C. Li, Y. Xiao, and J. Lin, "Experiment and Spectral Analysis of a Low-Power *ka*-Band Heartbeat Detector Measuring From Four Sides of a Human Body," *IEEE Transactions on Microwave Theory and Techniques*, vol. 54, no. 12, pp. 4464–4471, 2006.

[11] C. Li, J. Cummings, J. Lam, E. Graves, and W. Wu, "Radar Remote Monitoring of Vital Signs," *IEEE Microwave Magazine*, vol. 10, pp. 47–56, February 2009.

[12] H.-R. Chuang, Y.-F. Chen, and K.-M. Chen, "Automatic Clutter-Canceler for Microwave Life-Detection Systems," *IEEE Transactions on Instrumentation and Measurement*, vol. 40, pp. 747–750, August 1991.

[13] K.-M. Chen, Y. Huang, J. Zhang, and A. Norman, "Microwave Life-Detection Systems for Searching Human Subjects Under Earthquake Rubble or Behind Barrier," *IEEE TRANSACTIONS ON BIOMEDICAL ENGINEERING*, vol. 27, pp. 105–113, January 2000.

[14] V. M. Lubecke, O. Boric-Lubecke, A. Host-Madsen, and A. E. Fathy, "Through-the-Wall Radar Life Detection and Monitoring," in *International Microwave Symposium*, pp. 769–772, 2007.

[15] C. Gu, J. Long, J. Huangfu, S. Qiao, W. Z. Cui, W. Ma, and L. Ran, "An Instruments-built Doppler Radar for Sensing Vital Signs," in *8th International Symposium on Antennas, Propagation and EM Theory*, pp. 1398–1401, 2008.

[16] C. Gu, C. Li, J. Lin, J. Long, J. Huangfu, and L. Ran, "Instrument-Based Noncontact Doppler Radar Vital Sign Detection System Using Heterodyne Digital Quadrature Demodulation Architecture," *IEEE Transactions on Instrumentation and Measurement*, vol. 59, pp. 1580–1587, June 2010.

[17] I. Mostafanezhad, O. Boric-Lubecke, and V. Lubecke, "A Coherent Low IF Receiver Architecture for Doppler Radar Motion Detector Used in Life Signs Monitoring," in *Proc. IEEE Radio and Wireless Symposium (RWS)*, pp. 571–574, 2010.

[18] Z. Qin, L. Jianhan, A. Host-Madsen, O. Boric-Lubecke, and V. Lubecke, "Detection of Multiple Heartbeats using Doppler Radar," in *IEEE International Conference on Acoustics, Speech, and Signal Processing*, pp. 1160–1163, 2006.

[19] J. M. C. Budge and M. P. Burt, "Range Correlation Effects in Radars," in *Proc. Record of the 1993 IEEE National Radar Conf.*, pp. 212–216, 1993.

[20] A. D. Droitcour, O. Boric-Lubecke, V. M. Lubecke, J. Lin, and G. T. A. Kovacs, "Range Correlation Effect on ISM Band I/Q CMOS Radar for Non-Contact Vital Signs Sensing," in *Proc. IEEE MTT-S Int. Microwave Symp. Digest*, vol. 3, pp. 1945–1948, 2003.

[21] D. Girbau, A. Lázaro, Ángel Ramos, and R. Villarino, "Remote Sensing of Vital Signs Using a Doppler Radar and Diversity to Overcome Null Detection," *IEEE Sensors Journal*, vol. 12, pp. 512–518, March 2012.

[22] Y. Xiao, C. Li, and J. Lin, "A Portable Noncontact Heartbeat and Respiration Monitoring System Using 5-GHz Radar," *IEEE Sensors Journal*, vol. 7, no. 7, pp. 1042–1043, 2007.

[23] C. Li, Y. Xiao, and J. Lin, "A 5GHz Double-Sideband Radar Sensor Chip in 0.18 μm CMOS for Non-Contact Vital Sign Detection," *IEEE Microwave and Wireless Components Letters*, vol. 18, no. 7, pp. 494–496, 2008.

[24] C. Li, J. Ling, J. Li, and J. Lin, "Accurate Doppler Radar Noncontact Vital Sign Detection Using the RELAX Algorithm," *IEEE Transactions on Instrumentation and Measurement*, vol. 59, pp. 687–695, March 2010.

[25] C. Li and J. Lin, "Optimal Carrier Frequency of Non-Contact Vital Sign Detectors," in *Proc. IEEE Radio and Wireless Symp*, pp. 281–284, 2007.

[26] B.-K. Park, O. Boric-Lubecke, and V. M. Lubecke, "Arctangent Demodulation With DC Offset Compensation in Quadrature Doppler Radar Receiver Systems," *IEEE Transactions on Microwave Theory and Techniques*, vol. 55, no. 5, pp. 1073–1079, 2007.

[27] B.-K. Park, V. Lubecke, O. Boric-Lubecke, and A. Host-Madsen, "Center Tracking Quadrature Demodulation for a Doppler Radar Motion Detector," in *Proc. IEEE/MTT-S Int. Microwave Symp*, pp. 1323–1326, 2007.

[28] D. Dei, G. Grazzini, G. Luzi, M. Pieraccini, C. Atzeni, S. Boncinelli, G. Camiciottoli, W. Castellani, M. Marsili, and J. L. Dico, "Non-Contact Detection of Breathing Using a Microwave Sensor," *Sensors*, vol. 9, pp. 2574–2585, April 2009.

[29] F. E. Churchill, G. W. Ogar, and B. J. Thompson, "The Correction of I and Q Errors in a Coherent Processor," *IEEE Transactions on Aerospace and Electronic Systems*, vol. AES-17, pp. 131–137, January 1981.

[30] B.-K. Park, S. Yamada, and V. Lubecke, "Measurement Method for Imbalance Factors in Direct-Conversion Quadrature Radar Systems," *IEEE Microwave and Wireless Components Letters*, vol. 17, no. 5, pp. 403–405, 2007.

[31] C. Li and J. Lin, "Complex Signal Demodulation and Random Body Movement Cancellation Techniques for Non-Contact Vital Sign Detection," in *IEEE MTT-S International Microwave Symposium Digest*, pp. 567–570, 2008.

[32] C. Li and J. Lin, "Random Body Movement Cancellation in Doppler Radar Vital Sign Detection," *IEEE Transactions on Microwave Theory and Techniques*, vol. 56, pp. 3143–3152, December 2008.

[33] I. Mostafanezhad, O. Boric-Lubecke, V. Lubecke, and A. Host-Madsen, "Cancellation of Unwanted Motion in a Handheld Doppler Radar Used for Non-contact Life Sign Monitoring," in *IEEE MTT-S International Microwave Symposium Digest*, pp. 1171–1174, 2008.

[34] T. D. N. IT and T. Agency, "The Danish Interactive Frequency Plan - Regulations on Frequency Bands." Homepage, Feb. 2012.

[35] M. I. Skolnik, *Introduction to Radar Systems*. 1221 Avenue of the Americas, New York, NY, 10020: McGraw-Hill Inc., third ed., 2001. ISBN: 0-07-288138-0.

[36] DTU-Elektro, "DTU-ESA Spherical Near-Field Antenna Test Facility." Available at http://www.dtu.dk/centre/ems/English/research/dtu_esa_facility.aspx.

[37] C. A. Balanis, *Antenna Theory - Analysis and Design*. Hoboken, New Jersey, United States of America: John Wiley & Sons, Inc., third ed., 2005.

[38] D. M. Pozar, *Microwave Engineering - Third Edition.* 111 River Street, Hoboken, NJ 07030, USA: John Wiley & Sons, Inc., 2005. ISBN: 0-471-44878-8.

[39] N. Skou and B. Laursen, "Additional Radar Notes for 30340, NB218," course note, Technical University of Denmark, Department of Electrical Engineering, January 2010.

[40] J. G. Proakis and D. G. Manolakis, *Digital Signal Processing - Principles, Algorithms, and Applications.* Upper Saddle River, New Jersey 07458: Pearson Prentice Hall, fourth ed., 2007. ISBN: 0-13-187374-1.

[41] B. Heinemann, R. Barth, D. Knoll, H. Rücker, B. Tillack, and W. Winkler, "High-Performance BiCMOS Technologies Without Epitaxially-Buried Subcollectors and Deep Trenches.," *Semiconductor Science and Technology*, vol. 22, pp. S153–S157, 2007.

[42] F. Carrara, A. Italia, E. Ragonese, and G. Palmisano, "Design Methodology for the Optimization of Transformer-Loaded RF Circuits," *IEEE TRANSACTIONS ON CIRCUITS AND SYSTEMS*, vol. 53, pp. 761–768, April 2006.

[43] V. Ragonese, A. Scuderi, V. Giammello, and G. Palmisano, "A SiGe BiCMOS 24-GHz Receiver Front-end for Automotive Short-Range Radar," *Analog Integrated Circuits and Signal Processing*, vol. 67, pp. 121–130, October 2011.

[44] M. Kraemer, D. Dragomirescu, and R. Plana, "Accurate Electromagnetic Simulation and Measurement of Millimeter-Wave Inductors in Bulk CMOS Technology," in *Proc. 10th Topical Meeting on Silicon Monolithic Integrated Circuits in RF Systems*, pp. 61–64, 2010.

[45] A. M. Niknejad and R. G. Meyer, "Analysis of Eddy-Current Losses Over Conductive Substrates with Applications to Monolithic Inductors and Transformers," *IEEE Transactions on Microwave Theory and Techniques*, vol. 49, pp. 166–176, January 2001.

[46] C. P. Yue and S. S. Wong, "On-Chip Spiral Inductors with Patterned Ground Shields for Si-Based RF IC's," *IEEE Journal of Solid-State Circuits*, vol. 33, pp. 743–752, May 1998.

[47] K. T. Ng, B. Rejaei, and J. N. Burghartz, "Substrate Effects in Monolithic RF Transformers on Silicon," *IEEE Transactions on Microwave Theory and Techniques*, vol. 50, pp. 377–383, January 2002.

[48] A. M. Niknejad and R. G. Meyer, "Analysis, Design, and Optimization of Spiral Inductors and Transformers for Si RF IC's," *IEEE Journal of Solid-State Circuits*, vol. 33, pp. 1470–1481, October 1998.

[49] C. P. Yue, C. Ryu, J. Lau, T. H. Lee, and S. S. Wong, "A Physical Model for Planar Spiral Inductors on Silicon," in *IEEE Technical Digest - International Electron Devices Meeting* (Anon, ed.), pp. 155–158, IEEE, 1996.

[50] F. Korndörfer, M. Kaynak, and V. Mühlhaus, "Simulation and Measurement of Back Side Etched Inductors," in *Proc. 40th European Microwave Conference*, pp. 1631–1634, September 2010.

[51] M. Fairburn, J. J. Minnis, and J. Neale, “A Novel Monolithic Distributed Mixer Design,” in *IEE Colloquium on Microwave and Millimetre Wave Monolithic Integrated Circuits*, pp. 13/1–13/6, 1988.

[52] I. D. Robertson, A. A. Rezazadeh, S. Lucyszyn, K. K. M. Cheng, U. Karacaoglu, M. Gillick, C. Samson, D. M. Brookbanks, R. G. Arnold, M. W. Geen, S. J. Nightingale, J. S. Joshi, and J.-F. Luy, *MMIC Design*, vol. 7 of *IEE Circuits and Systems Series*. The Institution of Electrical Engineers (IEE), Editor: I. D. Robertson, 1995. ISBN: 0-85296-816-7.

[53] J. Kaukovuori, K. Stadius, J. Ryynänen, and K. A. I. Halonen, “Analysis and Design of Passive Polyphase Filters,” *IEEE Transactions on Circuits and Systems*, vol. 55, pp. 3023–3037, November 2008.

Chapter 8

ADS Simulation Setup for Direct Conversion VSD Radar

Figure 8.1 shows the human body model implemented in ADS for use in homodyne VSD simulations. Human vital signs are modelled through the use of two sine-wave generators and a voltage-to-phase modulator while path loss is taken into account using an attenuator. Furthermore, a time delay is added for time displacement due to flight time of the transmitted wave.

Figure 8.2 shows the ADS simulation setup where the human body model is included with the smiley-figure representation. Envelope simulation is carried out such that time delays rather than phase shifts can be utilized for flight time modelling. The offset phase, $\Delta\theta$, from equation (2.10) can be adjusted by tuning the phase shifters going to the IQ mixers.

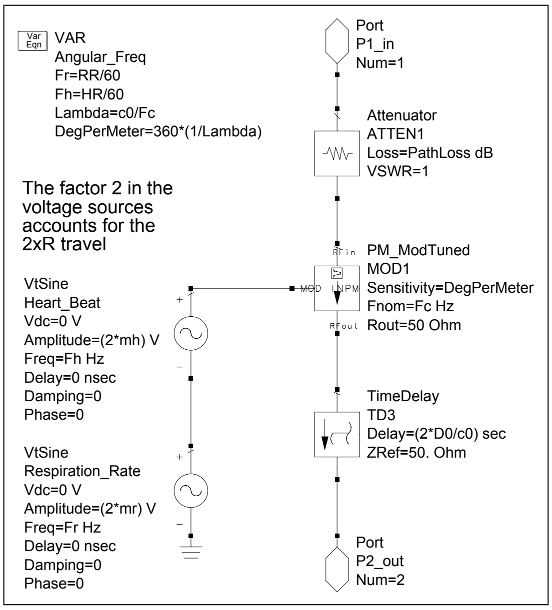

Figure 8.1: Human body model used in ADS setup for evaluating optimum frequency based on amplitude spectrum.

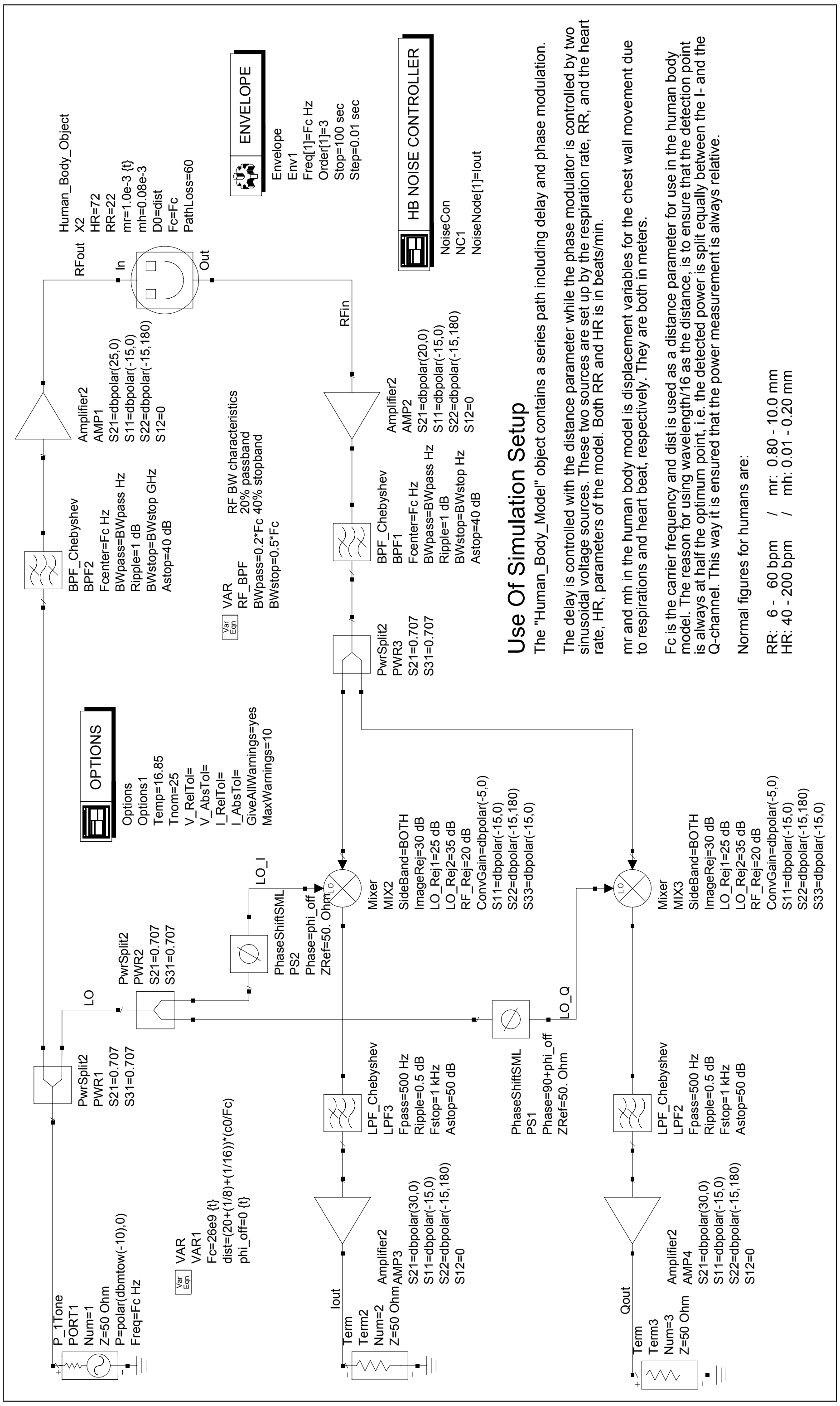

Figure 8.2: ADS simulation setup for estimating the optimum carrier frequency for a VSD instrument that obtains only baseband amplitude spectrum.

Chapter 9

DVD Content: VISDAM Function Set, Matlab Code Examples etc.

DVD

- ***Brian Sveistrup Jensen 2012 - Microwave Instrument for Vital Signs Detection and Monitoring.pdf***
  High resolution PDF copy of PhD thesis w. hyperlinks.
- **Matlab**
  Contains matlab scripts used for analysis and examples in Chapter 2.
- **VISDAM**
  - **Firmware**
    Contains the firmware for the PIC18F45K20 control unit. Use Microchip MPLAB and MCC18 compiler to modify the firmware and a PICKit3 debugger to program the device.
  - **LabView_Interface**
    Contains the Labview interface files used in conjunction with the National Instruments PCIe-6251 DAQ card.
  - **Matlab_FunctionSet**
    Contains the Matlab function set used for analysis of the raw VISDAM data. Sample data from the small scale verification test is included.
  - **SCH_and_PCB**
    Contains schematics and pcs's for all VISDAM blocks. Altium designer 2009 or later is needed for opening the projects.

Journal Paper 1 [JP1]

Twelve-bit 20-GHz reduced size pipeline accumulator in 0.25 μm SiGe:C technology for direct digital synthesiser applications

B.S. Jensen, M.M. Khafaji, T.K.Johansen, V. Krozer and J.C. Scheytt

Submitted	:	November 2010
Accepted	:	July 2011
Published	:	January 2012
Journal	:	IET Circuits, Devices & Systems

www.ietdl.org

Published in IET Circuits, Devices & Systems
Received on 23rd November 2010
Revised on 12th May 2011
doi: 10.1049/iet-cds.2010.0399

ISSN 1751-858X

Twelve-bit 20-GHz reduced size pipeline accumulator in 0.25 μm SiGe:C technology for direct digital synthesiser applications

B.S. Jensen[1] M.M. Khafaji[2] T.K. Johansen[1] V. Krozer[3] J.C. Scheytt[2]

[1]Department of Electrical Engineering, Technical University of Denmark, 2800 Kgs. Lyngby, Denmark
[2]IHP Microelectronics GmbH, 15236 Frankfurt (Oder), Germany
[3]Terahertz Photonics, Johann Wolfgang Goethe University, 60438 Frankfurt (Main), Germany
E-mail: bsj@elektro.dtu.dk

Abstract: This article presents a 20 GHz, 12-bit pipeline accumulator with a reduced number of registers, suitable for direct digital synthesiser (DDS) applications. The accumulator is implemented in the IHP SG25H1 (0.25 μm) SiGe:C technology featuring heterojunction bipolar transistors (HBTs) with F_t/F_{max} of 180/220 GHz. The accumulator architecture omits the pre-skewing registers of the pipeline, thereby lowering both power consumption and circuit complexity. Some limitations to this design are discussed and the necessary equations for determining the phase jump encountered each time the control word (synthesised frequency) is changed are presented. For many applications employing signal processing after detection, this phase shift can then be corrected for. Compared to a full pipeline architecture (omitting the input circuitry for the most significant bit, as is customary for such designs), the implemented 12-bit accumulator reduces the number of registers by 55% and the power by approximately 32%, while obtaining the highest clock frequency for SiGe:C accumulators intended for DDS applications.

1 Introduction

Direct digital synthesisers (DDS) are becoming increasingly attractive alternatives to analogue-based phase-locked-loop (PLL) synthesiser counterparts, because of their agility and broadband performance. Compared to PLL techniques, the DDS offer higher-frequency output range (ideally from DC to half the clock frequency, F_{clk}), higher frequency switching speed and greater stability. However, they also have a high number of spurious output components because of the periodic nature of the digital implementation, [1]. Recently, DDS designs running at clock frequencies of up to 32 GHz have been reported in the literature, for example [2–5]. Although requiring large amounts of power and high production costs, these designs have been manufactured in Indium Phosphide (InP) Double-Heterojunction Bipolar Transistor (DHBT) technologies where the cut-off frequency is high because of the high carrier mobility. Recent advances in SiGe:C technologies have yielded heterojunction bipolar transistor (HBT) devices with f_T/f_{max} in the vicinity of 300 GHz [6], while still maintaining low power consumption. Using such technologies for DDS applications yields high levels of integration and the possibility to include Complementary metal-oxide-semiconductor (CMOS) circuits on the same chip. Therefore lately very fast SiGe:C technologies have been utilised to lower the power consumption and die area of DDS ICs, for example [7–10]. However, until now, some of the fastest SiGe:C DDS ICs have been limited to clock frequencies of about 15 GHz.

A simplified block diagram of a standard DDS design utilising a phase increment counter (accumulator) and a look-up table (LUT) containing the sine wave samples, is shown in Fig. 1. Although the counting speed of the accumulator is set by the clock frequency, the so-called frequency control word (FCW) at the input sets the count increment of the accumulator and thereby the synthesised output frequency, according to

$$F_{out} = \mathrm{FCW} \cdot \Delta F, \quad \Delta F = \frac{F_{clk}}{2^j} \tag{1}$$

where ΔF is the frequency resolution of the DDS and j is the number of bits in the phase accumulator. Note from Fig. 1 that only the k most significant bits (MSB) are used for the LUT indexing. This truncation of the accumulator output word is used to reduce LUT size and will result in some higher spurious components, as described in Section 3.1. At higher clock frequencies, to maintain the DDS resolution, that is, small frequency steps, the number of accumulator bits, j, should be increased. This in turn, will increase the overall power consumption and complexity of the DDS.

Many publications have sought to reduce the power consumption of the DDS; however, most of these publications address gate-level designs and/or special techniques to lower the size of the LUT, which traditionally

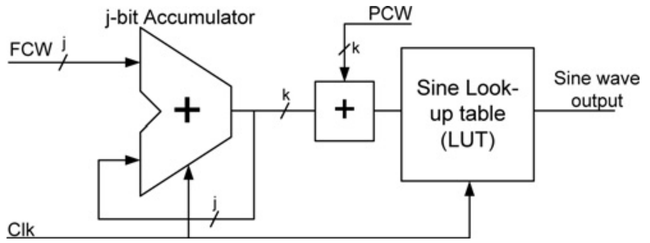

Fig. 1 *Simplified block diagram of a standard DDS architecture*

A j-bit accumulator counts the phase, while the k most significant output bits are used for indexing the sine LUT. FCW controls frequency and PCW modulates phase

has been implemented as a memory block containing the sine-wave samples and connected at the output to a linear digital-to-analogue converter (DAC). Two architectures, [8, 11], reduce the power consumption of the LUT considerably. In [8] and also later in [5], the memory block and the linear DAC were replaced with a sine-weighted DAC. However, a weighted DAC design is often more complicated and will often consume more power than a linear one, so in [11] yet another architecture was considered (Fig. 2). Here the MSB of the accumulator inverts all the bits to produce a digital triangle waveform instead of the normal ramp waveform. The LUT is then implemented with a linear DAC and a bipolar differential pair as the triangle-to-sine wave converter, [12].

In [13], it was sought to lower the accumulator power consumption by implementing a pipelined split-accumulator architecture and a special pre-skewing scheme for the pipeline registers.

This work considers the feasibility of completely removing all pre-skewing registers in the pipeline accumulator. This implementation has been suggested before, [14], however, without considering in detail the consequences and the exact relationship between the switching of the FCW and the associated phase jump. Here a mathematical treatment is given together with a discussion of the benefits and drawbacks of this implementation and a reduced size 20 GHz 12-bit accumulator suitable for use in the DDS architecture of Fig. 2 is presented.

In the next section the reduced-size accumulator is introduced and the equations for determining phase jumps associated with a change of synthesised frequency are presented. Furthermore, the circuit reduction and associated lowering of the power consumption is presented. Sections 3 and 4 then discuss the design of the implemented accumulator IC and the measurements carried out, respectively. Finally, Section 5 gives the conclusion.

2 Pipeline accumulator without pre-skew registers

For high-speed operation the accumulator is implemented as a pipeline accumulator in which registers are used to pre- and post-skew the input- and output data, respectively. An example of a 5-bit pipeline accumulator is given in Fig. 3. It can be seen that once the accumulator has been operated for K_{flush} clock cycles corresponding to the number of pipeline stages (e.g. six clock periods for the 5-bit example), the output becomes valid (O_{ACC} increments with a steady rate) and the pre-skewing registers are not changed before the FCW is updated again. The post-skewing registers are important for aligning the output data to the LUT. If a phase jump, $\Delta\Phi_{\text{err}}$, can be allowed each time FCW changes, the pre-skewing registers can be omitted to save power and reduce circuit complexity. The synthesised frequency, after changing FCW, will be the same as in the traditional DDS, once the accumulator has settled. Traditionally, this approach has been avoided, because some applications do not tolerate a non-continuous phase, thereby losing the ability for the DDS design to be an all-purpose building block. However, as will be discussed next, for many applications this phase jump is in fact not a problem.

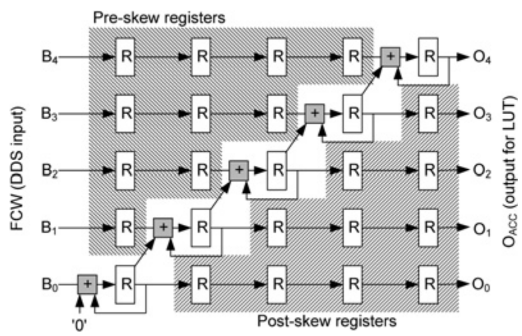

Fig. 3 *Example of 5-bit standard pipeline accumulator for use in DDS*

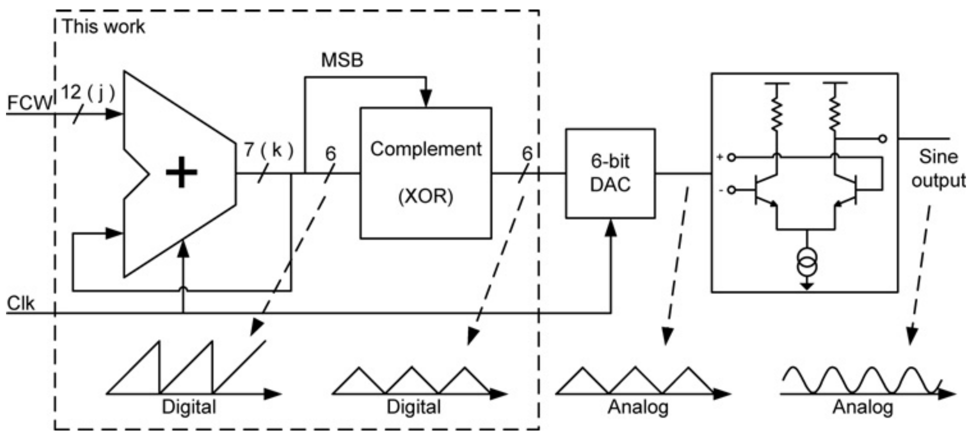

Fig. 2 *DDS architecture that reduces power consumption by implementing the LUT as a linear DAC connected at the output to a differential bipolar pair for triangle-to-sine conversion, as described in [11]*

Chip implemented in this work includes the 12-bit accumulator and the complement circuit (XOR) for digital ramp-to-triangle conversion

IET Circuits Devices Syst., 2012, Vol. 6, Iss. 1, pp. 19–27
doi: 10.1049/iet-cds.2010.0399

The use of DDS-type local oscillators (LO) in transceiver systems enables fast switching (multiplexing) between different frequency bands and reduction in complexity, as the DDS allows both the frequency and the phase to be directly modulated. Most receiver types receiving either amplitude-, phase- or frequency-modulated (AM, PM and FM, respectively) signals, employ a constant LO frequency and thus can use the DDS as LO. For transmitters employing amplitude modulation schemes, such as single- or double-sideband AM, quadrature amplitude, amplitude shift keying etc. where frequency and phase of the LO are constant during up- and down conversion, the use of the reduced-size DDS as LO is also allowed. The standard implementation of phase modulation in DDS designs is indicated in Fig. 1. Here a phase control word (PCW) is added to the accumulator output. As a result, once the frequency is stable after a change in FCW, the DDS can directly be used for standard phase modulation types such as simple PM, phase shift keying (PSK), quadrature PSK, continuous phase modulation etc. If the DDS is to be used for frequency modulation in transmitters, only frequency shift keying (FSK) will operate correctly, as this is the only frequency modulation scheme that does not require a continuous phase, as does simple FM and continuous phase FSK. The only exception to this is in transmitters used for radar applications. If the value of a phase jump created by switching the DDS frequency can be determined, then radar applications monitoring phase and/or frequency can use the DDS for frequency chirps and then correct for the jumps in the signal processing part of the receiver.

2.1 Phase jump determination

Imagine that the pre-skewing registers in Fig. 3 for the 5-bit accumulator are omitted. Each time the FCW is changed, the input bits to the five adders are not aligned. In fact, all bits except for the least significant bit (LSB), B_0, will reach the adders too soon, creating a jump in the accumulator output value, O_{ACC}. Based on the frequency setting before and after the switching, FCW_1 and FCW_2, respectively, the jump of the accumulator output, ΔO_{ACC}, can be determined as follows

$$\Delta O_{\mathrm{ACC}} = \sum_{n=0}^{j-1} n(B_{n,2} - B_{n,1})2^n \quad (2)$$

where $B_{n,x}$ represents bit n in FCW_x. The equation states that each bit, corresponding to a specific value (i.e. $2^3 = 8$ for B_3) will add to the counter jump, ΔO_{ACC}, according to the missing delay in front of the adders. For example, depending on whether B_3 changes upwards (0 to 1) or downwards (1 to 0), and because this bit is missing three delays, the accumulator will count three times 2^3 (i.e. in total 24) too much, or too little, respectively. It is important to note that (2) does not say anything about the value during the switching, that is, before the pipeline has been flushed (K_{flush} clock cycles have passed). It only determines the steady-state counting error. Now, as the phase resolution of the DDS is determined by $\Delta\Phi = 2\pi/2^j$ it is possible to find the phase jump, $\Delta\Phi_{\mathrm{err}}$, as follows

$$\Delta\Phi_{\mathrm{err}} = \Delta O_{\mathrm{ACC}}\Delta\Phi = \frac{\Delta O_{\mathrm{ACC}}}{2^{j-1}}\pi \quad (3)$$

Note that (3) sometimes predicts phase jump values outside

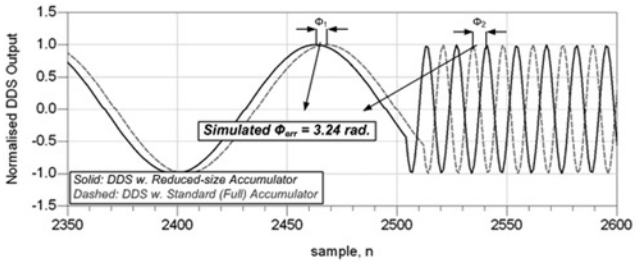

Fig. 4 *Simulated output waveform of a 12-bit DDS using the seven MSBs from the accumulator for LUT indexing*

Number of samples across 2π radians is different for the two cases of FCW values

the range $[-2\pi, 2\pi]$. As these values do not have physical influence on the output after LUT and digital-to-analogue conversion, such phase jumps should be wrapped to be within the range $[-2\pi, 2\pi]$. Fig. 4 shows an Agilent Ptolemy simulated discrete-time waveform example of a 12-bit DDS using 7 bits for LUT indexing. The initial phase difference between the waveform of the reduced-size design and the traditional design is due to the initial skew created during start-up of the circuits. At sample 2500, FCW is changed from 32 to 300, which is seen to result in not only higher frequency but also a phase jump ($\Phi_1 < \Phi_2$) simulated to be $\Delta\Phi_{\mathrm{err}} = \Phi_2 - \Phi_1 = 3.24$ rad. Using (3) we obtain $\Delta\Phi_{\mathrm{err}} = 3.19$ rad. The difference between the simulation and the calculation is owing to the finite precision caused by the truncation of the five LSBs.

2.2 Circuit reduction

As is also indicated in Fig. 1, many high-speed high-resolution DDS designs truncate some accumulator LSBs to reduce the LUT size. Furthermore, as a DDS can only synthesise up to the Nyquist frequency (half the clock frequency), the pre-skewing registers for the MSB are omitted. The input for this bit is then internally biased to a logic low value. When compared with a full pipeline design employing these standard circuit reductions, the 12-bit accumulator presented here reduces the number of registers from 105 to 50. Furthermore, this reduction also lowers the requirement to the clock tree and thus clock buffers; so in total the power reduction is approximately 32%.

3 Accumulator design

The accumulator is implemented in the IHP SG25H1 (0.25 μm) SiGe:C technology, [15], using a traditional pipeline design with 1-bit adders for maximum speed, as shown in Fig. 5. Note that the MSB output of the accumulator core controls the Exclusive-Or (XOR)-gates at the remaining outputs to create the complement function indicated in Fig. 2 and thus to create triangle waveforms. In the following, some of the most important design choices will be discussed.

3.1 Frequency- and phase resolution for DDS application

The design of the accumulator is driven by a desire to have a frequency synthesiser able to synthesise up to some 10 GHz signals with a frequency resolution, ΔF, better than 6 MHz. Using $j = 12$ in (1) we obtain $\Delta F = 4.9$ MHz.

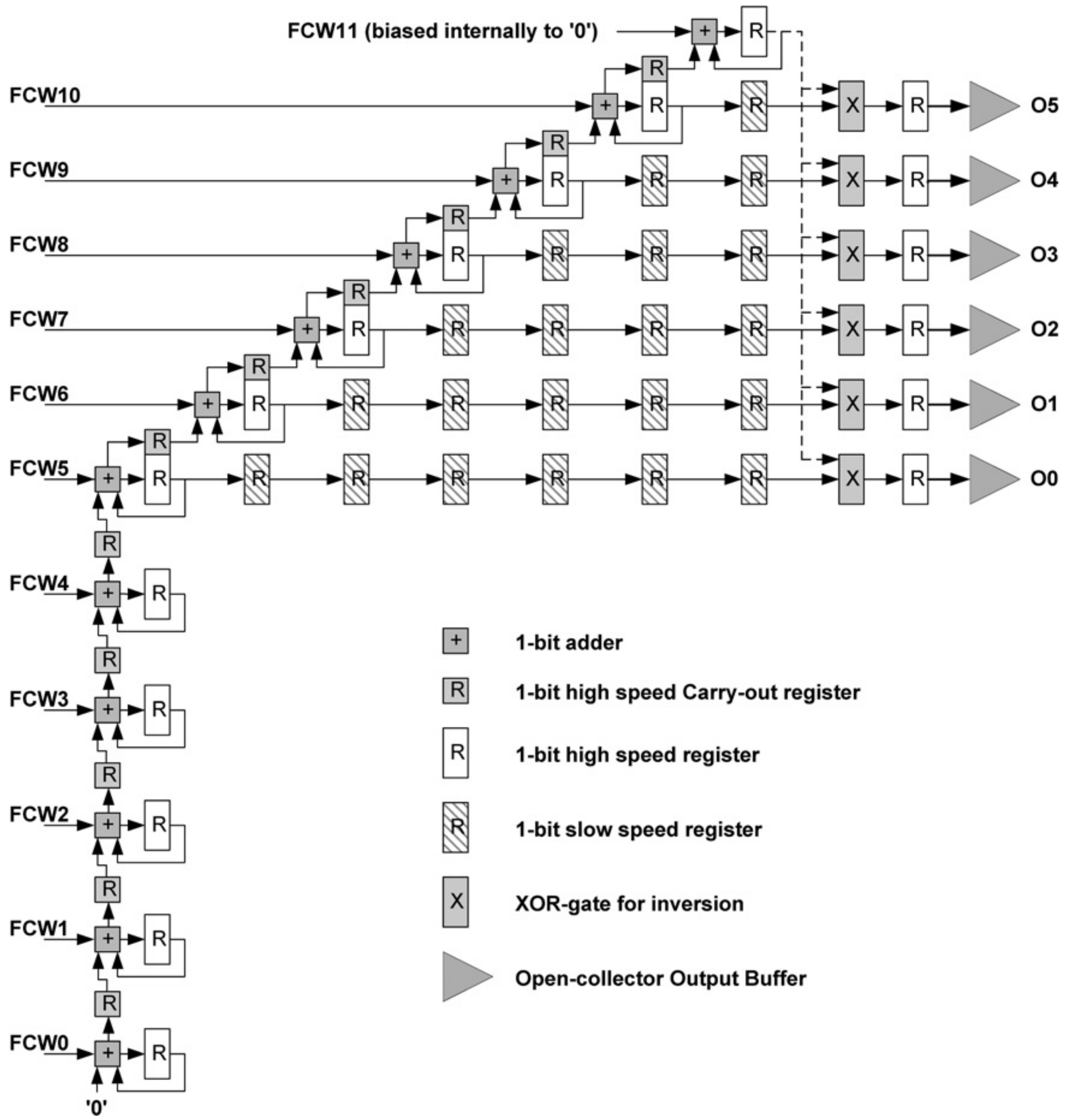

Fig. 5 *Block diagram of the reduced pipeline accumulator*

All registers are clocked at the same time, as discussed in Section 3.3 on the clock tree

One of the drawbacks of a DDS, compared to a PLL, is that many spurious frequencies are created because of the periodic nature of a counting accumulator. The spurious free dynamic range (SFDR) of a DDS using k bits for sine-wave look-up (see Fig. 2) can be estimated by [16]

$$\mathrm{SFDR} \simeq 6.02k - 3.992\ (\mathrm{dB}) \quad (4)$$

So for a DDS implemented with the accumulator presented here with $k = 7$ we should expect SFDR $\simeq$ 38.15 dB. Note that (4) do not take into account the effect of DAC non-linearity and the finite number of amplitude bits, which contribute to the creation of spurious frequencies, as well.

3.2 SiGe differential emitter-coupled logic (DECL) gates

In order to reach the desired clock speed of 20 GHz, the accumulator is implemented with DECL. As DECL is of the non-saturation-type logic with a more or less constant current in each cell (i.e. small difference between dynamic and idle current) the power consumption is high compared to other types of logic.

The DECL sum-output and carry-output gates used for the 1-bit adders are shown in Fig. 6. The sum-output circuit is implemented with two cascaded XOR-gates whereas the carry-output circuit is implemented as a majority gate [17] in which the total current in the cell is divided among three parallel differential bipolar pairs acting as the inputs. All gates in the pipeline core, that is, XOR-gates and latches for the registers, Figs. 6*b* and *d*, operate with a single-ended internal signal swing of 200 mV. The only exception is the majority gate in Fig. 6*c*, which uses a 400 mV signal swing. The reason for this is that whenever two of the inputs have the same logic value, and the third is not equal to those, the signal swing will be reduced to one-third of the maximum swing encountered when all inputs are the same – what will here be referred to as the nominal swing. For a 200 mV nominal swing this would mean that the reduced swing would be only 67 mV which is not desirable as it approaches the thermal voltage. Instead, for a swing of 400 mV the reduced swing is 133 mV.

IET Circuits Devices Syst., 2012, Vol. 6, Iss. 1, pp. 19–27
doi: 10.1049/iet-cds.2010.0399

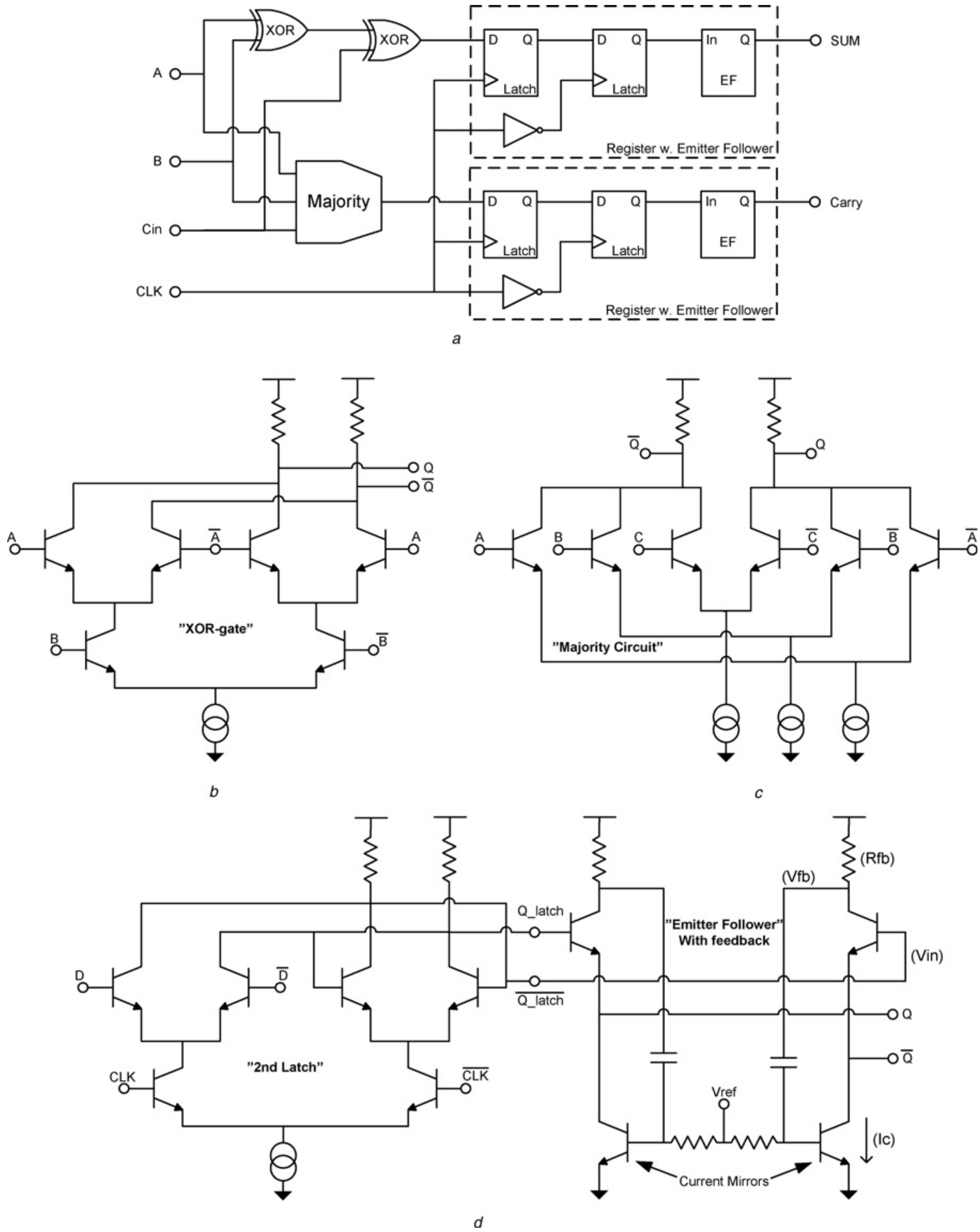

Fig. 6 *DECL gates used in the 1-bit adder circuits*

a Block diagram of the adder
b XOR-gate used for sum-output circuit
c Majority gate used for carry-output circuit
d Second latch and the output EF with feedback used for the fast registers

Two different latches have been designed for use in pipeline registers – a fast one and a slow one, as indicated in Fig. 5. The fast one is needed at the outputs of the adders, see Fig. 6*a*, where they have been optimised to be able to latch the signals going through the calculation circuitry. The low-speed latch is used for post-skewing registers as no calculations are needed in between these. As speed is proportional to current, this reduces power consumption.

Fig. 6*d* shows the last of two latches used for the fast registers together with an emitter follower (EF) on the output. The latch design is rather standard DECL; however, the EF includes feedback through capacitors to facilitate a small amount of peaking. When the input (V_{in}) to the EF decreases, the current in the EF, and thus the voltage drop across the feedback resistor, R_{fb}, becomes lower. The result is that the feedback voltage, V_{fb}, and thus the current drawn through the current mirror, I_{c}, becomes higher. This helps discharging any capacitive loading caused by the next stage. On the other hand when the input increases, the current through the current mirror is lowered, which means that more current is allowed to flow to the capacitive load. As seen from the schematic, the EF current mirrors do not use resistors on the emitter for degeneration, as this would counteract the feedback action. All other current mirrors on the chip use approximately 200 mV drop over the degeneration resistors.

DECL gates use EFs at the outputs not only to drive subsequent circuitry but also to lower the signal level to match that of the next gate. However, EFs are extremely power hungry, and so for all gate outputs that only drive one subsequent gate, the EF is omitted. As can be seen from, for example, Fig. 6 this means that for the subsequent gate, the input HBTs (input A in Fig. 6*b*) will have their base–collector junction slightly forward biased because of the base having a higher potential than the collector. However, the associated reduction in speed is not significant for such low signal swings and the extra current needed to overcome this speed reduction is often much less than that needed for driving two EFs at the differential output.

3.3 Clock tree

For circuits operating at multi-GHz frequencies it is important that clock skew, either positive or negative, is controlled very carefully. Negative clock skew, as defined in [18] can be used to speed up pipeline circuits; however, if the negative clock skew is more than the signal delay through each digital block, the pipeline becomes ineffective in that the signals will be swept through the registers rather than being latched. Positive clock skew, on the other hand, will make the circuit slower. In order to be able to control the clock skew precisely, the three-level clock tree shown in Fig. 7 has been implemented. As shown, each clock buffer in a given level drives exactly the same number of buffers or registers, making all the clock signals arriving to the registers at the same time. The clock tree has been laid out

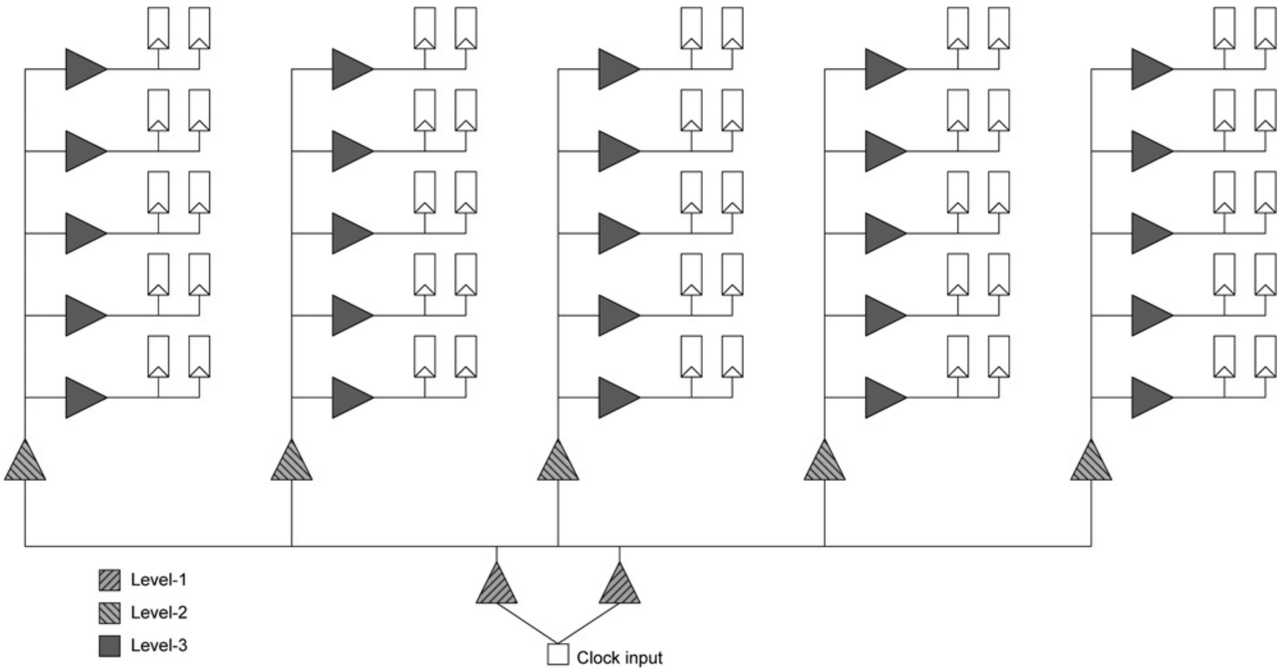

Fig. 7 *Block diagram of the three-level clock tree implemented for the pipeline accumulator*

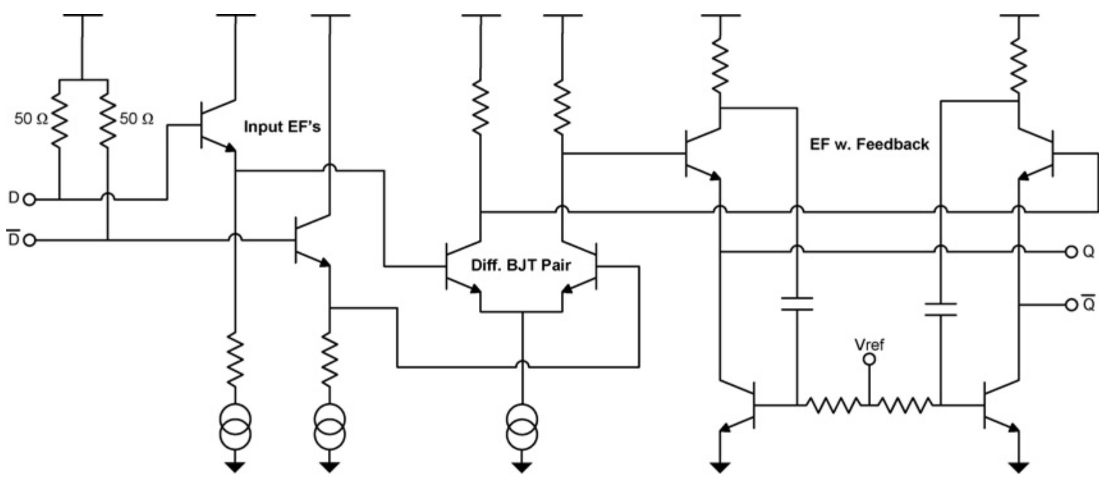

Fig. 8 *Input differential clock buffer mathed to 50 Ω and with output EF stage for high drive capability*

IET Circuits Devices Syst., 2012, Vol. 6, Iss. 1, pp. 19–27
doi: 10.1049/iet-cds.2010.0399

carefully to ensure that lines have the same length, thereby minimising skew because of unequal travel paths.

Fig. 8 shows the input clock buffer, which deviates slightly from the internal clock buffers in that it includes an input EF stage with 50 Ω matching resistors connected to V_{CC}. Internal buffers omit this EF stage and matching resistors and take the input signal directly from the buffer in front of it. All clock buffers have a powerful output EF to drive the high loading created by the subsequent buffer stages and registers. These EF stages use the same feedback scheme as was used in Fig. 6*d* for the high-speed latch output.

3.4 Output buffers

When the accumulator is to be integrated on the same chip together with a linear DAC and a bipolar pair as the triangle-to-sine converter to form a complete DDS, no output buffers are needed for the accumulator itself. However, to test the accumulator separately, output buffers are needed. Each output is therefore equipped with an open-collector differential buffer, see Fig. 9, designed to deliver a 300 mV single-ended swing across a 50 Ω load resistor. This design is chosen as the preceeding circuitry – whether being test equipment or a high-speed DAC – is often equipped with 50 Ω input matching resistors, across which a current can be drawn. The current through the open-collector differential pair is approximately 6 mA which is high compared to all other current switches in the design; so to be able to drive the output stage, an EF is added to the input of the output buffers as indicated in the figure. As seen, the topology of this EF again follows that of the output for the fast latches and the clock buffers, Figs. 6*d* and 8, respectively.

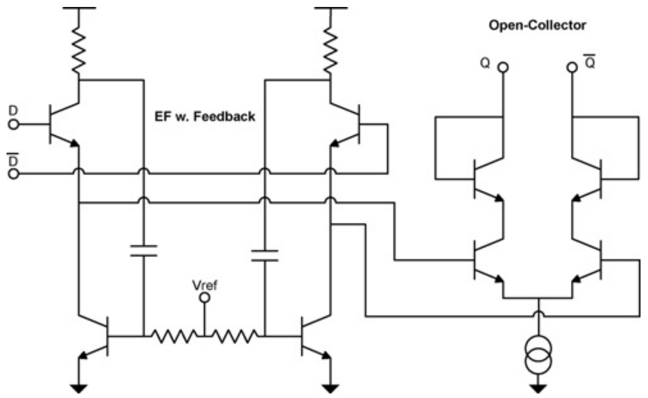

Fig. 9 *Differential open-collector output buffer with input EF implemented to be able to test the accumulator seperately*

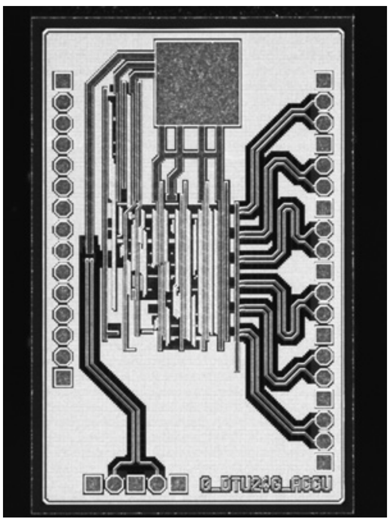

Fig. 10 *Photograph of the 12-bit accumulator die*

Chip size is 2.25 × 1.43 mm

3.5 Final accumulator IC

A photograph of the final accumulator IC is shown in Fig. 10. The IC measures 2.25 × 1.43 mm with an accumulator core area of approximately 0.66 mm^2. The core includes a total number of around 4500 transistors. The measured core power consumption is approximately 1.08 W without including the output buffers as these will be omitted when the accumulator is to be integrated with a DAC in a final DDS design.

4 Measurements

The accumulator IC has been measured on-wafer with a Tektronix TDS 6154G digital storage oscilloscope for real-time voltage curve measurements. Only one output bit was measured at a time while the remaining ones were connected directly to VCC. The monitored output is taken on-wafer with a *Z*-probe and fed through a bias-*T* where the DC connection is connected to supply and the AC-connection is connected to the oscilloscope which is internally matched to 50 Ω. The test set-up limits the clock frequency to about 20 GHz.

4.1 Output waveforms and power consumption

The simulated current at 3.0 V supply voltage was approximately 325 mA, however, when the IC was measured, the current at 3.0 V supply was only 284 mA. All current mirrors are internally biased (no external reference pin); so to reach the desired supply current and thus speed of the IC, the supply voltage had to be increased to 3.27 V, thus increasing the power consumption from the simulated 975 mW to approximately 1.08 W.

Fig. 11 shows output curves from the LSB for three different settings of FCW, that is, FCW = 2, 4 and 8. For all the presented output curves, the inverting/complement

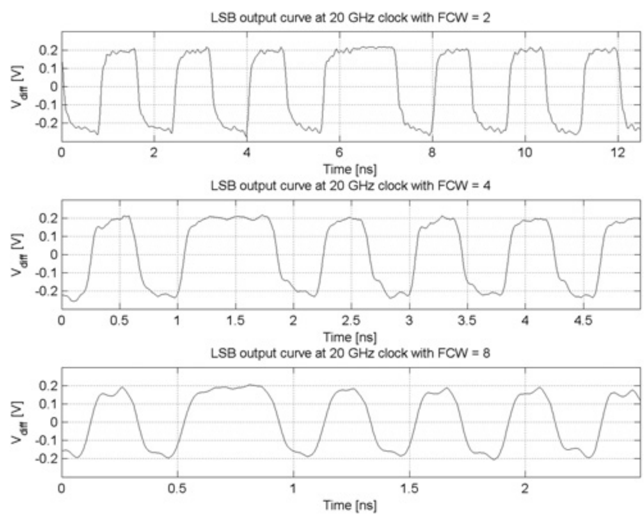

Fig. 11 *Measurements of LSB output at a clock frequency of 20 GHz for three different FCW settings (FCW = 2, 4 and 8)*

LSB is monitored with a Tektronix digital storage oscilloscope while remaining outputs are connected directly to VCC

Table 1 Measured LSB output frequencies and peak-to-peak voltages

FCW	Fund. freq. from oscilloscope data, MHz	Expected feq., MHz	Output diff. swing V_{PP_LSB}, mV
1	312.6	312.5	564
2	625.8	625	534
4	1259	1250	492
6	1887	1875	482
8	2513	2500	412
10	3175	3125	400
12	3745	3750	399
16	4975	5000	371

function (recall from Fig. 2) is captured to illustrate the functionality of the output XOR-gates. Table 1 shows a list of measured LSB output frequencies together with the differential peak-to-peak voltage, V_{PP_LSB}, for various different FCW settings. The fundamental frequencies have been obtained through the use of Matlab, by applying the auto-correlation function to the raw output data of the oscilloscope. By comparing the measured frequency with the expected frequency from simulations with Spectre Cadence, the functionality of the accumulator core can be verified. As seen from Table 1 the measured frequency is very close to the expected one for all respective FCW settings, verifying accumulator core operation. The small frequency differences observed in Table 1 are expected to be caused by the finite number of time-domain periods used in calculating the frequency. This calculation error naturally becomes more significant at higher frequencies as they are closer to the sample rate of the oscilloscope. Note that because of phase bit truncation, the LSB is in fact output bit number 6 from the accumulator, which explains why it is expected that for FCW = 1 the LSB should switch with a frequency of $2^6 \cdot \Delta F = 312.5$ MHz. Only the MSB of the accumulator output (the one used for inverting the ramp) will switch at a frequency of $\simeq$4.9 MHz as stated earlier in Section 3.1 for the minimum frequency step size.

Furthermore, as can be seen from Fig. 11 and in Table 1, when the output switching frequency goes up the peak-to-peak voltage goes down. This is often seen in high-speed digital systems. However, already at FCW = 10 the differential peak-to-peak voltage is at 400 mV, that is, a reduction of 33% compared to the nominal 600 mV, indicating that the output buffers are not fully able to drive the long lines and bias-T's used for the current measurement set-up. As the output buffers were not designed to drive this kind of external circuitry, further measurements of the chip bonded on PCB and connected directly to a high-speed DAC will be conducted in the near future. The DAC used for such future measurements will probably be the newly developed 6-bit DAC from IHP, see [19].

4.2 Comparison

Table 2 shows a comparison between recently published papers and articles on DDS and/or accumulator ICs. Apart from [7], only DDS publications with specification of the accumulator power consumption have been considered. The figure of merit (FoM) used in Table 2 is given by

$$\mathrm{FoM} = \frac{F_{\mathrm{clk}} \cdot j \cdot k}{P_{\mathrm{diss}}} \ (\mathrm{GHz} \cdot \mathrm{bits}^2/\mathrm{W}) \qquad (5)$$

Table 2 Comparison of recently published accumulators for DDS applications

Ref.	Techn.	J^a, bits	k^a, bits	F_{clk}, GHz	Power, W	FoM, (GHz bits^2/W)
[17]	InP	4	4	41	4.1	160
[5]	InP	8	5	32	4.9	261
[2]	InP	8	6	13	2.13	293
[8]	SiGe	8	8	5	0.495	646
[9]	SiGe:C	9	8	11	0.825	960
[10]	SiGe:C	9	8	12	0.825	1047
[3][b]	SiGe:C	9	9	6	0.308	1578
[7][b]	SiGe:C	8	6	15	0.366	1967
this work	SiGe:C	12	7	20	1.08	1557

[a]For j and k refer to Fig. 1
[b]Power consumption is for complete DDS IC

where j is the number of bits in the accumulator and P_{diss} is the dissipated power. Compared to previous reported FoMs this FoM also includes the effective number of bits, k, used for sine-wave look-up (refer to Fig. 2). This has been included because larger values of k will yield lower spurious signals (see Section 3.1) at the expense of a higher power consumption because of the requirement of more post-skew registers.

In [3, 7], only the power consumption of the complete DDS ICs are reported and even at this power consumption, they obtain higher FoMs. However, they do so at 70% and 25% lower clock frequencies, respectively. Furthermore, the frequency step size for [3] is 2.4 times larger (11.7 against 4.9 MHz) compared to the IC presented here, whereas that of [7] has a 12-times-larger step size (58.6 MHz against 4.9 MHz). Thus, the presented IC obtains one of the best FoMs among the reported accumulators and operates at the highest clock frequency among those integrated in SiGe:C technology.

5 Conclusion

This article presented a 20-GHz 12-bit pipeline adder accumulator integrated in IHP SG25H1 (0.25 μm) SiGe:C technology, intended for use in DDS applications. The seven MSBs of the accumulator output are used for the phase look-up operation of the DDS; however, only 6 bits are forwarded to the DAC, because the MSB is used for inversion of the counting operation to create a digital triangle output. In order to lower power consumption and circuit complexity, all the pre-skewing registers of the accumulator were omitted from the design. The benefits and drawbacks of this reduced pipeline architecture with respect to a DDS application have been discussed and equations for finding the resulting phase jump encountered when switching the control word (changing the synthesised frequency) are presented. Although the measurement facilities did not allow testing clock frequencies higher than 20 GHz, it can be concluded that this design is the fastest SiGe:C accumulator intended for DDS applications reported so far. The measured power consumption for the accumulator core is 1.08 W without including the output buffers as these will be omitted when the accumulator is to be integrated with a DAC in a final DDS design.

Further measurements of the chip bonded on PCB together with a high-speed DAC and a bipolar differential pair to form a complete DDS system will be conducted in the near future.

doi: 10.1049/iet-cds.2010.0399

6 Acknowledgments

The authors would like to thank IHP GmbH, Frankfurt (Oder), Germany, for making the 0.25 μm SiGe:C technology available and for a great deal of support during the development and testing of this new accumulator. Furthermore, we would like to thank IPtronics A/S, Roskilde, Denmark for their knowledge sharing and design suggestions during the initial development stages of the IC.

7 References

1 Vankka, J., Halonen, K.: 'Direct digital synthesizers: theory, design and applications' (Kluwer Academic Publishers, Dordrecht, The Netherlands, 2001)
2 Turner, S.E., Kotecki, D.E.: 'Direct digital synthesizer with ROM-less architecture at 13-GHz clock frequency in InP DHBT technology', *IEEE Microw. Wirel. Compon. Lett.*, 2006, **16**, (5), pp. 296–298
3 Thuries, S., Tournier, E., Cathelin, A., Godet, S., Graffeuil, J.: 'A 6-GHz low-power BiCMOS SiGe:C 0.25 μm direct digital synthesizer', *IEEE Microw. Wirel. Compon. Lett.*, 2008, **18**, (1), pp. 46–48
4 Turner, S.E., Chan, R.T., Feng, J.T.: 'ROM-based direct digital synthesizer at 24 GHz clock frequency in InP DHBT technology', *IEEE Microw. Wirel. Compon. Lett.*, 2008, **18**, (8), pp. 566–568
5 Turner, S.E., Kotecki, D.E.: 'Direct digital synthesizer with sine-weighted DAC at 32-GHz clock frequency in InP DHBT technology', *IEEE J. Solid-State Circuits*, 2006, **41**, (10), pp. 2284–2290
6 Rücker, H., Heinemann, B., Winkler, W., *et al.*: 'A 0.13 μm SiGe BiCMOS technology featuring f_T/f_{max} of 240/330 GHz and gate delays below 3 ps', *IEEE J. Solid-State Circuits*, 2010, **45**, (9), pp. 1678–1686
7 Laemmle, B., Wagner, C., Knapp, H., Maurer, L., Weigel, R.: 'A 366 mW direct digital synthesizer at 15 GHz clock frequency in SiGe bipolar technology'. IEEE Radio Frequency Integrated Circuits Symp., 2009, pp. 415–418
8 Dai, F.F., Chimakurthy, L.S.J., Yang, D., Huang, J., Jaeger, R.C.: 'A low power 5 GHz direct digital synthesizer designed In SiGe technology'. IEEE Topical Meeting on Silicon Monolithic Integrated Circuits in RF Systems, 2004, pp. 21–24
9 Yu, X., Dai, F.F., Irwin, J.D., Jaeger, R.C.: 'A 9-bit quadrature direct digital synthesizer implemented in 0.18 μm SiGe BiCMOS technology', *IEEE Trans. Microw. Theory Tech.*, 2008, **56**, (5), pp. 1257–1266
10 Yu, X., Dai, F.F., Irwin, J.D., Jaeger, R.C.: 'A 12 GHz 1.9 W direct digital synthesizer MMIC implemented in 0.18 μm SiGe BiCMOS technology', *IEEE J. Solid-State Circuits*, 2008, **43**, (6), pp. 1384–1393
11 Thuries, S., Tournier, E.: 'A DDS-oriented phase-to-amplitude converter using a SiGe:C bipolar transistors differential pair'. IEEE Int. Workshop on Radio-Frequency Integration Technology, Singapore, 30 November–2 December 2005, pp. 211–214
12 Meyer, R.G., Sansen, W.M.C., Lui, S., Peeters, S.: 'The differential pair as a triangle-sine wave converter', *IEEE J. Solid-State Circuits*, 1976, **SC-11**, (3), pp. 418–420
13 Merlo, E., Baek, K.H., Choe, M.J.: 'Split accumulator with phase modulation for high speed low power direct digital synthesizers'. IEEE Proc. 15th Annual IEEE Int. ASIC/SOC Conf., 2002, pp. 97–101
14 Laemmle, B., Wagner, C., Knapp, H., Maurer, L., Weigel, R.: 'High speed low power phase accumulators for DDS applications in SiGe bipolar technology'. IEEE Bipolar/BiCMOS Circuits & Technology Meeting, 2009, pp. 162–165
15 Heinemann, B., Barth, R., Knoll, D., Rücker, H., Tillack, B., Winkler, W.: 'High performance BiCMOS technologies without epitaxially-buried subcollectors and deep trenches', *Semicond. Sci. Technol.*, 2007, **22**, pp. 153–157
16 O'Leary, P., Maloberti, F.: 'A direct-digital synthesizer with improved spectral performance', *IEEE Trans. Commun.*, 1991, **39**, (7), pp. 1046–1048
17 Turner, S.E., Elder, Jr. R.B., Jansen, D.S., Kotecki, D.E.: '4-bit adder-accumulator at 41-GHz clock frequency in InP DHBT technology', *IEEE Microw. Wirel. Compon. Lett.*, 2005, **15**, (3), pp. 144–146
18 Friedman, E.G.: 'Clock distribution networks in synchronous digital integrated circuits', Invited Paper, *Proc. IEEE*, 2001, **89**, (5), pp. 665–692
19 Khafaji, M., Gustat, H., Scheytt, J.: 'A 6 bit linear binary RF DAC in 0.25 μm SiGe BiCMOS for communication systems'. Proc. IMS, 2010, pp. 916–919

Conference Paper 1 [CP1]

Vital Signs Detection Radar using Low Intermediate-Frequency Architecture and Single-Sideband Transmission

Brian Sveistrup Jensen, Sævar Þór Jónasson, Thomas Jensen and Tom Keinicke Johansen

Conference	:	European Microwave Conference, Amsterdam RAI, The Netherlands, 2012
Accepted	:	Mai 2012

Vital Signs Detection Radar using Low Intermediate-Frequency Architecture and Single-Sideband Transmission

Brian Sveistrup Jensen, Sævar Þór Jónasson
and Tom Keinicke Johansen
Department of Electrical Engineering
Technical University of Denmark
2800 Kgs. Lyngby, Denmark
Email: bsj@elektro.dtu.dk

Thomas Jensen
Ferdinand-Braun-Institut
Leibniz-Institut für Höchstfrequenztechnik
12489 Berlin, Germany
Email: thomas.jensen@fbh-berlin.de

***Abstract*—This paper presents a continuous wave vital signs detection radar that utilizes a heterodyne transceiver architecture with a 10 MHz intermediate frequency to remove both unwanted DC offsets in the electronic components and the so-called null-detection-points. For successful removal of the latter, it is shown that single-sideband transmission (or demodulation) must be used. Measurements verify this behaviour.**

I. Introduction

Measuring human vital signs (heartbeat and respiration rate) unobtrusively has been of great interest since the first wireless sensors were demonstrated in the early 1970's, [1]. The most commonly used non-contact sensor types are in the form of continuous-wave (CW) and ultra-wide-band (UWB) radars, [2]-[4], among which this paper concentrates on the CW type.

The vital signs detection (VSD) radar technology is mainly of interest in medical applications where it has the potential to eliminate the need for wired sensors that often induce discomfort for the patients. Furthermore, it has the potential to be of use for monitoring of infants and the elderly in their homes as well as for certain search and rescue operations and military applications. For these types of sensors to be a viable alternative, they of course need to exhibit a performance comparable with traditional worn sensors.

Typically, due to phase noise limitations of oscillators, especially at radio frequencies, and the fact that the desired vital signs signals are only 0.1 - 3.0 Hz offset from the carrier, mainly direct conversion architectures (also called homodyne or zero-IF) in the form of quadrature (I/Q) and double-sideband (DSB) systems have been used for CW-VSD applications; see the simplified block diagrams of Fig. 1(a) and (b) and [2]-[3].

Going to a low intermediate-frequency (low-IF) heterodyne architecture ([5]-[6]), see Fig. 1(c), has several advantages. In particular DC offsets in the electronic components and channel mismatches seen in homodyne I/Q systems are eliminated. This leads to reduced complexity in the signal processing steps, as curve fitting- and estimation algorithms are not necessary in order to carry out proper arctangent demodulation of the phase signal, [8]. Furthermore, frequency tuning as implemented in the DSB system of [3] is not required.

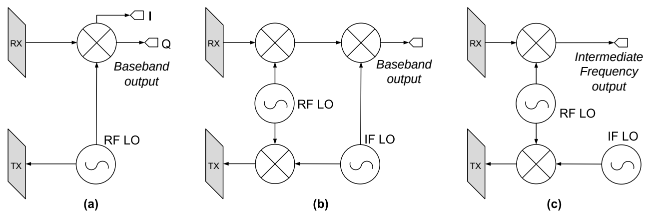

Fig. 1. Simplified block diagrams of (a) traditional quadrature architecture, (b) double-sideband architectures and (c) a low-IF architecture.

While [5] presented the first instrument build heterodyne VSD radar system using a digital I/Q receiver and further [6] sought to evaluate the noise benefits of using a coherent heterodyne architecture compared to homodyne I/Q systems, this paper focuses on the signal theory governing the choise between single- and double-sideband (SSB and DSB) transmission/demodulation. As will be shown, both theory and test measurements dictates that SSB signals should be used in order to eliminate null-detection points.

The heterodyne architecture used in this paper for measurements, implements a 10 MHz IF while data aquisition is carried out on an oscilloscope using sub-sampling techniques. Measurements performed on a living subject is presented and verifies the system's ability to track heart- and respiration rates.

II. DSB vs. SSB transmission/demodulation in Low-IF VSD Radar Instruments

The block diagram of the proposed CW-VSD radar is shown in Fig. 2. The main building blocks consist of an HP 8671B RF signal generator, two Hittite HMC521LC4 I/Q mixers and an AFS42-08001200-15-10P-42 LNA from MITEQ. The IF oscillator is a Vectron C4400A1 oven controlled crystal oscillator (OCXO) followed by a bandpass filter to remove the DC offset and harmonics of the 10 MHz square wave signal. The up-conversion mixer is configured as an SSB mixer (using

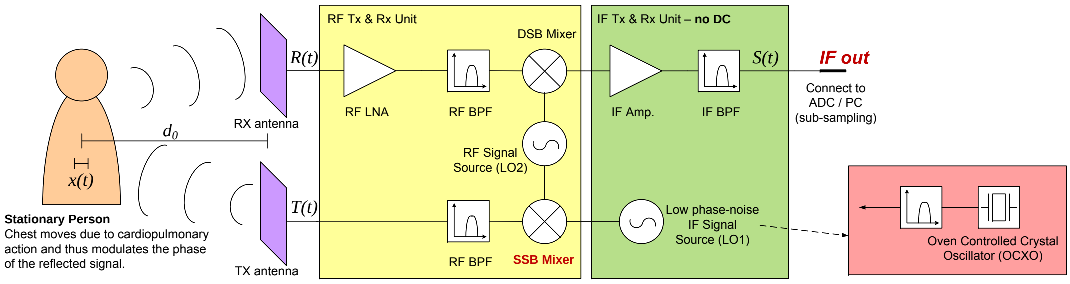

Fig. 2. Block diagram of the proposed low-IF VSD radar architecture.

an IF I/Q splitter). As will be shown next, this configuration is essential for proper removal of the null-point problem.

A. DSB Transmission

To form the transmitted DSB signal, $T_{DSB}(t)$, two frequencies are mixed together. These are the $LO_{RF}(t)$ and $LO_{IF}(t)$ signals respectively,

$$LO_{RF}(t) = \cos\left(\omega_{RF}t + \theta_{RF} + \phi_{nRF}(t)\right) \tag{1a}$$

$$LO_{IF}(t) = \cos\left(\omega_{IF}t + \theta_{IF} + \phi_{nIF}(t)\right) \tag{1b}$$

where ω_{XX} are the angular frequencies and θ_{XX} are phase constants associated with each LO. Furthermore, $\phi_{nXX}(t)$ represent phase noise in each oscillator. Mixing the two signals and keeping only the relevant mixing terms (i.e. sum and difference frequencies), we obtain

$$\begin{aligned} T_{DSB}(t) &= LO_{RF}(t) \cdot LO_{IF}(t) \\ &= \frac{1}{2}\cos\left(\omega_L t + \theta_L + \phi_{nL}(t)\right) \\ &+ \frac{1}{2}\cos\left(\omega_U t + \theta_U + \phi_{nU}(t)\right) \end{aligned} \tag{2}$$

where

$$\omega_L = \omega_{RF} - \omega_{IF} \quad , \quad \theta_L = \theta_{RF} - \theta_{IF} \tag{3a}$$

$$\omega_U = \omega_{RF} + \omega_{IF} \quad , \quad \theta_U = \theta_{RF} + \theta_{IF} \tag{3b}$$

represent the lower and upper sideband frequencies as well as the associated phase terms, respectively. Furthermore,

$$\phi_{nL}(t) = \phi_{nRF}(t) - \phi_{nIF}(t) \tag{4a}$$

$$\phi_{nU}(t) = \phi_{nRF}(t) + \phi_{nIF}(t) \tag{4b}$$

represent the total phase noise associated with each of the two sidebands.

Using the notation from Fig. 2, the time varying distance to the target and back can be represented as

$$d(t) = 2\left(d_0 + x(t)\right) \tag{5}$$

where d_0 is the nominal distance to the target and $x(t)$ is the time varying chest wall movement due to respiration and heartbeat. This change in distance will modulate the phase of the transmitted signal according to

$$\theta_m(t) = \frac{2\pi}{\lambda_i} \cdot d(t) \tag{6}$$

where λ_i is the wavelength of the carrier frequency. In the following, constant phase shifts encountered in the electronic components are assumed to be included in the travel path from (5). Neglecting any path loss, the received signal can now be represented as follows

$$\begin{aligned} R_{DSB}(t) &= \frac{1}{2}\cos\left(\omega_L t + \theta_L + \frac{2\pi}{\lambda_L}d(t) + \phi_{nL}\left(\Delta t\right)\right) \\ &+ \frac{1}{2}\cos\left(\omega_U t + \theta_U + \frac{2\pi}{\lambda_U}d(t) + \phi_{nU}\left(\Delta t\right)\right) \end{aligned} \tag{7}$$

where the phase noise terms have been shifted in time using

$$\Delta t = t - \frac{d(t)}{c} \approx t - \frac{2d_0}{c} \tag{8}$$

where c is the speed of light in air and where the approximation can be used for $d_0 \gg |x(t)|$. The received signal is downconverted using the RF LO signal from (1a). Thus, after band-pass filtering to reject all frequencies outside the IF band, the received IF signal, $S_{DSB}(t)$, can be represented as

$$\begin{aligned} S_{DSB}(t) &= R_{DSB}(t) \cdot \cos\left(\omega_{RF}t + \phi_{nRF}\left(t\right)\right) \\ &\approx \frac{1}{4}\cos\left[\frac{2\pi}{\lambda_L}d(t) + \theta_{RF} + \Delta\phi_{nRF}(t)\right. \\ &\qquad \left. -\omega_{IF}t - \theta_{IF} - \phi_{nIF}\left(\Delta t\right)\right] \\ &+ \frac{1}{4}\cos\left[\frac{2\pi}{\lambda_U}d(t) + \theta_{RF} + \Delta\phi_{nRF}(t)\right. \\ &\qquad \left. +\omega_{IF}t + \theta_{IF} + \phi_{nIF}\left(\Delta t\right)\right] \end{aligned} \tag{9}$$

where

$$\Delta\phi_{nRF}(t) = \phi_{nRF}\left(t - \frac{d_0}{c}\right) - \phi_{nRF}(t) \tag{10}$$

is the residual phase noise from the RF oscillator and where the LO signal for down-conversion is assumed to have a zero phase offset, in accordance with the previous assumption, that any phase offsets are included in the travel path from (5).

At GHz carrier frequencies with low IF offsets it can be assumed that $\lambda_L \approx \lambda_U = \lambda$. Substituting this into (9) and inserting (5), the IF signal, S_{DSB}, can now be rewritten as

$$\begin{aligned} S_{DSB}(t) &= \frac{1}{2}\cos\left(\frac{4\pi}{\lambda}x(t) + \theta_\Sigma + \Delta\phi_{nRF}(t)\right) \\ &\cdot \cos\left(\omega_{IF}t + \theta_{IF} + \phi_{nIF}(\Delta t)\right) \end{aligned} \tag{11}$$

where

$$\theta_\Sigma = \frac{4\pi}{\lambda} d_0 + \theta_{RF} \tag{12}$$

is the constant phase term associated with the RF oscillator and the travel path, $2d_0$. In (11) it can be seen, that the baseband signal is merely a sine wave at the IF frequency with the envelope modulated by the chest wall movement. Although DC offsets can easily be removed, the null-points and optimum-points seen for direct conversion VSD radars will also occur for a low-IF system that transmits (or downconverts with) a DSB signal. Whether the reception is located at a null-point is determined by θ_Σ (i.e. the distance to the target, d_0).

B. SSB Transmission

To avoid the null-point problem in the low-IF architecture, SSB transmission must be used. This can be seen by considering once more the transmitted signal from (2) although now with the lower sideband removed. The transmitted SSB signal can thus be represented as

$$T_{SSB}(t) = \frac{1}{2} \cos\left(\omega_U t + \theta_U + \phi_{nU}(t)\right) \tag{13}$$

while the received signal, $R_{SSB}(t)$, takes the form

$$R_{SSB}(t) = \frac{1}{2} \cos\left(\omega_U t + \theta_U + \frac{2\pi}{\lambda_U} d(t) + \phi_{nU}\left(\Delta t\right)\right). \tag{14}$$

Finally, after down-conversion and filtering to retain only the IF frequency component, the IF signal can now be written as

$$S_{SSB}(t) = \frac{1}{4} \cos\Big[\omega_{IF} t + \frac{4\pi}{\lambda_U} x(t) + \theta_\Sigma + \theta_{IF} + \Delta\phi_{nRF}(t) + \phi_{nIF}\left(\Delta t\right)\Big] \tag{15}$$

which can not be further reduced. For the case of SSB transmission it is thus seen that the IF signal consists of a carrier at the IF frequency with a phase modulated according to the chest wall movement of the subject in front of the VSD instrument. The constant phase term associated with the nominal distance to the target and back no longer affects the signal, because the constant angular frequency, ω_{IF}, ensures that the demodulation will be carried out continuously at different points on the circular signal phasor trajectory, [8].

In the above mathematical treatment, the residual phase noise terms where included for completeness. For a detailed treatment on this noise component and the associated range correlation effect, the interested reader should consult [7].

III. Experimental Measurements

To verify the functionality of the proposed system, several measurements were performed with a laboratory radar setup. Due to limitations of the equipment, coherent measurements, in which the ADC sampling circuitry is locked to the IF oscillator, could not be carried out. This typically results in poorer phase noise performance and greater spectrum spreading. A TekTronix TDS725B oscilloscope was used for sampling and

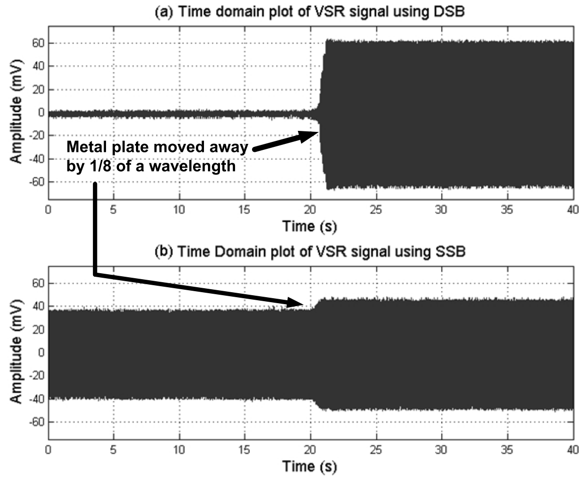

Fig. 3. Metal plate test illustrating SSB versus DSB performance.

although it has the capability to lock the internal time base to an external 10 MHz source, this feature cannot be used since direct tracking of the IF frequency together with the sub-sampling process will place the signal spectrum at DC. This effectively means that null-points arise once more, which is not desirable for the further processing of the signals. Nonetheless, measurements have been carried out and they show promising results, and for the first time in litterature (at the time of writing at least), heartbeat and respiration signals have been obtained using a low-IF VSD radar architecture.

To verify the theory from Section II and to illustrate that SSB signals are indeed prefered over DSB signals, a simple test was set up. A metal plate acting as a strong and constant target was placed in front of the VSD instrument and the distance to the plate was tuned for lowest amplitude output (i.e. null-point), and then halfway through the measurement period, the plate was moved away from the radar 1/8 of a wavelength ($\approx$4.7 mm at 8 GHz carrier). The measurements for both DSB and SSB transmission are shown in Fig. 3. The envelope of the DSB case clearly illustrates that a null-point is present in the beginning of the measurement, while at the end, an optimum point is present. For the SSB case, the change in envelope is approximately 12-15% when the plate is moved. This change agrees well with the finite image rejection of approximately 20 dB in the up-conversion mixer. The measurements verifies that null-points are no longer present in the SSB case.

Fig. 4(a) shows a typical time domain plot of a measurement performed on a subject seated approximately 1 meter from the radar. The frequency difference between the IF oscillator and the internal reference of the oscilloscope is approximately 21.8 Hz and the signals are sampled at 500 Samples/s. The result is a digital signal spectrum going from -250 Hz to +250 Hz with signals located at a center frequency of $\pm$21.8 Hz, as seen in Fig. 4(b). Although null-points are not present, the signal envelope is still modulated. This modulation must be ascribed to changes in effective radar cross section, from when the chest wall is tightened and relaxed during respiration, as well as if

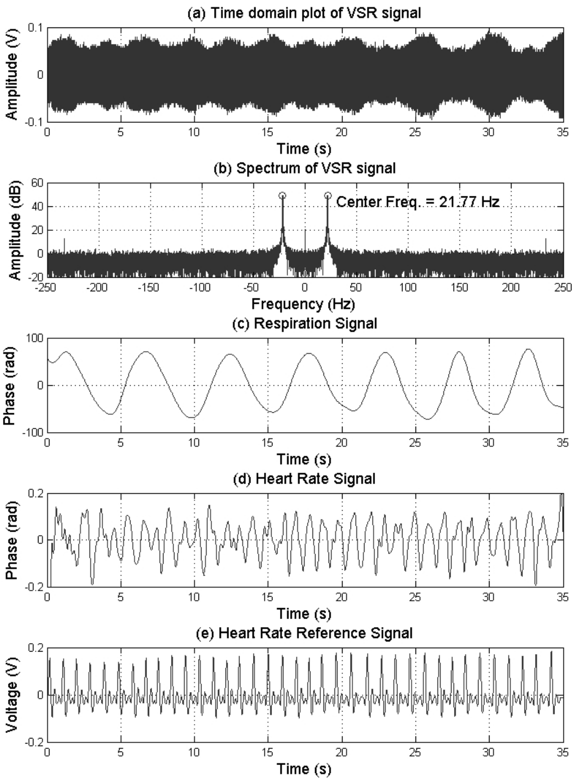

Fig. 4. (a) Time domain and (b) spectrum of raw signal from vital signs measurement (SSB transmission). (c) Respiration and (d) heartbeat signals obtained after digital down-conversion (using method from Fig. 5). Bottom plot (e) shows heart rate reference obtained from a finger pressure sensor.

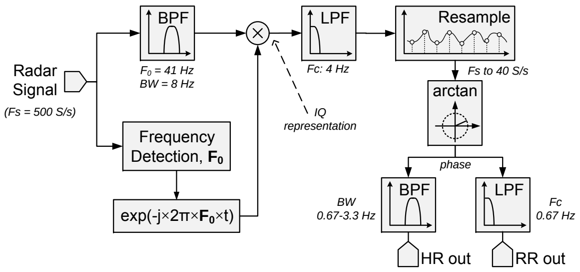

Fig. 5. Block diagram of the signal processing steps done in Matlab.

the angle towards the VSD radar is changing.

Signal processing is carried out to obtain the phase information of the desired signals. The processing steps are illustrated in Fig. 5. After having located the center frequency, and bandpass filtered the incoming signal, a complex exponential carrier is created and multiplied with the signal to obtain a complex baseband signal (i.e. an I/Q representation). This signal is low pass filtered and resampled to a sampling frequency of 40 Samples/s to ease the requirements to the order of the following filters, and thus computational effort. After resampling, the phase is obtained by use of arc-tangent demodulation and finally filters are applied to separate respiration and heartbeat signals. These signals are plotted in Fig. 4(c) and (d) together with the response from a finger pressure heartbeat sensor (Fig. 4(e)), which was used for reference.

To obtain the heart rate based on the signal from Fig. 4(d) an auto-correlation was carried out on a sliding window of 5 second duration. From this, the frequency of the fundamental periodic signal was extracted. Results show that the heart rate measurement stays within 10% of the reference (finger pressure sensor) at all times. Moving towards coherent data acquisition, it is expected that this deviation can be lowered even further. Work is being carried out to update the instrument capabilities for such measurements.

No reference was recorded for the respiration activity. However, simply counting the number of breaths per minute agreed well with the 12 breaths/minute obtained in Fig. 4(e).

IV. Conclusion

A VSD radar using a heterodyne architecture that samples directly at an IF of 10 MHz is presented. Using this low-IF architecture it is possible to eliminate the normal DC offset and null-detection-point problems encountered in direct-conversion tranceivers. This lowers the complexity of the signal processing when doing arctangent demodulation to obtain change in phase caused by the chest wall displacement during heart- and respiration activity. Through theory and measurements is has been shown that null-detection-points are only eliminated if SSB transmission (or demodulation) is used.

Although present instrument limitations do not allow for coherent data acquisition, results show good agreement with the reference heart rate sensor, and stays within 10%.

Acknowledgment

The authors would like to thank the Danish fond "Radiopartsfonden" for financial support.

References

[1] J. C. Lin, "Noninvasive Microwave Measurement of Respiration," Proceedings of the IEEE, p. 1530, 1975.

[2] Amy D. Droitcour, Olga Boric-Lubecke, Victor M. Lubecke, Jenshan Lin and Gregory T. A. Kovacs, "Range Correlation and I/Q Performance Benefits in Single-Chip Silicon Doppler Radars for Noncontact Cardiopulmonary Monitoring," *IEEE Transactions on Microwave Theory and Techniques*, Vol. 52, No. 3, pp. 838-848, March 2004.

[3] Yanming Xiao, Jenshan Lin, Olga Boric-Lubecke and Victor M. Lubecke, "Frequency-Tuning Technique for Remote Detection of Heartbeat and Respiration Using Low-Power Double-Sideband Transmission in the *Ka*-band," *IEEE Transactions on Microwave Theory and Techniques*, Vol. 54, No. 5, pp. 2023-2032, May 2006.

[4] Enrico M. Staderini, "UWB Radars in Medicine," *IEEE AESS Systems Magazine*, pp. 13-18, January 2002.

[5] Changzhan Gu, Changzhi Li, Jenshan Lin, Jiang Long, Jiangtao Huangfu and Lixin Ran, "Instrument-Based Noncontact Doppler Radar Vital Sign Detection System Using Heterodyne Digital Quadrature Demodulation Architecture," *IEEE Transactions on Instrumentation and Measurement*, Vol. 59, No. 6, pp. 1580-1587, June 2010.

[6] Isar Mostafanezhad, Olga Boric-Lubecke and Victor Lubecke, "A Coherent Low IF Receiver Architecture for Doppler Radar Motion Detector Used in Life Signs Monitoring," *IEEE Radio and Wireless Symposium*, pp. 571-574, 2010.

[7] M. C. Budge and M. P. Burt, "Range Correlation Effects in Radars," *IEEE National Radar Conference*, pp. 212-216, 1993.

[8] Byung-Kwon Park, Olga Boric-Lubecke and Victor M. Lubecke, "Arctangent Demodulation With DC Offset Compensation in Quadrature Doppler Radar Receiver Systems," *IEEE Transactions on Microwave Theory and Techniques*, Vol. 55, No. 5, MAY 2007.

Conference Paper 2 [CP2]

Noise Considerations for Vital Signs CW Radar Sensors

Brian Sveistrup Jensen, Thomas Jensen, Vitaliy Zhurbenko
and Tom Keinicke Johansen

Conference	:	European Conference on Antennas and Propagation, Rome, Italy, 2011 - Convened Papers
Published	:	May 2011

Noise Considerations for Vital Signs CW Radar Sensors

Brian Sveistrup Jensen, Thomas Jensen, Vitaliy Zhurbenko, Tom Keinicke Johansen
Department of Electrical Engineering
Technical University of Denmark (DTU)
Oersteds Plads Bygning 348, DK-2800 Kgs. Lyngby, Denmark
bsj@elektro.dtu.dk, tje@elektro.dtu.dk, vz@elektro.dtu.dk, tkj@elektro.dtu.dk

***Abstract*—The use of continuous wave (CW) radars for measuring human vital signs have recently received a lot of attention due to its many promising applications like monitoring people at hospitals or infants at home without the need for wired sensors. This paper briefly presents the typical CW radar setup and the underlying signal theory for such sensors. Then to point out and especially clarify one of the most important effects aiding the design of vital signs radars (VSR), a more detailed discussion concerning phase noise cancellation (or filtering) by range correlation is given. This discussion leads to some general conclusions about which system components are the most critical concerning noise contribution and thus detection accuracy and dynamic range.**

***Index Terms*—Human Vital Signs, CW Radar, Phase Noise, Range Correlation, Spectrum Analysis, Bessel Functions.**

I. Introduction

Measuring human vital signs unobtrusively has been of great interest since the first wireless sensors were demonstrated in the early 1970's, [1]. The most commonly used non-contact sensor types are in the form of continuous-wave (CW) or ultra-wide-band (UWB) radars, [2]- [4]. Although such systems have been conceived and utilised in many applications for several decades, due to lack of sufficient technology the interest in vital signs radar (VSR) systems was limited before the beginning of the new millenium. This paper focuses on recent developments using the CW-VSR sensor type.

The CW-VSR has the potential to eliminate the need for wired sensors that often induce discomfort for the patients and extra work in the form of more strigent hygiene demands for the nursing staff. The technology is mainly of interest for medical applications and monitoring of infants and the elderly, both at hospitals and in their own homes, but it can also easily be of use for certain search and rescue operations as well as military applications.

For these types of sensors to be a viable alternative, they of course have to exhibit a performance that can compete with the traditional worn sensors. Radar sensor performance is limited by transceiver noise and the non-uniform nature of the targets (humans) and the non-static type of behavior that has to be expected from these. This paper discusses noise induced detection limitations in CW-VSR sensors.

II. CW-VSR Setup and Signal Theory

The respiration and heartbeat rates of a human being is in the range from 12 to 30 breaths and 40 to 200 beats per minute respectively, i.e. approximately 0.2 - 3.4 Hz. Measuring such low frequencies with a CW radar would initially seem impossible due to the inherent close-in phase noise of the transmitted signal. However, using the same local oscillator (LO) for both transmitting and down-conversion of the returned signal, the CW-VSR exploits the so-called range-correlation, [5], in which the phase noise of the LO is effectively cancelled while still preserving the desired signals. This section will describe the fundamental signal analysis for CW-VSR's and discuss aspects of the range correlation effect. Furthermore the so-called optimum-points and null-points will be described together with a more rigorous spectral signal representation.

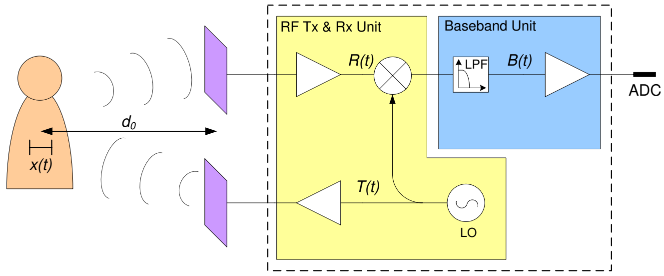

Fig. 1. Typical Block Diagram of a CW-VSR.

A. CW-VSR Baseband Signal

A typical block diagram of a CW-VSR is shown in figure 1. For simplicity reasons the following signal analysis will omit any amplitude constants on the described signals. The transmitted signal generated by the system LO can be represented as follows

$$T(t) = \cos\left(2\pi f_T t + \phi_n(t)\right) \tag{1}$$

where f_T is the transmitted frequency and $\phi_n(t)$ represents the phase noise. Equation (1) omits any constant phase shift that originates in the LO.

The time-varying distance, $d(t)$, that the transmitted signal has to undergo before reaching the radar receiver is given by

$$d(t) = 2 \cdot (d_0 + x(t)) \tag{2}$$

where d_0 is the absolute distance to the target and $x(t)$ represents the chest wall movement due to heart- and respiration activity, i.e. $x(t) = x_h(t) + x_r(t)$. Neglecting any path loss and thus amplitude attenuation, the received signal is now given by

$$R(t) = \cos\left[2\pi f_T t + 2\pi\frac{d(t)}{\lambda_T} + \phi_n\left(t - \frac{d(t)}{c}\right) + \Delta\theta_0\right] \quad (3)$$

where c is the speed of light in free space, $\lambda_T = c/f_T$ is the wavelength of the transmitted signal and where $\Delta\theta_0$ takes into account any constant phase shift that occurs in the electronic components and when the wave is reflected on the chest of the test subject. Also it is seen that the phase noise component, $\phi_n(t)$, is now shifted in time.

Using the transmitter LO, i.e. (1), as LO source for the down-conversion mixer we obtain the following baseband signal after low pass filtering

$$B(t) = \cos\left(2\pi\frac{d(t)}{\lambda_T} + \Delta\phi_n(t) + \Delta\theta_0\right) \quad (4)$$

where

$$\Delta\phi_n(t) = \phi_n\left(t - \frac{2d_0}{c}\right) - \phi_n(t) \quad (5)$$

is called the residual phase noise. Assuming $x(t) << d_0$ in (5), the approximation $d(t) \approx 2d_0$ is used. For $d_0 = 0$ and thus zero time delay it is seen that the receiver would operate as a perfectly matched filter in that it effectively cancels the phase noise. However, as the distance increases, the two terms in (5) become more and more decorrelated, thus effectively increasing the residual phase noise. Intuitively we would also expect the phase noise filtering to work best at the close-in frequencies where variations in $\phi_n(t)$ are slowest. This effect is often referred to as the range correlation effect and was first described in [5] where the attenuation of the phase noise was given as

$$\Gamma(d_0, f_m) = 4\sin\left(\frac{2\pi d_0 f_m}{c}\right)^2 \approx 4\left(\frac{2\pi d_0 f_m}{c}\right)^2 \quad (6)$$

where f_m is the offset frequency from the carrier. The approximation is valid for small offset frequencies where the argument to the sine function becomes small. As an example of the phase noise filtering effect; at an offset frequency of 1 Hz, the attenuation is on the order of 141 dB for a range of 2 meters and the effect is reduced with 6 dB for a doubling of the distance.

B. Null-points and Optimum-points

Not only phase noise has to be considered as a limiting factor for VSR's. Also the so-called null-point problem has to be considered. This effect can be illustrated briefly by inserting (2) into (4) and neglegting the residual phase noise term, $\Delta\phi_n(t)$. Thus the baseband signal can be written as

$$B(t) = \cos\left(4\pi\frac{x(t)}{\lambda_T} + \Delta\theta\right) \quad (7)$$

where

$$\Delta\theta = 4\pi\frac{d_0}{\lambda_T} + \Delta\theta_0 \quad (8)$$

is the total phase shift due to electronic components, reflections and distance to the target. For small phase modulations, $x(t) << \lambda_T$, which is often the case when considering chest wall movements due to heart activity, the baseband signal can be approximated as

$$\begin{aligned} B(t)\Big|_{\Delta\theta = n\frac{\pi}{2}} &\approx \frac{4\pi x(t)}{\lambda_T} &&, \; n = \text{odd int.} \\ B(t)\Big|_{\Delta\theta = n\frac{\pi}{2}} &\approx 1 - \left(\frac{4\pi x(t)}{\lambda_T}\right)^2 &&, \; n = \text{even int.} \end{aligned} \quad (9)$$

in which it is seen that for $\Delta\theta = n\pi/2$ with n being an odd integer the baseband signal is directly proportional to the chest wall movement, $x(t)$, while for n being equal to an even integer this is no longer true. Furthermore, for the later case the variation of the baseband signal as a function of chest wall movement, is at its smallest, thus we call it the null-point. Having realized that the phase distance between optimum points and null-points is $\pi/2$ it is seen from (8) that this crossover occurs every $\lambda_T/8$, thus a small change in absolute distance to the target could potentially move the measurement from optimum to worst-case. To solve this problem two common techniques are often employed; in [2] an I/Q-receiver was used, whereas in [3] double-sideband (DSB) signals were used.

C. Baseband Signal for High Carrier Frequencies and/or Large Respiration Amplitudes

For VSR instruments, the assumption of a low phase modulation, $x(t) << \lambda_T$, used in (9) is normally met for the chest wall movement due to heartbeat activity, as this is in the order of 0.01 to 0.1 mm. However, at high carrier frequencies the chest wall movement due to the respiration activity alone, becomes comparable to the wavelength of the carrier, thus resulting in an increase of the harmonics as well as the intermodulation (IM) products between the respiration- and heartbeat signals. The 'optimum-point/null-point' terminology used in view of equation (9) vanishes in this case, and it becomes important to use a more rigorous spectral treatment. In [6] it was shown that the baseband signal can be written as

$$B(t) = \sum_{k=-\infty}^{\infty}\sum_{l=-\infty}^{\infty}\left[J_l\left(\frac{4\pi m_h}{\lambda_T}\right)J_k\left(\frac{4\pi m_r}{\lambda_T}\right) \cdot \cos\left(k\omega_r t + l\omega_h t + \Delta\theta\right)\right] \quad (10)$$

in which $J_n(x)$ is the Bessel function of first kind, order n with argument x, and where m_h and m_r are the amplitudes of the movement on the chest wall, due to heartbeat and respiration activity, respectively. It is seen that an infinite number of harmonics and IM-products with just as many different amplitudes exist. Based on this type of treatment, it was shown that the IM products and harmonics of the respiration signal could easily become stronger than the heartbeat signal itself, in which case it becomes difficult to sort out the different spectral components based on spectral peaks alone. In fact,

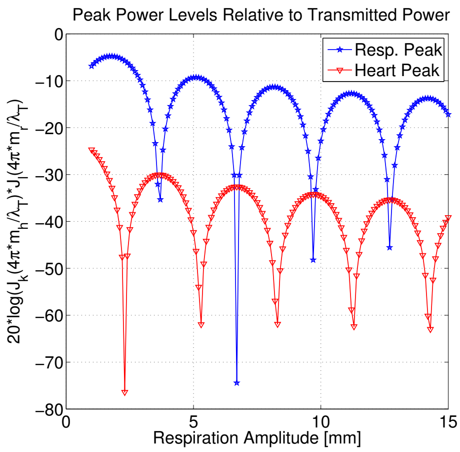

Fig. 2. This plot illustrates the power at the respiration and heartbeat frequencies relative to the transmitted carrier power plotted versus the respiration amplitude. The heartbeat amplitude is fixed at 0.15 mm and the carrier frequency is 25 GHz.

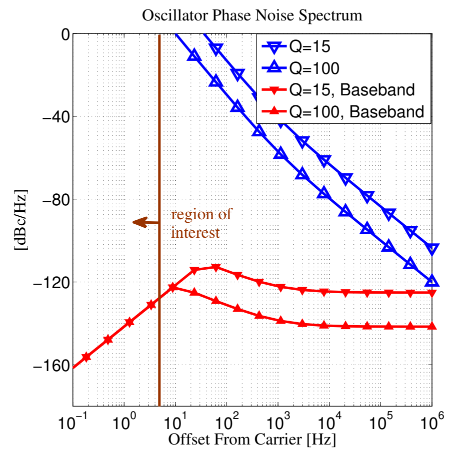

Fig. 3. Phase noise spectrum obtained by using Leesons formula, [7]. Assumed parameters are: VCO frequency, f_{VCO} = 25 GHz, VCO noise figure, $\mathrm{NF}_{\mathrm{VCO}}$ = 15 dB, transistor corner frequency, f_c = 1 kHz and carrier output power, $\mathrm{P}_{\mathrm{carrier}}$ = 10 dBm. The residual baseband phase noise is calculated for a distance, d_0 = 2 meters.

in these situations, where the Bessel function arguments are large, they could potentially fall into a zero crossing of the Bessel function, in which the heartbeat and respiration signals will vanish.

To illustrate this effect, the relative power amplitude peaks of the fundamental respiration and heartbeat signals are plotted in figure 2; i.e. the terms given by

$$\begin{aligned} \text{Fundamental Respiration} &: \quad J_0\left(\frac{4\pi m_h}{\lambda_T}\right) J_1\left(\frac{4\pi m_r}{\lambda_T}\right) \\ \text{Fundamental Heartbeat} &: \quad J_1\left(\frac{4\pi m_h}{\lambda_T}\right) J_0\left(\frac{4\pi m_r}{\lambda_T}\right). \end{aligned}$$

The variation of the transmitted power that is transferred to the two peaks of importance during the phase modulation is clearly seen. The peak power cancellation is in theory infinite when the modulation amplitude is exactly in one of the nulls, but in practice because the measured subject will hardly sit perfectly still, one would probably have to expect variations in the range of 20 dB. It is also seen that when either the respiration peak or heartbeat peak are located at a null, then the other is at the maxima and vice versa; this is due to the fact that the zero crossings of the Bessel function of the first kind $J_n(x)$, for $n = 0$ are close to the maxima for the $n = 1$ function. This makes it impossible to tune (by changing the carrier frequency) both peaks for a maximum at the same time. For lower frequencies, the problem is less severe because the distance between nulls are larger (because the argument to the Bessel function is smaller).

III. LO Phase Noise & VSR Noise Limitations

Analyzing the general LO phase noise spectrum together with the range correlation effect and some absolute power considerations leads to conclusions regarding which noise components dominates in a VSR instrument.

A. LO Close-in Phase Noise

Fig. 3 shows the theoretical Leeson phase noise spectrum, [7], of an oscillator with two different Q-values; Q=15 is a representative value for a typical integrated CMOS voltage controlled oscillator (VCO) and Q=100 is included to present a rather extreme case (for integrated BiCMOS-VCO's). It is seen that for close-in frequencies the Leeson power spectrum goes above 0 dBc/Hz, and thus is not valid. At lower frequencies the spectrum becomes Gaussian, [8], which is more or less flat all the way to the carrier frequency. For integrated VCO's (Q=15 curve) it is seen that the cut-off is at some 8-10 Hz, i.e. well above our desired signals.

Fig. 3 also shows the residual phase noise at baseband, after down-conversion and filtering due to the range correlation effect, (6). It is seen that the phase noise is greatly attenuated.

B. VSR Overall Noise Limitations

Using the above mentioned observations the overall noise limitations on a VSR device can be analyzed. To do this, we first consider the well-known radar equation (the equation giving the power returned to the radar) together with equation (6). The power at the terminals of the receiving antenna can be expressed as, [9],

$$P_r = \frac{P_t G^2 \lambda_T^2 \sigma_e}{(4\pi)^3 d_0^4} \tag{11}$$

where P_t is the transmitted power, G is the antenna gain and where σ_e is the effective radar cross section (RCS) of the target, i.e. the person being monitored. It is assumed that the transmit and receive antennas have the same gain.

At a first glance it is evident that for a doubling in distance, the d_0^4 dependence results in a 12 dB attenuation of both signal and residual phase noise levels. Thus the signal-to-noise ratio (SNR) is degraded by this factor in regions where thermal noise (receiver noise figure) dominates over residual

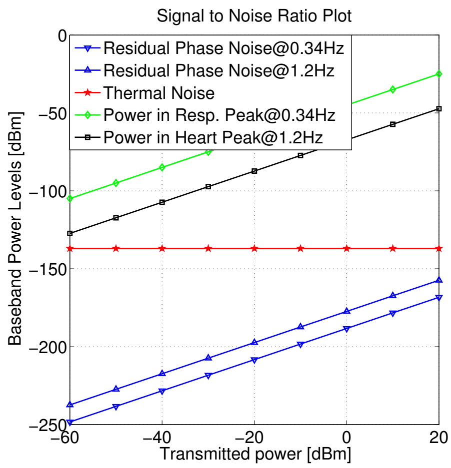

Fig. 4. Absolute power levels at baseband for thermal noise, oscillator phase noise, received respiration and heartbeat. Power levels plotted versus transmitted power. The SNR ratio can be read as the distance between the thermal noise floor and either the respiration or heartbeat levels.

TABLE I
PARAMETERS USED IN THE PLOT IN FIGURE 4.

freq	25 GHz	m_r	10 mm	Range	1 m
$G_{\text{LNA+Mix}}$	20 dB	m_h	0.15 mm	RCS (σ)	1 m^2
G_{Antenna}	10 dB	f_r	0.34 Hz		
NF	7 dB	f_h	1.2 Hz		
BW	10 Hz				

TABLE II
SYSTEM COMPONENTS IMPACT ON BASEBAND NOISE LEVEL.

Component	Thermal Noise	Phase Noise
LO	no	no
Power Splitter	no	no
PA	no	yes
LNA	yes	yes
Mixer	yes	yes
BB Amp	yes	yes
BB LPF	(yes)	(yes)

phase noise, i.e. for strong return signals. In regions where the residual phase noise dominates over thermal noise, the SNR degradation is determined by equation (6), i.e. as mentioned earlier a 6 dB degradation for a doubling of the distance.

Looking at a simulated example using absolute power levels for signal and noise components, will help to clarify which noise component is in fact the dominant one. Using equation (11) to calculate path loss due to a finite distance to the target, and equation (10) to obtain the relative strengths between the heartbeat, the respiration rate and carrier signals, while taking into account the phase noise filtering (equation (6)) a radar transceiver with the parameters given in table I, has been simulated. Here f_r and f_h are the frequencies of the respiration and heartbeat, respectively. The bandwidth (BW) is set to 10 Hz for noise floor estimation and reflects the fact that the desired signals could easily be filtered with such a BW at baseband (and even smaller BW once in the digital domain).

It is clearly seen that the region in which a VSR instrument normally operates (i.e. for transmit power levels below 0 dBm) is often dominated by the thermal noise in the receiver, *not* LO phase noise. This was also realized and briefly commented on through an experimental setup in [2], in which two different LO's with over 100 dB difference in phase noise performance, were used with very little difference in the detection accurary.

These observations are important in that they lower the requirements for the LO and thus simplifies the design of this component tremendously. They also imply that the phase noise of other components in the receiver chain can potentially become the limiting factor at baseband.

Aided by the fact that the range to the target and thus path loss is often relatively small, it is further seen from figure 4, that for a reasonable receiver noise figure (in which the phase noise of LNA etc. is taken into account, see section IV), it is possible to use very little transmit power. This is another desirable feature because of public radiation and power consumption concerns. A fully integrated sensor, with the microwave circuitry on a single low-cost BiCMOS chip will probably be the best system solution from a cost and size perspective.

IV. COMPONENT NOISE CONSIDERATIONS

Having realised that noise in the receiver chain is the limiting factor and not the LO phase noise, then it becomes interesting to study the impact of the components in the receive path. Reducing the noise floor level is best done with a low noise amplifier. There is relatively little demand to the LNA gain because of the small detection distances, but it has to be adequate to make the effect of the mixer noise figure neglible. Table II lists the components in the full radar system and classifies them according to the noise they contribute to the baseband noise level.

The SNR analysis (figure 4) shows that very limited transmit power is needed. The Typical LO power levels needed for the mixer can readily be obtained direcly from the LO, e.g via the thru arm of a directional coupler whereas the lower power level to be radiated by the antenna can be routed via the coupled port of the same coupler. A 20 dB coupler would probably be adequate in most situations. Using a coupler in this way has the added advantage of providing isolation between the LO and the antenna, which will often be subjected to reactive loading by the surroundings (person in close proximity). Furthermore, the LO port of the mixer is an invariant load that can be incorporated in the LO design. A power amplifier, although mentioned in table II, seems to be redundant in any case.

A comparative study has been done to compare two down-converter architectures based on resulting SNR, complexity and power consumption (figure 5). One architecture employs a passive mixer (FET ring) and the other an active mixer (Gilbert cell). Flicker noise from the LNA and the mixer in

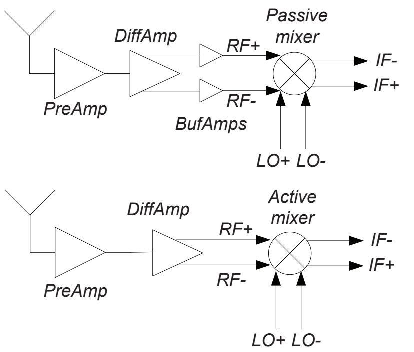

Fig. 5. Passive (top) and active (bottom) receiver architectures used for the comparison.

TABLE III
PERFORMANCE OF RECEIVER ARCHITECTURES.

Topology	Gain [dB]	NF [dB]	LO Power [dBm]	Phase Noise [dBc/Hz@0.1Hz]	P_{diss} [mW]
Active	20.0	4.1	-4	-	134.4
Passive	19	7	4	-117	136.0

the receiver chain will add to the baseband phase noise on top of the thermal noise floor. Passive mixer types are generally considered to have lower flicker noise than active mixer types and it is therefore interesting to compare them directly. Both downconverter topologies are based on a commercially available SiGe:C process; the SG25H3 from IHP-Microelectronics GmbH with f_T/f_{max} of 110/180 GHz. The design frequency is 25 GHz and a differential mixer architecture is used in order to reduce LO leakage, [10]. For a fair comparison the passive mixer topology employs extra buffer amplifiers to bring the overall gain to a comparable level. The results of the comparative study is shown in table III.

The IF output of the Gilbert Cell has the disadvantage that it needs DC-blocks for the transistor biasing. This presents a design challenge for direct downconversion because the cut-off frequency would have to be below 0.1 Hz. One possible solution could be to have high input-impedance operational amplifiers placed at the IF outputs. The FET resistive mixer does not have this disadvantage because the transistor bias is applied to the gate of the FET and not the drain or source (as the DC-bias of these two points have to be zero). Another passive mixer type, the diode ringmixer is likewise disadvantaged because it needs DC-blocks to bias the diodes.

The passive mixer architecture becomes physically larger due to the extra buffer amplifiers which also adds to the circuit complexity. The circuit sizes are 800x600 μm^2 and 735x600 μm^2 for the passive and active receiver chains, respectively. The required LO power for optimum conversion gain is also larger for the passive configuration.

The simulated phase noise added by the LNA and mixer in the passive configuration is -117 dBc/Hz at 0.1 Hz and is roughly 20 dB above the thermal noise floor. In the active configuration the added phase noise seems to be below the noise floor at 0.1 Hz. This is a surprising result that gives a clear advantage to the active mixer topology, but it needs to be verified experimentally.

The choice of using a passive versus an active mixer in the receiver part of the radar has no simple solution because both types have advantages and disadvantages. However, the increased LO power needed for the passive mixer and the added gain necessary to compensate for loss and thermal noise makes the active mixer system look like the most attractive solution in most cases.

V. CONCLUSIONS

The general signal theory for VSR instruments has been presented together with a discussion about local oscillator phase noise and range correlation. It has been shown that for most practical VSR instruments, the local oscillator phase noise is not a limiting factor. Instead the noise floor and thus flicker noise/phase noise of the receiver chain will dominate the noise performance. Choice of LNA and mixer topology seems to point in the direction of active rather than passive mixers. An active mixer topology has some obvious advantages with regards to size, gain, NF and LO power and has comparable power consumption. The higher phase noise typically seen in active mixers is much less of a concern in HBT's with low corner frequency.

In general there is a large margin for the SNR even at very low transmitted power levels, but for systems using high carrier frequencies there might be a large decrease in SNR at certain respiration amplitudes. This problem can be avoided if the carrier frequency is tunable.

REFERENCES

[1] J. C. Lin, "Noninvasive Microwave Measurement of Respiration," Proceedings of the IEEE, p. 1530, 1975.

[2] Amy D. Droitcour, Olga Boric-Lubecke, Victor M. Lubecke, Jenshan Lin and Gregory T. A. Kovacs, "Range Correlation and I/Q Performance Benefits in Single-Chip Silicon Doppler Radars for Noncontact Cardiopulmonary Monitoring," *IEEE Transactions on Microwave Theory and Techniques*, Vol. 52, No. 3, pp. 838-848, March 2004.

[3] Yanming Xiao, Jenshan Lin, Olga Boric-Lubecke and Victor M. Lubecke, "Frequency-Tuning Technique for Remote Detection of Heartbeat and Respiration Using Low-Power Double-Sideband Transmission in the *Ka*-band," *IEEE Transactions on Microwave Theory and Techniques*, Vol. 54, No. 5, pp. 2023-2032, May 2006.

[4] Enrico M. Staderini, "UWB Radars in Medicine," *IEEE AESS Systems Magazine*, pp. 13-18, January 2002.

[5] M. C. Budge and M. P. Burt, "Range Correlation Effects in Radars," *IEEE National Radar Conference*, pp. 212-216, 1993.

[6] Changzhi Li and Jenshan Lin, "Optimal Carrier Frequency of Non-contact Vital Sign Detectors," *Proceedings of the IEEE Radio and Wireless Symposium*, Orlando, pp. 281-284, 2007.

[7] D. B. Leeson, "A Simple Model of Feedback Oscillator Noise Spectrum," Proceedings of the IEEE, pp. 329-330, February 1965.

[8] Gleb V. Klimovitch, "Near-carrier oscillator spectrum due to flicker and white noise," *Proceedings of the IEEE International Symposium on Circuits and Systems*, Geneva, 2000.

[9] Merrill L. Skolnik, *Introduction to Radar Systems*, Third Edition, New York, United States: McGraw-Hill Companies, Inc., 1221 Avenue of the Americas, NY 10020, 2001.

[10] Changzhi Li, Yanming Xiao and Jenshan Lin, "A 5 GHz Double-Sideband Radar Sensor Chip in 0.18 μm CMOS for Non-Contact Vital Sign Detection," *IEEE Microwave and Wireless Components Letters*, Vol. 18, No. 7, July 2008.

www.elektro.dtu.dk
Department of Electrical Engineering
Electromagnetic Systems Group (EMS)
Technical University of Denmark
Ørsteds Plads
Building 348
DK-2800 Kgs. Lyngby
Denmark
Tel: (+45) 45 25 38 00
Fax: (+45) 45 93 16 34
Email: info@elektro.dtu.dk

ISBN XX-XXXXX-XX-X